

AD-A233 626

DTIC FILE COPY

①

STUDIES OF SEA ICE THICKNESS AND CHARACTERISTICS FROM AN ARCTIC
SUBMARINE CRUISE

ONR

Final Report on Phase III Continuation work accomplished under
Contract N00014-89-C-0014,
between 1 October 1989 and 30 September 1990

DTIC
ELECTE
MAR 25 1991
S D D

SAIC Polar Oceans Associates
Block A2, Westbrook Centre
Milton Road, Cambridge CB4 1YQ
United Kingdom

31 January 1991

DISTRIBUTION STATEMENT A
Approved for public release;
Distribution Unlimited

91 3 25 013

EXECUTIVE SUMMARY

This document reports Phase III of Contract N00014-89-C-0014, concentrating on the period between October 1989 and September 1990. Work undertaken by SAIC's Raleigh NC Office during 1990 is not reported here.

In spring 1987 a unique collaborative experiment took place in the Arctic Ocean. A submarine and two remote sensing aircraft co-operated in concurrent profiling and imaging of the upper and lower sea ice surfaces along the same track. The experiment provided opportunities for validation of airborne remote sensing systems using confirmed ice type and thickness information derived from below. Data collocation was achieved over a large area, north of Ellesmere Island (between approximately 60 and 140km long), for various combinations of sensors.

The submarine was equipped with a narrow beam upward-looking sonar and a sidescan sonar system. A NASA P-3A was equipped with an advanced multichannel microwave radiometer, an electrically scanning microwave radiometer, an airborne oceanographic lidar, a PRT-5 infra-red radiometer, aerial cameras and video. A Cessna Conquest was equipped with the Intera STAR-2 X-band synthetic aperture radar, (SAR).

During Phase III (October 1988 to September 1989), datasets were analysed by SAIC Polar Oceans Associates (Division 494) (submarine and SAR data), NASA Goddard and Wallops (P-3A data) and NASA JPL (aerial photography and SAR registration). Technical work concentrated on a detailed statistical comparison of various remotely sensed data for a 20km and a 60km section. Also 3500km of upward-looking sonar data were analysed statistically and work began on analysing the underice surface in wave number space.

During Phase III Continuation (October 1989 to September 1990), data analysis continued at SAIC Polar Oceans Associates. The analysis of the ice in wave number space was completed. Technical effort then concentrated on a rigorous classification of the underice surface. Verification of this surface (based on submarine sonar data) was undertaken to provide an unambiguous ice type map. A detailed comparison of sonar and SAR derived ice classifications was made for the region of best collocated data. Also, a major aim was to provide a coherent set of good quality data for the region of best collocation since it was important that the key data sets were made available to collaborators as soon as possible. All good quality data for the region of best collocation were assembled. SAR imagery was used as the basis for collocating data from other sensors. The data pack is a

Areal statistics of the underice surface were generated. The underice data give the most reliable classification of sea ice yet available for such a large area. The comparison of ice classifications derived from sonar and SAR addressed the question: "What information about the ice surface beneath the water can be provided by airborne remote sensing?". In order to do this a comparison was required of features classified and verified using submarine data and those seen on SAR imagery. A feature by feature comparison of the two data sets was undertaken that allows a transfer information from underice morphology to topside morphology. The efficacy of X-band SAR imaging of the upper ice surface was tested with respect to known ice types. the results presented have generally applicable implications for SAR imaging of sea ice fields.

Accession No. _____
NTIS GRA&I _____
DTIC TAB _____
Unannounced _____
Justification _____
By **per AD-A21939**
E _____
A-H

CONTENTS

CONTENTS	i
1 INTRODUCTION	1
2 BACKGROUND	2
3 PHASE III CONTINUATION SUMMARY	3
3.1 Task 1 Technical Liaison	3
3.2 Task 2 Data Map	3
3.3 Task 3 Compile Data Sets	4
3.4 Task 4 Two Dimensional Ice Type Transfer	4
3.5 Task 6 Wave Number Underice Characterisation	5
3.6 Reporting and Deliverables	5
3.6.1 Agreed deliverables	5
3.6.2 Delivered items	6
4 BASIC DATA ANALYSIS	6
4.1 Phase III Work	6
4.1.1 Coregistration	6
4.1.2 Analysis of submarine data	7
4.1.2.1 Upward-looking sonar data	7
4.1.2.2 Wave number spectra of upward- looking sonar data	8
4.1.2.3 Sidescan sonar analysis	8
4.1.2.4 Comparative analyses	9
4.1.3 SAR data analyses	10
5 PHASE III CONTINUATION	11
5.1 Autocorrelation Function and Power Spectrum	11
5.1.1 Data Analysis	11
5.1.2 Results	12
5.1.2.1 Autocorrelation function	12
5.1.2.2 Power spectrum	13
5.1.3 Conclusions	15
5.2 Data Map	17
5.2.1 Introduction	17
5.2.2 Sidescan data	17
5.2.3 Classification	18
5.2.4 Results	20
5.3 Sidescan Digitisation	23
5.4 Tie Pointing	23
5.6 Sidescan Statistics of Association	26
5.6.1 Introduction	26
5.6.2 Analysis	27
5.6.3 Feature association	27

5.6.4 A runs test for sequence data	29
5.6.5 Ridge spacing	29
5.6.6 Ridge orientation	32
5.6.7 Analysis of leads	35
5.6.7.2 Lead orientation	35
5.6.7.3 Lead width	37
5.6.7.4 Lead spacing	38
5.6.8 Summary	38
5.7 SAR Classification	40
5.8 SAR Statistics	41
5.9 Sidescan / SAR comparison	46
5.9.1 Areal fractions	46
5.9.2 One-to-one feature comparison	46
5.9.2.1 Methodology	46
5.9.2.2 Results	47
5.9.2.3 Discussion	49
5.9.2.4 Conclusion	50
6 DATA PACK	51
7 SUMMARY	53
8 PROGRAMME STATUS	54
9 ACKNOWLEDGEMENTS	54
10 REFERENCES	55
11 APPENDICES	56

1 INTRODUCTION

This report is a summary of achievements during Phase III Continuation of Contract N00014-89-C-0014, between October 1989 and September 1990.

During this year the thrust of the work undertaken (outlined in the Scope of Work issued in January 1990) reflected the concerns of the funding agencies, expressed in the progress meeting held in September 1989, at the offices of ONR. The Scope of Work was negotiated and agreed by SAIC and Dr P Wadhams and accepted by the funding agencies. During 1990 every effort was made to adhere to the scope outlined. Minor technical modification to the scope was necessary during the year as the work unfolded. These were agreed by SAIC and Peter Wadhams and communicated to Dr Curtin, ONR's technical representative.

The detailed comparison of above-ice and underice data sets that was undertaken during Phase III provided valuable background information for Phase III Continuation. The scope of work proposed for Government Fiscal Year 1990 was geared towards providing deliverables that are immediately useful to all the funding agencies. We also aimed to submit one or more papers, based on the work undertaken.

In order to ensure that the interests of all funding agencies were represented throughout Phase III Continuation, it was proposed that SAIC/Raleigh (North Carolina) effort should be included. This effort has been undertaken independently of SAIC Cambridge and is not reported here. SAIC Raleigh effort during FY 1990 is to be reported separately, as agreed with Dr Curtin.

Our first aim was to provide a coherent set of good quality data for the region of best collocation from the exercise between 19th and 24th May, 1987. It was seen as crucial that the key data sets were made available to collaborators as soon as possible. To this end, the first task was to produce a data map of the relevant portion of the exercise to identify the best region for further study. It was intended that all good quality data for this chosen region was assembled and disseminated to the funding agencies and collaborators, via ONR. SAR imagery was to be used as the basis for collocating data from other sensors.

Airborne data sets and tracks were to be located on the SAR imagery as were the submarine track (the last by identifying unambiguous tie points on sidescan and SAR). We proposed to address the question: "What information about the ice surface

beneath the water can be provided by remote sensing from above?". In order to do this a comparison was required of features 'typed' using submarine data and those seen on SAR imagery.

In order to maximise the skill level in ice type feature matching between sidescan and SAR, classification and digitising of the sidescan record was required. Our aim was to classify sidescan and SAR for ice features and types. A feature by feature comparison of the two data sets would then be possible that would allow transfer of information from the underice environment to the surface. To do this, SAR features would be matched to the sidescan record. After confirming the transfer function, the SAR imagery itself could be classified in terms of ice type so that the SAR would form an effective link between the sidescan-derived ice features and those seen by airborne sensors.

SAIC was also guided by the needs of our collaborators. First, to make available sets of data for a region of tight collocation, enabling future work on the data collected in the exercise. Second to provide sidescan-derived sea ice statistics to NASA staff before an important remote sensing (SSMI) meeting in April, 1990. Both these aims were achieved.

Throughout the period October 1989 to September 1990, SAIC Cambridge reported technical progress to Dr Curtin at ONR in monthly telemail messages (copied to NASA and OPO90) and in quarterly reports, issued via SAIC head office in San Diego. SAIC Cambridge has also issued several supplementary technical reports to ONR, on aspects of the work undertaken, either through SAIC in San Diego, or directly from Cambridge, if a report included secure information.

Finally, it was planned that an unspecified number of scientific papers would be submitted. At the time of writing, one paper has been submitted and a second is in preparation.

2 BACKGROUND

In May 1987 a collaborative experiment took place in the Arctic Ocean, A British submarine and two remote sensing aircraft co-operated in concurrent profiling and imaging of the upper and lower sea ice surfaces along the same track. The experiment provided opportunities for validation of remote sensing systems using ice of known type and thickness.

The submarine was equipped with a 780 upward-looking sonar System (narrow beam, 48 kHz) feeding chart and digital recorders and an EDO Western 602 sidescan sonar towfish (100 kHz) feeding an EDO 706 sidescan mapping system.

The two remote sensing aircraft were:

A. A NASA P-3A equipped with:

- i Advanced Multichannel Microwave Radiometer (AMMR) with 37GHz and 18GHz dual polarised channels and 21GHz vertically polarised channel,
- ii Electrically Scanning Microwave Radiometer (ESMR) operating at 19GHz,
- iii Airborne Oceanographic Lidar (AOL),
- iv PRT-5 infra-red radiometer,
- v aerial cameras and video;

B. A Cessna Conquest equipped with:

- i the Intera STAR-2 X-band HH-polarised synthetic aperture radar (SAR), giving a 63km swath width.

The SAR mission was funded by the UK Admiralty Research Establishment. All data collected on the submarine remain the property of the UK Ministry of Defence.

During Phase III (October 1988 to September 1989), datasets were analysed by SAIC Polar Oceans Associates (submarine and SAR data), NASA Goddard and Wallops (P-3A data) and NASA JPL (aerial photography and SAR registration).

During Phase III Continuation (October 1989 to September 1990), data analysis continued at SAIC Polar Oceans Associates, with SAIC's consultant, Dr P Wadhams. This document reports this effort.

3 PHASE III CONTINUATION SUMMARY

3.1 Task 1 Technical Liaison

Collaboration on technical methods and data analysis was maintained between SAIC/Cambridge, our consultant (Dr P Wadhams), NASA (Dr J Comiso) and SAIC/Raleigh (Dr T Clark).

3.2 Task 2 Data Map

The region of best near-simultaneous location of the airborne remotely sensed data, the SAR and the submarine data was

confirmed. Data quality for all sensors was tabulated and a data map produced. The data map (UK Confidential) was issued to ONR, directly from Cambridge.

3.3 Task 3 Compile Data Sets and Produce Data Pack

The production and dissemination of a set of collocated data was a key requirement of Phase III Continuation effort. The data map produced in Task 2 was used to identify of the most appropriate section for further analysis. All good quality airborne and submarine data were collocated on near-simultaneous and coincident SAR imagery. The submarine track was placed on SAR imagery using a series of unambiguous tie points, identified initially on photographs of the sidescan record. Then the P-3 track was placed on the same imagery. The completed imagery formed part of the data pack delivered.

The location of the submarine track on SAR imagery was a two stage process. Crucial to this task was the classification of the sidescan record for the region of best collocation. Ice types on the sidescan were classified and verified by reference to the upward-looking sonar record, giving the best possible approximation to an unambiguous classification scheme. This major activity is described more fully below, in Section 5. The 'map' of underice features produced and the similar SAR 'map' were constituent parts of the data pack, as were upward-looking sonar, AOL and AMMR data for the region of best collocation.

Once all data sets and imagery were assembled at SAIC, a data pack was generated (UK Confidential), documentation written and copies issued to ONR, direct from SAIC Cambridge.

3.4 Task 4 Two Dimensional Ice Type Transfer (incorporating parts of Task 5)

For the best collocated data segment, the spatial coherence was studied between the top surface of the sea ice and its underside. This task took identifiable ice regimes on the sidescan record and matched these to similar features on the SAR. In order to confirm the skill in identifying sea ice regimes on SAR, SAR features classified independently from the submarine data, according to pixel brightness and texture (that may have physical significance) were located on the sidescan record, classified in Task 3.

Along the line of the tied submarine track, like features were identified on the SAR and these compared to the underice feature map (classified by ice type). Success and failure rates for this matching were quantified. By overlaying the SAR map onto

the sidescan map the required basic link was provided between underice and surface.

The scope of work included the following definition of Task 5: "Determine Underice - Above Ice Surface Coherence & Provide Quantitative Statistics". Technical evolution of the project occurred during Phase III Continuation. One change to the work to be undertaken was agreed between SAIC and Dr Wadhams and reported to the funding agencies. Some Task 5 effort was incorporated within an expanded Task 4. Remaining Task 5 activities were considered inappropriate or not feasible considering the experience gained during this phase of the project. For example, time constraints on collaborators (whose input was crucial to the success of the task) forced a reassessment of attainable goals.

3.5 Task 6 Wave Number Underice Characterisation

As noted above, this task has been undertaken by SAIC Raleigh. It is not reported here, though the scope of work indicated that it would be. SAIC has ONR's agreement to issue two separate reports on FY 1990 effort.

3.6 Reporting and Deliverables

3.6.1 Agreed deliverables

The following were due for delivery during Phase III Continuation:

A) Reporting

- i. Monthly progress updates to ONR's representative.
- ii. Quarterly progress reports (3/31/90; 6/30/90; 9/30/90).
- iii. A preliminary Phase III Continuation Report /Presentation.
- iv. A Phase III Continuation Final Report, by 31st December 1990.
- v. Journal submissions pertinent to Phase III Continuation data analysis may be prepared during the course of the work.

B) Data Sets

- i. 'Data Map' of the 1987 data collection exercise up to and including 24th May.

- .1. 'Data Pack' consisting of complete collocated data sets from all main instruments, with documentation.
- iii. Classified SAR hard copy output, consistent with the data pack.

C) Supplemental Deliverables

We also aimed to issue supplementary deliverables (not specified in the scope of work) consisting of technical reports of work undertaken during Phase III Continuation.

3.6.2 Delivered items

At the time of writing, the following have been delivered:

- A) i, v (times two).
- B) i, ii and iii.
- C) 3 reports

- A) ii: Quarterly reports have been issued for 3/31/90 and 6/30/90, though not for 9/30/90
- A) iii: Because of time and budget constraints no presentation has been made, nor is one planned.
- A) iv: This document.

4 BASIC DATA ANALYSIS

4.1 Phase III Work

4.1.1 Coregistration

The submarine spent ten days operating independently in the Arctic, collecting upward-looking sonar data and ending at the North Pole. Then, 23 days of concurrent submarine and aircraft profiling was undertaken, along a track running southward from the Pole towards Greenland, then eastward towards Fram Strait and finally, running southward through the East Greenland pack ice. Registration of the submarine data was achieved by converting the upward-looking Sonar record from a function of time to a function of distance. This was accomplished using recorded position fixes for the submarine, together with measured curves of acceleration and deceleration during times of speed change.

Detailed registration was undertaken for the aircraft, for a 200km section to the north of Greenland for May 20th. GPS and high-altitude photography information were used to register the

P-3A sensor data to SAR imagery. Features such as leads were matched between the data sets by a NASA team (Wadhams *et al.* 1991). During Phase III (October 1988 to September 1989) SAIC co-registered the submarine track with the SAR imagery, for approximately 60km within the 200km section, using the sidescan sonar record to match features with the SAR. The SAR imagery became the base data set on which both the P-3A and submarine tracks were superimposed. Work during Phase III comprised systematic comparisons of sensor outputs for portions of this 60km.

4.1.2 Analysis of submarine data

4.1.2.1 Upward-looking sonar data

Upward-looking Sonar profiles were obtained using the sonar with a transducer on the top of the submarine fin (10° beamwidth). The effective footprint of the beam on the ice bottom was about 15m. The raw digital data obtained were quality-controlled and gaps filled by manual digitisation of the chart record. Range was converted to draught by identifying points on the chart record that were open water (very strong echoes, often containing multiple returns). These points were joined by a smooth polynomial, that was then subtracted from the range to leave a record of draught versus time. This was converted to one of draught versus distance using the handwritten submarine log in combination with the onboard Ships Inertial Navigation System (SINS) log. Finally, the record was quadratically interpolated to yield a discrete ice draught series at 1m along track intervals. The 1m ice draught record was analysed in 50 along track sections, each 50km long (see the Phase III Final Report, issued in February 1990).

Various statistical analyses were undertaken for each 50km section. Line printer output and sample graphical results for a sample section (Section 1) were presented in the progress report, issued in September 1989, together with a commentary on each output statistic. A copy of the line printer output of statistics for all 50 sections is to be delivered to ONR directly by Dr P Wadhams. Details of the following parameters of the underice environment are included in these results (for details, see the Phase III Final Report and Dr Wadhams' report):

- A. the normalised probability distributions of ice draught and derived statistics.
- B. polynya/lead distributions and derived statistics.
- C. smooth ice distributions.

- D. rough ice distributions.
- E. smooth and rough ice length and draught analyses and derived statistics.
- F. pressure ridge draught and spacing analyses and derived statistics.

4.1.2.2 Wave number spectra of upward-looking sonar data

During Phase III a preliminary analysis was carried out for energy spectra of the underice surface. This was reported in the Phase III Final Report. Spectra were computed for each of the 50km sections. Each underice record was sampled at 12m intervals. Previous underice records from the marginal ice zone region typically showed spectra where the energy density varies as k^{-3} . However, in this study no such variation was shown for the ice interior. Instead, the energy density appears to vary approximately as k^{-4} for wavelengths less than 11m and as k^{-2} or even k^{-1} at longer wavelengths. Thus, there is a 'knee' at about 11m wavelength, clearly seen in the averaged spectrum and also visible in most of the individual 50km sections.

During Phase III Continuation, this work was extended and finalised. The results are outlined in Section 5.1 below and the report issued is included here as Appendix I.

4.1.2.3 Sidescan sonar analysis

Sidescan sonar data were recorded on electrically sensitive paper, producing a fragile analogue record. When the submarine was travelling at less than 8kts and kept constant depth, a geometrically correct chart record was generated (compensated for both depth and speed).

A total of 3000km of sidescan record was collected, of which 1000km was geometrically correct. Various analyses were undertaken in Phase III. These are discussed in the Phase III Final Report and in two papers: Comiso *et al.* (1991) and Wadhams *et al.* (1991).

AMMR footprints were placed on the SAR data by reference to underlying ice type, given by the sidescan sonar record. This coregistration exercise could only be seen as a first approximation and in view of the requirements of the funding agencies, a major part of Phase III Continuation effort was directed at providing a more rigorous match of the data sets over the region of best overall collocation.

4.1.2.4 Comparative analyses

Sonar and laser data were compared in Phase III as part of the intensive analysis reported in Comiso et al. (1991). A joint statistical analysis was carried out on three consecutive, corresponding 20km sections of upward-looking sonar and laser data. Analysis of the probability density functions (pdfs) was carried out for ice draught and elevation. The overall mean draught was compared with the overall mean elevation. The result was a ratio of 7.909. This agrees with previous work. A close agreement was found between draught and elevation pdfs. It appears that surface features in the ice cover are magnified by 7.909 on the underside, by isostasy. It was concluded that, in ice cover typical of the central Arctic, it is possible to derive the pdf of ice draught (and thus of ice thickness) solely from the results of airborne laser profiling. This result has important implications. Airborne surveys are easier to conduct than submarine surveys and our ability to monitor synoptically large scale ice thickness distribution in the Arctic would be greatly increased if this result was generally applicable.

An analysis was also carried out of ridge and keel distributions, using the same three 20km sections as above. An empirical transformation was carried out to derive keel distributions from sail distributions. However, these transformations are not based on isostasy. It was found that keel distributions could be obtained from ridge sail distributions. This requires testing using longer sections of data before it can be applied generally. These results are discussed fully in Comiso et al. (1991).

Two sections, respectively 10km and 22km in length were used to compare SAR brightness with ice draught and elevation. The original SAR pixels (15.45m x 5.6m) were subsampled 1 by 3 in order to obtain pixels covering an area of 15.45m x 16.8m. The sonar and laser data were filtered to have equivalent along track resolutions. Point-for-point comparisons were then made between SAR brightness and ice draught or elevation and regression analyses undertaken.

The correlation coefficient for point-to-point comparison of sonar and SAR was 0.39. Both SAR and ice draught were then windowed over n pixels along track, to try to improve the correlation. As n was increased, the correlation coefficient r for SAR brightness versus ice draught increased but there was an upper useful limit dictated by the need to have a good spread of data in the scatter diagrams. It was found that $n = 15$ gave the best windowed correlation, with an r of 0.68. This implies that 46% of the variance in ice draught can be explained in terms of

SAR brightness variations. The corresponding averaging length is 252m. These results are discussed fully in Wadhams et al. (1991). It is stressed that these results should be seen as first approximations to reality, since they depend on the accuracy of the placement of the submarine track on the SAR imagery, that was undefined by the Phase III work. Work during Phase III continuation has shown us that this placement can be achieved to approximately $\pm 16\text{m}$. However, the Phase III analysis has not been replicated after rigorous collocation.

These Phase III results gave some promise that X-band SAR could be used as an empirical means of inferring regional ice draught distribution. However, the correlation can never be as good as that between sonar and laser, since ice elevation and draught are connected by isostasy, whereas SAR brightness is determined by ice roughness, salt content and snow cover and is only indirectly related to ice draught. These results have lead to further work during Phase III Continuation, in comparing sonar and SAR for an extended length of collocation. The results are outlined later in this document.

The combination of platforms provided a unique opportunity for the validation of passive microwave data over long lengths of track. Initial analysis compared AMMR with ice type and ice draught. During Phase III Continuation, the generation of a data pack consisting of co-registered data will make future analyses easier. In Phase III, a 190km test region was studied. AMMR footprints were marked on SAR imagery. The footprints were then transferred manually to a photomosaic of the sidescan sonar imagery, and analyses carried out of dominant and subsidiary ice types within the footprint.

Sea ice was classified as ridged; undeformed multiyear; undeformed firstyear; young ice; refrozen lead; and open lead. Where a footprint overlapped the submarine track itself, the ice draught was measured from the upward-looking sonar and given as an average for the 33m length of the footprint. Some 280 footprints were analysed, of which 40 yielded ice draughts as well as types. Initial results are reported in Comiso et al. (1991). It was found that the large amount of deformed ice in this region hampered ice discrimination. During Phase III Continuation, a more rigorous collocation exercise was undertaken in order to produce the data pack.

4.1.3 SAR data analyses

In Phase III an investigation was carried out using the GEMS image analysis system at SAIC's Cambridge office, of SAR pixel frequency distributions for the various ice types. High Arctic

ice was separated visually into six distinct ice types: lead; new ice; firstyear (FYR) ice; smooth floes; complex floes and ridges. This was based on a comparison between SAR and sidescan. These six categories were reduced to four broader classes: lead and new ice; FYR ice; floe and complex floe (or multiyear ice, MYR) and ridges. These four classes could be successfully separated digitally.

Because of the difficulty of precisely collocating SAR with sidescan, the analysis was seen as preliminary. It provided the basis for the main thrust of technical work in Phase III Continuation towards the generation of a two dimensional transfer function between the underice environment and the ice surface. These analyses are discussed later in this document.

4.2 Phase III Continuation - Summary

During this final year of technical effort several key tasks were undertaken (as described in Section 3) and completed successfully (see Section 5 below). The data map and data pack were completed approximately on schedule. The delivery of both were delayed whilst SAIC obtained relevant security clearances. Also, the data pack was delayed because SAIC decided to include in it a digital SAR type map and corrected (relocated) upward-looking sonar data, to match the other data in the pack.

Work on deriving sea ice type data maps and statistics (based on sidescan imagery, verified using upward-looking sonar data) was crucial to the success of this year's programme and was completed approximately on time, despite some technical difficulties with digitising. SAR imagery was digitised and classified independently of the underice data. The final thrust of this part of the project was to compare the sidescan and SAR, along 109km of track. This was completed in late summer 1990.

5 PHASE III CONTINUATION

5.1 Autocorrelation Function and Power Spectrum

5.1.1 Data Analysis

Using 'away from the pole' data from the 1987 submarine cruise, autocorrelation and spectral analysis techniques were used to investigate the nature of the roughness of the underside of Arctic sea ice and its geographical variation.

The purpose of undertaking this analysis was to gain insight into the geometrical properties of the underside of Arctic sea

ice, in order to ascertain the statistical nature of underside roughness. This work is applicable to ice-ocean frictional coupling, internal wave generation by ice, ice forces on structures and acoustic scattering by the underside of the sea ice. The supplementary deliverable detailing this analysis is included here as Appendix I.

The autocorrelation function and power spectrum of the ice underside were analysed in wave number space. The dataset used was the corrected ice draught data, derived from upward-looking sonar data and extending from the North Pole into Fram Strait. The 1m interval data described earlier in this report were divided into 35 sections, each 50km long, from north of Greenland to Fram Strait. The analysis for autocorrelation function and power spectral density was carried out over successive 2km subsections within each section, with ensemble averaging to improve the statistical reliability. Each 2km subsection had to be complete, with no gaps, for the spatial analysis to be valid. If fewer than five, complete 2km subsections were available, then the section was not used. Seven sections were rejected (Sections 4 to 6 and 17 to 20), leaving 28, that were analysed.

The sections were divided into three groups. Group 1 (Sections 01-12) comprises the central Arctic Basin. Group 2 (Sections 13-28) comprises the Greenland Offshore Zone. Group 3 (Sections 29-35) comprises Fram Strait south of about 81°N, a region with broken floes and much open water because of the proximity to the Greenland Sea. The normalised autocorrelation function was computed, for lags of up to 1000m. The power spectral density was computed using conventional FFT techniques for wave numbers of up to 0.5m^{-1} . Results for each subsection were ensemble averaged to yield results for a whole section.

5.1.2 Results

The results of the analysis are detailed in Appendix I. Here they are outlined briefly.

5.1.2.1 Autocorrelation function

The general appearance of the autocorrelation functions was straightforward with only one section showing clear secondary peaks. The lag at which the autocorrelation function first reaches zero is shown in Table 1, that also shows the Lipschitz exponent. Plots of $\ln(1 - \bar{R})$ (\bar{R} is the autocorrelation coefficient) against $\ln \tau$ (τ is the lag) had slowly increasing slopes for lags of up to 8m, then relatively constant slopes for lags up to about 20m, then a decreasing slope. It is likely

that at the smallest lags, the autocovariance is artificially increased because the sonar had a beamwidth of about 5° (giving a surface beam diameter of about 8m) and so gives a smoothed profile. Therefore, the range of lags from 8m to 20m was used to obtain a best value for each section, by linear regression.

Large differences of computed Lipschitz component were not seen but some geographical differences were evident. A slightly longer coherence length was indicated for ice features in Fram Strait than in the Arctic Basin, possibly a consequence of the dominance of the profile by floes and wide leads rather than by pressure ridges. A relatively small Lipschitz component in Fram Strait and a relatively larger one in the Greenland Offshore Zone were seen. This implies that fractal roughness as defined by the Hausdorff dimension is highest in Fram Strait and lowest in the Greenland Offshore Zone where the physical roughness (for example, mean ice draught and frequency of ridges) is greatest. This is an interesting paradox.

However, within each geographical group there were wide variations and the trends noted above may not be significant. These results were compared to those obtained by another British submarine to the Fram Strait and Arctic Basin in summer 1985. Then, Lipschitz exponents lay in the range 0.5 to 0.8, suggesting a lower fractal roughness in summer that may result from smoothing of the ice surface by melting.

5.1.2.2 Power spectrum

The power spectral density of the ice under surface [$S(k)$] showed three distinct slope domains, when plotted on a log-log scale. At low wave numbers (very long wavelengths of 300m or more), the decay of the spectrum with increasing wave number was slow. This corresponds to wavelengths where the autocorrelation function shows little or no coherence. At moderate wave numbers (corresponding to wavelengths of between about 300m and 10m), the spectrum falls off as a power law. At high wave numbers (corresponding to wavelengths of less than 10m), there is a 'knee' in the spectrum followed by a more rapid fall off in energy density with increasing wave number.

As noted above, the autocorrelation function has anomalous properties at lags of 8m or less and that 8m is approximately the surface beam diameter of the sonar. Thus, it is likely that the smoothing of the underice profile caused by sonar beamwidth was producing an anomalously rapid fall off in energy at wave

Section	Lag (m) at which R crosses zero	Lipschitz exponent	Hausdorff dimension
1	271	0.560	1.440
2	389	0.520	1.480
3	362	0.448	1.552
7	195	0.527	1.473
8	271	0.513	1.487
9	317	0.409	1.591
10	146	0.518	1.482
11	331	0.557	1.443
12	120	0.540	1.460
13	202	0.537	1.463
14	313	0.535	1.465
15	390	0.403	1.597
16	265	0.669	1.331
20	448	0.667	1.333
21	227	0.710	1.290
22	175	0.711	1.289
23	248	0.510	1.490
24	180	0.438	1.562
25	204	0.341	1.659
26	248	0.526	1.474
27	298	0.556	1.444
28	215	0.514	1.486
29	226	0.516	1.484
30	407	0.518	1.482
31	388	0.444	1.556
32	357	0.426	1.574
33	318	0.472	1.528
34	290	0.456	1.544
35	371	0.348	1.652

Table 1. Properties of autocorrelation functions.

numbers corresponding to wavelengths of less than the surface beam diameter. Thus, this part of the spectrum can be regarded as an artefact of the sonar system.

The region of moderate wave numbers was studied further by measuring the slope of the linear part of the log-log spectrum and defining the range of wave numbers over which this linearity occurred. Results are given in Table 2. Three of the sections (22, 27, 29) have two gradients, since the spectrum changed slope within the range of moderate wave numbers. On the whole, however, there is consistency between sections. The log-log plots show a straight line from about 10m wavelength (corresponding to the beginning of beamwidth-induced smoothing) to a wave number corresponding to about 200m wavelength. The exponents show some very low values, especially in the Fram Strait sections, but mostly these also lie within a limited range. The central Arctic Basin (Sections 1-12) has a mean exponent of -2.21 over a range of validity from 14m to 213m wavelength. The Greenland Offshore Zone has mean exponents of -2.19 and -2.33, for the first and second quoted slopes, respectively. The Fram Strait zone has a mean exponent of -1.91 from 12m to 163m using the first slope in section 29 but -1.99 from 16m to 179m, using the second slope.

It is clear that the Arctic Basin and Greenland Offshore Zone have similar p values (valid over a somewhat more restricted range of wavelengths for the Greenland Offshore Zone), whilst the Fram Strait data suggest a lower p value. Translating these into Lipschitz exponents, values are obtained of 0.61 for the central Arctic, 0.60 to 0.67 for the Greenland Offshore Zone and 0.46 to 0.50 for Fram Strait. These values agree reasonably well with Lipschitz exponents estimated from the autocorrelation functions.

5.1.3 Conclusions

The underside of Arctic sea ice is a rough surface that obeys the Lipschitz condition, with exponents in the range 0.5 to 0.8. The autocorrelation function at small lags (8m to 20m) has a uniform slope from which the Lipschitz exponent and Hausdorff dimension may be calculated. At very small lags the autocorrelation function is affected by the finite beamwidth of the echo sounder. The power spectral density of the ice surface $[S(k)]$ varies as k^p , where p takes average values between -1.9 and -2.2 at wavelengths between 10m and about 200m. The Lipschitz exponent derived from the p value agrees quite well with exponents estimated from the shape of the autocorrelation function.

Section	P	Range of validity (m)	
		From	To
1	-2.32	10	158
2	-2.09	10	229
3	-2.15	10	316
7	-2.07	10	178
8	-2.21	10	115
9	-2.36	40	347
10	-2.27	16	158
11	-2.17	10	219
12	-2.25	9	200
13	-2.25	10	58
14	-2.57	25	316
15	-1.58	13	275
16	-2.78	10	115
20	-2.75	20	91
21	-2.66	11	158
22	-2.06 / -3.24	10 / 29	29 / 95
23	-2.00	10	182
24	-1.91	10	219
25	-1.86	10	69
26	-2.44	10	69
27	-1.70 / -2.36	10 / 40	40 / 219
28	-1.94	10	275
29	-1.69 / -2.27	9 / 36	36 / 145
30	-2.19	20	182
31	-1.76	16	457
32	-2.17	11	50
33	-1.51	10	87
34	-2.39	10	76
35	-1.66	10	251

Table 2. Exponents governing wave number spectrum and their ranges of validity

The fractal 'roughness' is greatest in the Fram Strait region and is fairly consistent over the rest of the Arctic Basin region sampled. This is despite the fact that the physical roughness (expressed in terms of mean and r.m.s. ice draught) is lowest in the Fram Strait region.

5.2 Data Map

Between 19th and 23rd May 1987 the overlap and quality of the data from the individual sensors varied considerably. To determine areas with good quality, comparable data, the results of the missions were mapped. The tracks of the submarine and AOL record were mapped, together with the SAR image area. A large scale map was produced that allowed the region of best collocation to be defined more precisely. The results indicated that the region of best collocation was sensed on 20th May. On that day, good quality sidescan sonar, upward-looking sonar and SAR overlapped for roughly 110km. Good quality AOL and SAR overlapped for approximately 135km and good quality sidescan and SAR overlapped for about 140km. The overlap for all data sets was 65km.

Based on this information, it was agreed that we would classify 150km of sidescan imagery. That section of sidescan also matches approximately 110km of upward-looking sonar and 105km of AOL. One further region of good overlap was identified on 21st May but this was too short to provide a reasonable length of sidescan for ice type classification.

5.3 Classification of Sidescan Sonar Imagery

5.2.1 Introduction

Approximately 140km of sidescan sonar chart roll were collected in the region of best collocation, north of Ellesmere Island. The sidescan imagery was classified by ice type and the classification scheme verified by using upward-looking Sonar data. A report detailing this analysis, entitled "The Classification of sidescan Imagery for Ice Types", was issued in March 1990. The digital sidescan data were located onto near-simultaneous and coincident SAR imagery, using a series of unambiguous tie points.

5.2.2 Sidescan data

The sidescan data used were in the form of a series of photographs, taken from the original chart roll and corresponding to a total length of around 140km. These images

were of sections 1km wide (across track) and around 1.5km long (along track). On each frame only the swath within around 350m of the centre line (zenith) received a strong enough sonar backscatter to produce a clear image. This gave a usable swath width of approximately 700m. The actual average width was 673m.

5.2.3 Classification

The images were classified manually by two experienced analysts into areas of different ice type. Thus:

- i. **ridges (r)**: linear features characterised by strong backscatter from the nearside of the ice blocks and dark shadow from the far side. Clear crests can be seen.
- ii. **firstyear ice (f)**: characterised by a smooth underside sometimes criss-crossed by narrow cracks.
- iii. **multiyear ice (m)**: characterised by a less smooth or rugged underside with distinctive bulges.
- iv. **'bright' leads (l)**: identified by linearity and being smooth, poorly scattering surface (specular reflection), lighter than w. May be recently refrozen.
- v. **'dark' leads (w)**: identified by linearity and high scattering (stronger sonar return), darker than l. Sometimes appear striped or banded.
- vi. **unclassified (u)**: areas where classification is unclear because of poor return.
- vii. **matrix (Mx)**: the area remaining after classification of all features with well defined boundaries. Matrix is characterised as non-linear ridge and rubble fields with complex underice topography (hummocky).

The classification of the sea ice underside using upward-looking sonar data is based on ice draught and slope (Comiso et al. 1991) and Table 3 compares this classification with that using sidescan sonar, described above. From the upward-looking sonar classification, preliminary assessments were made of the range of ice draught within each class. Each individual feature identified on the sidescan was allocated an identifier consisting of two letters followed by an identification number. The first letter was used to identify the feature type (r,f,m,l,w or u) followed by the second letter that could either be the same as the first for features entirely within the swath width, or 'e' for features that crossed the swath edge (for example rr130, fe23, ww29). The result was a series of 86 hand-drawn classification maps showing individual ice features. Appendix II here explains the analysis in more detail.

Ice Type	Sidescan Classification	Upward-looking Sonar Classification	Draught range (m)
i. Ridge (r)	Linear, strong backscatter / dark shadow. Clear centre line	Defined by Rayleigh criterion (eg. Wadhams and Davy, 1986)	$r > 5m$
ii. Firstyear (f)	Smooth, narrow cracks	Smooth bottom (bottom slope $< 5\%$)	$1 < f < 2.5$
iii. Multiyear (m)	Less smooth or rugged with bulges	High mean draught, a bumpy relief with bulges	$2.5 < m < 4m$ Bulges $< 1m$
iv. Lead (l)	Linear, smooth, weak return	Thin level ice. Smooth bottom (slope $< 5\%$)	$l < 1m$
v. Lead (w)	Linear, smooth, strong return, maybe banded	Thin level ice or open water (slope $< 5\%$)	$w < 1m$
vi. Unclassified (u)	Poor return	-	-
vii. Matrix (Mx)	Non-linear ridges and rubble, hummocky	Rough ice (bottom surface slope not always less than 5%)	$Mx > 2.5m$

Table 3. Comparison of ice type classifications from sidescan sonar and upward-looking sonar data with likely ice draught ranges.

5.2.4 Results

This classification was carried out initially without reference to upward-looking sonar data, that were obtained concurrently. The sidescan overlays were then examined and compared with the upward-looking sonar record. Classifications that were judged to be false in the light of this comparison were changed. This could only be done for ice features that straddled the zenith. The data comparison was carried out for 86 frames, representing about 140km of track. Of a total of 2397 features identified, 767 separate ice features from the initial identification straddled the zenith.

Table 4 shows the overall results, validating sidescan classification with upward-looking sonar data. An identification was declared to be erroneous if the upward-looking Sonar record demonstrated that a different classification was appropriate, even if that classification included the original ice type as part of itself (e.g. the addition of a pressure ridge to the centre of an area of 'matrix', turning it into a ridge and two areas of matrix).

The most reliable identifications were of pressure ridges, only 3% of which were erroneous. The identification of multiyear ice was also reliable (87% successful) but that of firstyear ice was not very good. Only 35% of firstyear identifications on the sidescan were confirmed by the upward-looking sonar record. matrix was correctly classified 75% of the time. Given longer to analysis each photograph, further subdivision would have been possible, resulting in fewer mis-identifications of matrix. The overall success rate of 78% indicates the suitability of classifying sea ice using sidescan sonar imagery.

Our report "The Classification of Sidescan Imagery for Ice Types" includes a detailed discussion of the error analysis undertaken of the classification and of the results for each individual ice type. Briefly, two error types were identified:

Type A error: a feature was assigned to a given category and after reference to the upward-looking sonar record, was seen not to belong to this category, or

Type B error: failure to identify a feature of a given ice type whose presence on the imagery was confirmed by upward-looking sonar.

A revised distribution of ice types resulted and Table 5 indicates classification success and failure rates in terms of

Ice Type	Correct IDs		Erroneous IDs		Total Number	%
	Number	%	Number	%		
Matrix	196	72.1	76	27.9	272	35.5
Multi-	233	86.6	36	13.4	269	35.1
First-	12	34.3	23	65.7	35	4.6
Ridge	116	96.7	4	3.3	120	15.7
Lead l	19	73.1	7	26.9	26	3.4
Lead w	19	52.8	17	47.2	36	4.7
Unc'fd	1	11.1	8	88.9	9	1.2
Totals	596	77.7	171	22.3	767	100.0

Table 4. Success and failure rates of classification of ice types on sidescan sonar images by validating using upward-looking sonar data, for 85 sidescan photographs.

error type. Overall, more multiyear ice features were introduced by the correction procedure, than were lost and a large number of 'new' ridges were identified. However, almost all of the original ridge identifications were correct. Again firstyear classifications are seen to be unreliable. Table 6 shows the revised **total numbers of features** in each ice type category. The overall number of features seen along the zenith rises from 767 to 899 but the proportion of multiyear features remains almost the same.

This indicates that even an un-validated sidescan classification is likely to provide a good measure of the proportion of multiyear ice features, at least in this region of the Arctic, in spring. By contrast, the proportion of ridges in the corrected feature map is greatly increased. Thus, raw ridge counts using sidescan data are likely to underestimate the total number of ridges present. The proportion of matrix is reduced, reflecting its nature as a residual category, that can be partially re-assigned using upward-looking sonar data and will vary with the time spent on and resolution of the initial classification. We conclude that the numerical fraction (as opposed to areal fraction) of multiyear ice seen on the sidescan is a reasonable estimate of the actual fraction, as is the fraction of total leads, whereas the fraction of ridges is probably too low (perhaps by a factor of two).

Ice Type	Correct IDs	Type A	Type B
Matrix	196	76	66
Multiyear	233	36	86
Firstyear	12	23	19
Ridge	116	4	109
Lead l	19	7	12
Lead w	19	17	11
Uncl'fd	1	8	0
Total	596	171	303

Table 5. Overall Summary of Type A and Type B Errors in the classification of sidescan imagery.

Ice Type	Original ID		Corrected ID	
	Number	%	Number	%
Matrix	272	35.5	262	29.2
Multiyear	269	35.1	319	35.5
Firstyear	35	4.6	31	3.4
Ridge	120	15.6	225	25.1
Lead l	26	3.4	31	3.4
Lead w	36	4.6	30	3.3
Uncl'fd	9	1.2	1	0.1
Total	767	100.0	899	100.0

Table 6. Original and revised total numbers of features, by class.

The analysis of errors leads us to ask: what further changes would have occurred if the entire area of each overlay had been verified, rather than just the features that crossed the zenith? To consider this, the proportion of the features in the 673m

swath that straddle the zenith was determined. It was found that 25% of features crossed the zenith. Thus, the validation dealt with only 25% of the ice features present. 75% remain not validated and the changes shown in Table 6 represent only a quarter of the changes that might occur if the entire sidescan image could have been tested against ice thickness profiles. This is not the same as saying that the magnitude of the changes in proportions in Table 6 should be multiplied by four to yield a final correct set of values. But it does suggest that the correct proportions would involve further changes in the same direction as those indicated in the table.

5.3 Sidescan Digitisation

The classified features were digitised manually as a series of x,y co-ordinates via a Kontron MOP digitising unit. In addition to the outline, the digitising unit output various statistics for each classified shape. These included area, perimeter and orientation of the major axis. The 86 digitised images corresponded to a track length of around 140km (including a gap of 6.362km). Each of these images was displayed, plotted and compared with the original classification map, to ensure accuracy.

The digitised sidescan record thus generated from the corrected, classified data, was used to generate areal statistics of the ice types and features studied (see Section 5.5 below).

5.4 Tie Pointing

Because of variations in the ratio of platform speed to chart recorder speed, variations in the along track scale occur in the sidescan that are not present in the SAR data. By comparing the sidescan with the SAR data, a series of 50 points were found that could be unambiguously identified on both datasets. Converting the pixel values of these tie points to distances and comparing with the distance between the tie points on the sidescan image, enabled scaling factors to be calculated for each of 49 sections. In addition to this, each image was rotated and translated so as to give a consistent set of x,y values (see Figure 1). Then, the images were re-scaled individually to minimise rounding errors.

Unfortunately, the SAR data did not cover the first six frames and it was not possible to identify tie points unambiguously in the next six frames. Hence, collocation with the SAR data was only possible for 74 of the small frames, corresponding to a distance of around 119km. All the 74 separate image frames were then plotted to the same scale as a hard copy enlargement of the

relevant portion of the SAR imagery and photocopied to acetate to enable the two datasets to be overlaid.

Between successive pairs of these tie points, a constant submarine speed/chart speed ratio was assumed and the digital sidescan record adjusted by 'stretching' or 'squashing' the digitised data. In this way, we have achieved the best possible location of the sidescan, without being unduly biased by subjective matching of SAR and sidescan features. The digitised sidescan record was used to generate areal statistics of the ice types and features studied.

5.5 Ice type areal fractions

Table 7 shows the verified areal percentages of the various ice types seen from beneath the ice, as well as statistics of feature size. Because the SAR imagery could provide only a limited view of the ice surface in terms of ice type, the information provided by the submarine data is vital for detailed analysis of the area.

These data confirm that the region studied was intensely deformed, resulting in a high proportion of small scale ridging and rubble fields that cannot be seen as belonging uniquely to any of the 'classical' sea ice types. Also, previous deformation events resulted, by spring, in a relatively small areal fraction of undeformed first year ice and leads.

Approximately 50% of the total area of the sidescan imagery comprises matrix. It is likely that there is no valid way to split this region into other ice types, except for re-analysing the original imagery to extract progressively smaller homogeneous units, such as linear ridges. At the time of the data collection in May 1987, the study region was clearly not made up of a simple mix of clearly defined floes, leads and ridges but was predominately heavily deformed.

Of the area not defined as matrix, the area of clear multi-year ice (30% of the total) is twice that of clear linear ridges (15% of the total). First year and lead fractions comprise less than 2% and 3% of the total area, respectively.

By inspection, the statistics presented indicate that the distributions of feature sizes are not Gaussian. This was confirmed for most of the feature size and shape parameters studied (area, Ferret diameter, perimeter length). Their distributions are all highly positively skewed, both for features contained within the swath width and for edge features.

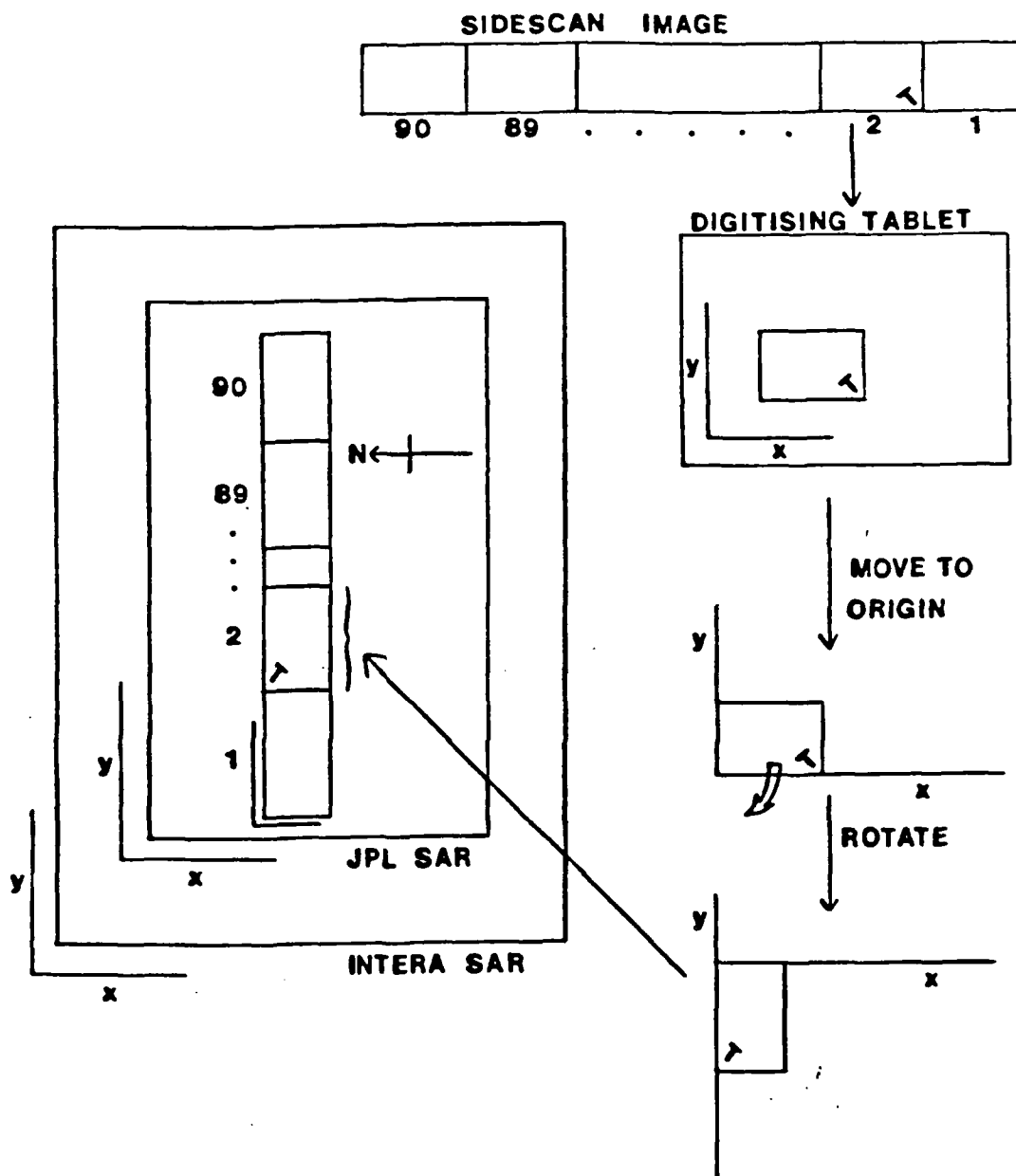


Figure 1. Schematic diagram showing the stages of digitising and rotating Sidescan images to collocate each onto the available SAR imagery.

Ice Type	Number		Total Area (10^6m^2)	Areal Fraction	Areal Statistics (10^3m^2)*		
	Within Swath	Total (incl. edge)			Mean	Median	St.Dev
l	12	37	1.4	1.9	13.0	8.6	10.4
w	53	71	0.8	1.1	8.5	4.7	11.0
f	41	67	1.4	1.8	9.1	7.0	10.2
m	589	811	22.7	29.7	18.1	9.8	24.3
r	1285	1378	11.2	14.7	7.7	5.9	6.4
Mx	-	-	37.8	49.7	-	-	-
u	4	33	1.1	1.1	4.8	3.7	4.0
Total	1984	2397	76.4	100.0	-	-	-

* For features entirely within the swath width (ie. not edge features)

Table 7. Ice type statistics based on analysis of underice data

The exception is form factor, which is a measure of the linearity, or alternatively, the 'roundness' of a feature and which was normally distributed. These results are militated by sample size. The samples of features are limited at both ends of their size ranges, at the lower end by the limit for rapid analysis and at the upper end by the width of the sidescan swath.

5.6 Sidescan Statistics of Association

5.6.1 Introduction

Familiarity with the appearance of Arctic ice fields suggests to most observers that ice elements do not occur in random sequence but that particular types of element tend to be juxtaposed. For example, larger frozen leads often have pressure ridges beside them that appear to have been generated by repeated partial closure and re-opening of the lead during its history. Thus, we might expect leads to be preferentially associated with pressure ridges, although the reverse would not necessarily be the case.

Similarly, one might suppose that a different frequency of pressure ridging occurs in first year ice than in multi-year ice.

To test such hypotheses quantitatively, two sequences of ice categories were considered, along lines parallel to the zenith and offset from it by 100m to each side. (This can be done along any other suitable line, between -350m and +350m.) The choice of lines avoided difficulties associated with the centre line and the occasional lack of continuity of features across it, as well as the lower contrast seen there.

Two transects of the sidescan swath were studied to enable a qualitative assessment of the stability of the resulting statistics. 100m offsets were chosen to maximise the quality of the data in the area of swath with the clearest image and to be as close to the zenith as possible so as to be within the area of the swath corrected using the upward-looking sonar. Whilst each transect represents a separate trial of the population, the size of some features means that the two trials are not independent.

A report detailing this analysis and entitled "Report on Statistics of Association of Features Generated from Sidescan Sonar Analysis", was issued in June 1990.

5.6.2 Analysis

By scanning through the scaled and rotated sidescan images along two lines, each 100m from the centre line, sequences of feature types were obtained along these lines. By definition, matrix is not present in these sequential lists of features, so the data were analysed to identify the regions along these lines where there existed gaps between features of greater than 15m. At each of these points, a feature of type matrix (Mx) was added. The threshold of 15m was chosen after consideration of the digitising accuracy and examination of a frequency histogram of the gaps between features. This procedure was checked by hand to ensure that matrix was correctly inserted between defined features. The resulting data sets were two sequences of features, along track for approximately 119km (for example: m,r,Mx,m,l,w,r,m,Mx,r,m,...).

5.6.3 Feature association

The resulting sequences were tested to see if features of a certain type (Type 'A') are more or less likely to be associated with features of another type (Type 'B') than could be accounted for if the sequences of features were random. The technique

employed and detailed results are discussed in the relevant report and submitted paper (Sear and Wadhams, 1991).

Some clear associations were seen that are not surprising. For example the two lead types (l and w) were strongly and significantly positively associated. Leads of either type were strongly negatively associated with ridges with a less strong negative association the other way (ridges with leads). This suggests that opening events are not the same events as those that build ridges. Alternatively, it may be that this area of the sea ice field has experienced only divergence during the events that created the local pattern of ridges and leads, in the period just before the data were collected. Thus, there would have been no cases of partial lead closure that would have built ridges along the edges of leads.

Matrix is positively associated with ridges. This is not surprising considering the sea ice environment of the study area and because matrix is defined as a non-linear ridged and hummocked underice surface. On the other hand, ridges are not significantly associated with matrix, confirming that the presence of matrix does not necessarily indicate the presence of identifiable linear ridging.

Interestingly, leads are significantly not associated with multiyear ice. This has a clear physical explanation, in that multiyear ice floes are stronger than younger, thinner ice and might be expected not to break preferentially, to form leads.

However, the converse relation between multiyear ice and leads does not support this conclusion. There is no clear preference for multiyear ice to be not associated with leads. Analysis of other data sets may resolve this ambiguity.

Similarly, while leads are strongly not associated with matrix, there is no converse relationship (matrix with leads), suggesting that matrix is as likely as not to occur next to a lead.

Not surprisingly, multiyear ice and first year ice are strongly negatively associated. Despite the paucity of firstyear ice in the study area, we accept this result as a confirmation that such a juxtaposition is likely to be unstable, as ridge building will be encouraged at the interface.

This line of enquiry is novel and requires a verified ice type classification, such as that derived for the first time in this study. Detailed analyses such as these may provide important

clues to the large scale physics of Arctic sea ice deformation responses to forcing.

5.6.4 A runs test for sequence data

A run is defined as a succession of identical features that are followed or preceded by features of different types, or no features at all. For example, the sequence:

.....,R,R,R,M,M,R,M,.... has a run of three Rs, then a run of two Ms, followed by a run of one R and finally a run of one M.

By counting the number of runs of each feature type and comparing the actual number with the expected number, the hypothesis can be tested that the sequence of like features is randomly distributed along track. A runs test was undertaken for both 100m offset tracks, discussed above and the results indicated that the distribution of runs is approximately random for all features except ridges and multiyear ice (see Table 8). Both ridges and multiyear ice show significantly more runs and hence smaller groupings (more regularly spaced features) than would be expected in a random sequence. This result does not indicate an association between ridges and multiyear ice. Also, it does not indicate that there is a preferred length scale for ridge building and multiyear floe splitting events in the region prior to data collection. It does show that in this data set, both ridges and multiyear ice fragments tend to come in ones, not often in pairs, triplets or other groups. For ridges, this suggests that each ridge building event tends to build one ridge, rather than a number of adjacent ridges. Explaining the multiyear ice result is more problematic, since having a number of multiyear fragments adjacent is only possible if they are separated by the thinnest of cracks (not delineated as separate features in classification). We expect that there would be a tendency towards separation of multiyear ice floes and thus a non-random distribution along track.

5.6.5 Ridge spacing

In the light of the results of the runs tests, the spacing of features was considered. This was done for ridges, that form a large data set along any one track within the sidescan swath. First, the frequency distribution of ridge spacing (between start positions of ridges) was determined along one of the 100m offset lines. Figure 2 shows the distribution of spacing. This approximates to a negative exponential distribution, except for ridge spacing less than 150m, where a log-normal distribution (not shown) provides a better fit, by eye. This is an expected result for Arctic sea ice ridges (Wadhams and Davy, 1986).

To verify these results, the positions of leading edges of ridges along the two 100m offset lines (Transects 1 and 2) were computed. In each case, the along track distance was split into 100m bins and the number of ridges that started in each bin were counted. No account was taken of ridge orientation, so that ridges crossing the transects that were nearly parallel to the submarine track would be much longer than others. Bearing this in mind, if the (leading edges of) ridges identified along track were randomly spaced, with a negative exponential distribution of spacing, then the frequency distribution of number per bin would be expected to fit a Poisson distribution. For each data set, the actual distribution of ridge starts per bin and the corresponding Poisson distribution were compared and Kolmogorov-Smirnov goodness-of-fit tests indicated no significant differences between the observed and expected probability distributions.

Type	Number of Runs	n_i	$E(r)$	σ^2	σ	z
100m Offset - Transect 1						
r	353	420	269	62	7.9	10.6
m	299	310	228	44	0.6	10.8
f	19	20	20	0.3	0.5	2.0
l	22	23	23	0.4	0.6	1.7
w	43	43	41	1.4	1.2	1.7
u	1	1	1	0.0	0.0	0.0
100m Offset - Transect 2						
r	291	343	222	51	7.1	9.7
m	230	243	182	34	5.8	8.2
f	18	19	19	0.4	0.6	-1.1
l	16	17	17	0.3	0.5	-1.4
w	38	39	37	1.4	1.2	0.4
u	2	2	2	0.0	0.0	0.0

Table 8. Results of two along track runs tests for features of like sea ice type. Note that, by definition, two or more areas of matrix cannot be adjacent. Significance at the 0.01 significance level is indicated by emboldening.

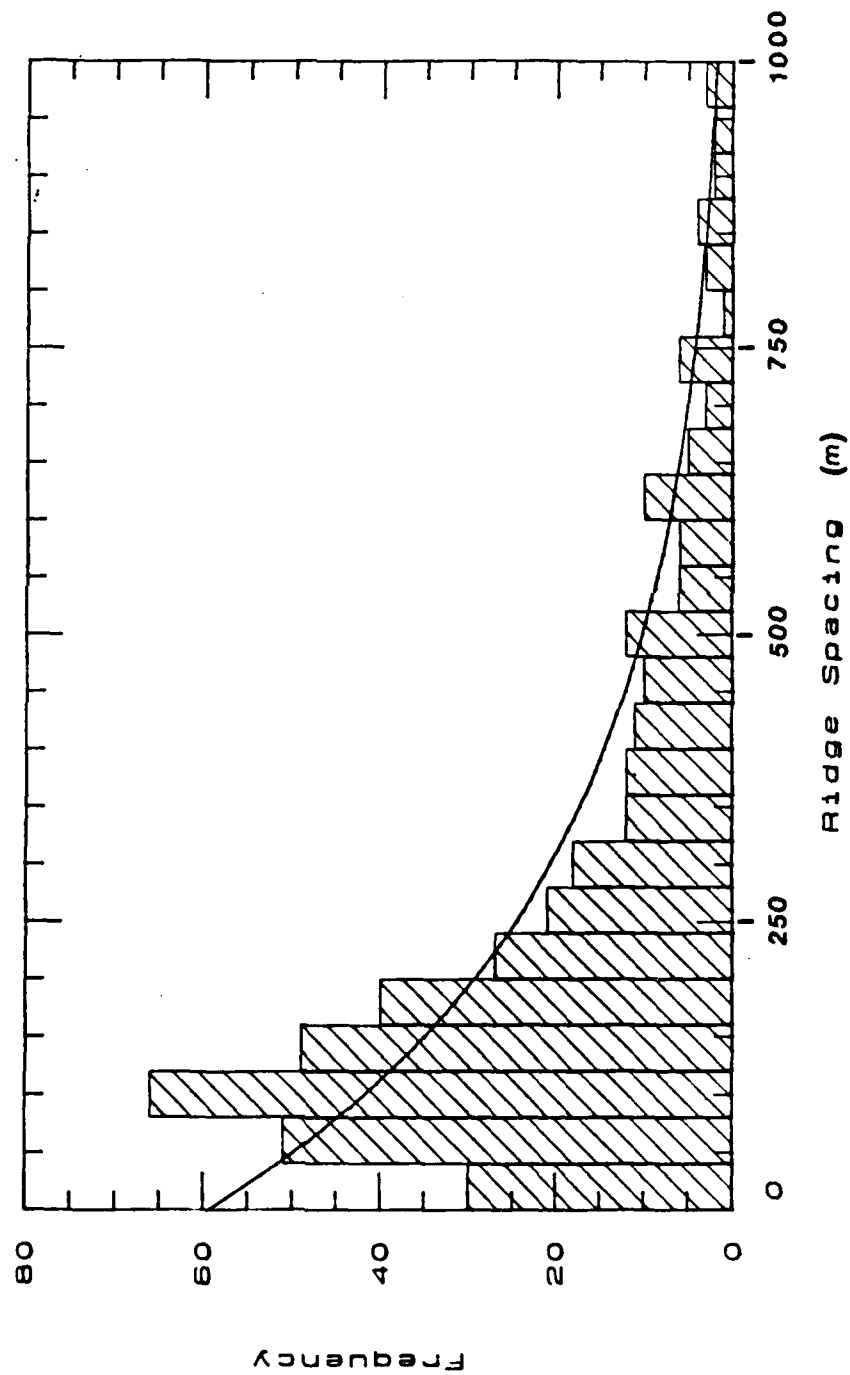


Figure 2. Frequency distribution of ridge keel spacing derived from verified, digital sidescan sonar 'maps'. Also shown is the equivalent negative exponential distribution.

These results indicate that ridges do fit a Poisson distributions, are randomly spaced along the track and thus that there was no obvious length scale of ridge building events in the study region or upstream of it, prior to data collection.

5.6.6 Ridge orientation

Information on ridge orientation is important operationally. Any directional anisotropy in sea ice roughness parameters would lead to a corresponding anisotropy in the mean strength of the ice cover, drag coefficient, its ability to generate internal waves and the rate of transmission loss for sound under ice.

The crest line of each ridge identified on the sidescan was placed on the overlay and it was possible to compute the orientations of pressure ridges that cut any given line. Here, four lines were chosen; the centre line of the sidescan swath, a line offset by 100m, a second line offset on the side at 300m and a corresponding line at -300m, on the other side of the centre line. The datasets are not independent but each represents a separate unbiased trial of the orientation distribution. Here, we will discuss the centre and 100m offset results. 173 ridges were observed along the centre line and 420 along the 100m offset, an indication of the data quality problems at zenith. The distributions of orientations along these transects are shown plotted in 10° bins in Figure 3.

Figure 3 shows that centre line orientations are peaked (with the main peak in the 60° - 80° range) relative to the sine curve that should be seen for a random distribution. The 100m offset orientations are also peaked at 60° - 80° but with a smaller deviation from randomness. We suspect that the ridges along the centre line are subject to data quality and detectability problems as already described and the smaller number implies that they are a selected group. Thus, the 100m offset distribution is considered to be more representative of the data set as a whole. It appears not to differ significantly from a random distribution, except for the peak at 60° - 80° . This peak is evidence of a preferred ridge orientation to match the preferred lead orientation, discussed later.

This result is derived using ridges encountered along a single line, sampling relatively few of all the ridges present in the complete sidescan data set. Because the orientations of all identified ridges were output as a product of the classification and digitising procedure, it is possible to consider a larger set of ridge orientations (θ), determined relative to the direction of movement (eastward). Figure 4 shows the frequency

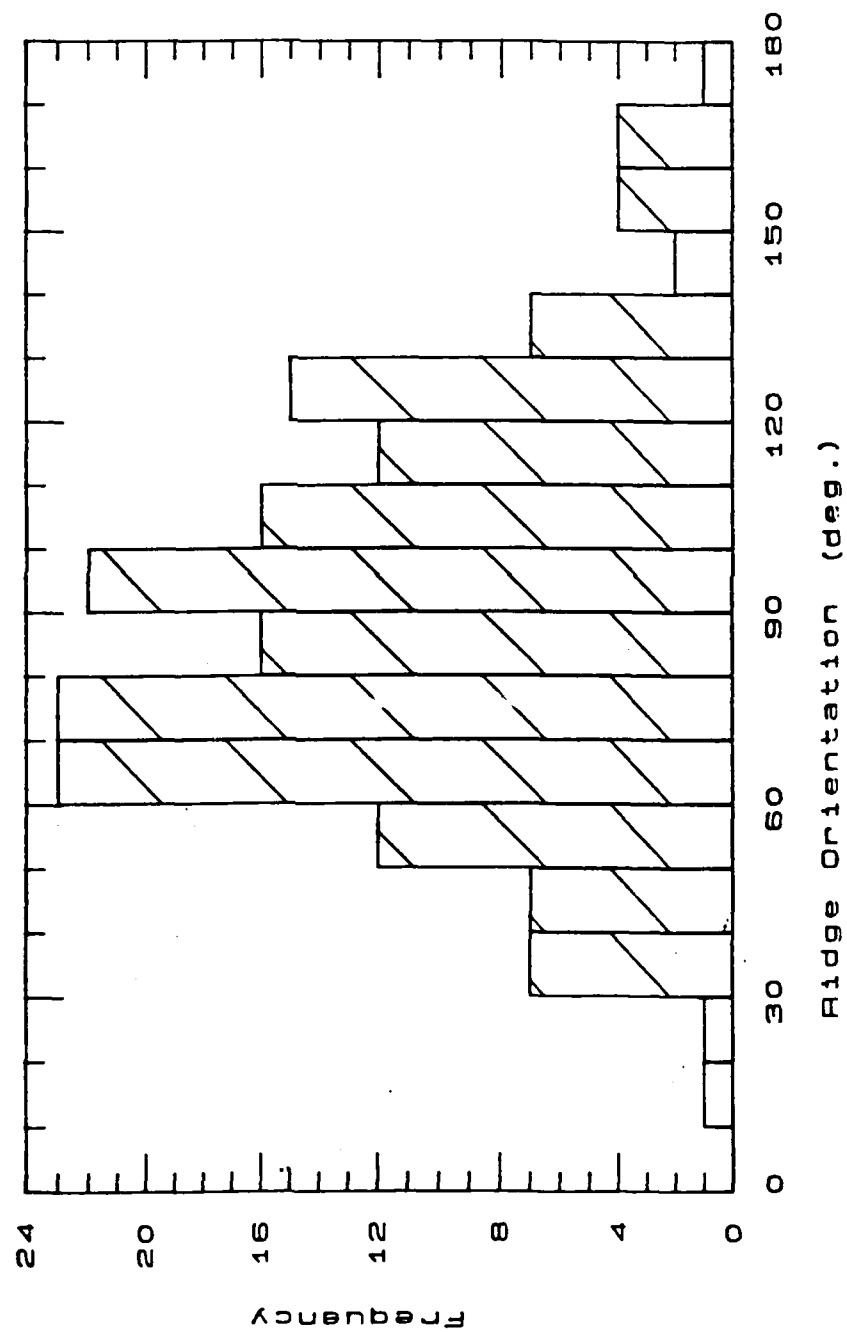


Figure 3. Frequency distribution of ridge keel orientations seen along the centreline of the sidescan swath and derived from verified, digital sidescan 'maps'.

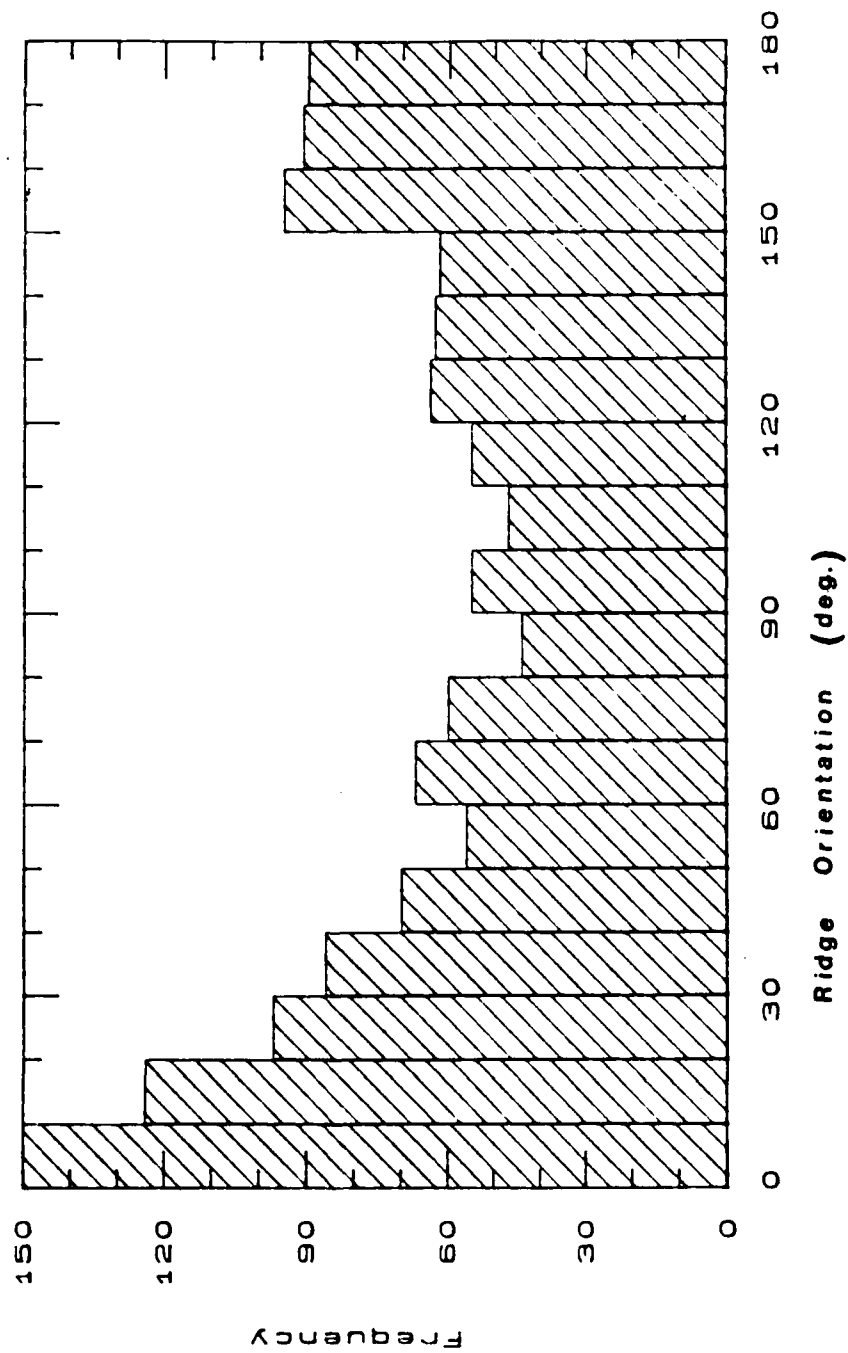


Figure 4. Frequency distribution of the orientations of all ridge keels seen in the sidescan record and derived from verified, digital sidescan 'maps'.

of all ridge 1378 orientations in the record. The frequency distribution appears quite uniform but with a tendency to dip in the centre, near $\pi/2$.

For a randomly orientated ridge field in two dimensions, we expect a uniform distribution on the sidescan image so long as the swath is wide enough to make the image truly two-dimensional, that is relatively few ridges with cross-track lengths greater than 673m. As this was not the case, the theoretical random distribution should lie between the $(\sin\theta)$ relationship of Figure 3 and uniformity. Folding the distribution in half so that its limits are 0 and $\pi/2$ indicates a reduction in sidescan detectability of ridges as the ridge orientations approach $\pi/2$ (ie. normal to the submarine track). This is expected since the shadows produced by such a ridge are just the relief shadows of individual blocks, whereas for a ridge parallel to the track, the entire ridge casts an acoustic shadow on the undeformed ice behind it.

5.6.7 Analysis of leads

5.6.7.1 Introduction

A manual analysis was carried out of every lead that crossed the centre line of the sidescan swath. The average orientation of each lead within the image width was measured. The position of the western edge of the lead when it crossed the centre line was recorded. The width of the lead at right angles to its major axis was measured at regular intervals along the axis, giving typically ten to twelve independent measurements of width for each lead. Finally the absolute position of the start of each lead was noted and their spacing analysed.

5.6.7.2 Lead orientation

The distribution of orientations of the 38 leads occurring in the original 140km sample of classified sidescan was studied. If leads were randomly orientated and had lengths independent of orientation, then the frequency of encounter, along any given track would be proportional to $\sin\theta$, where θ is the angle between the lead axis and the line. The observed distribution of leads differs considerably (though not significantly) from randomness. The distribution is strongly peaked in the range 60° - 70° (relative to north), indicating a preferred northeast to southwest orientation in this region. Lead detection should not be dependent on orientation (unlike ridges).

Variation of lead orientation with distance was also examined. Figure 5 shows the orientation of each lead plotted against the

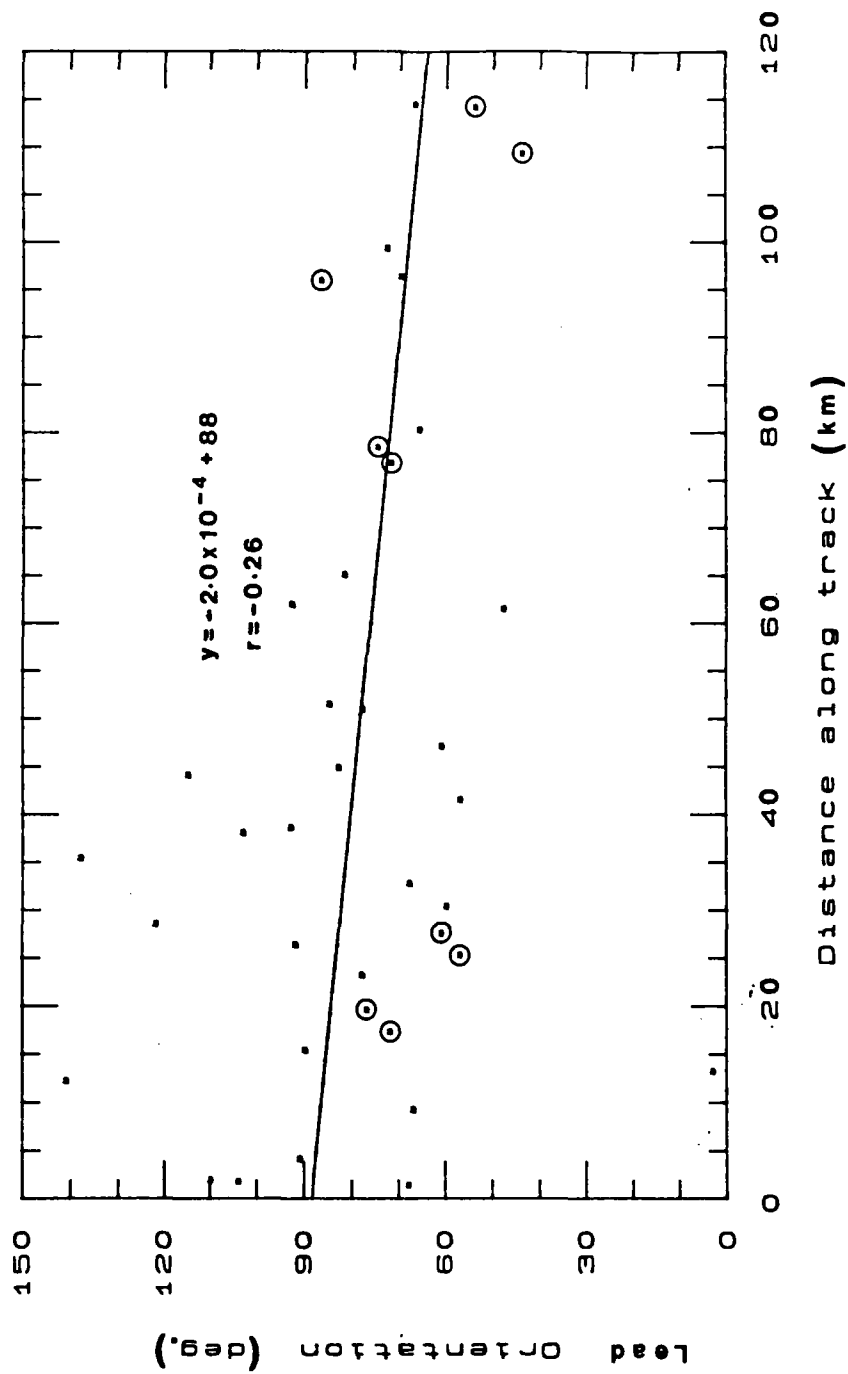


Figure 5. Lead orientation by distance along track for all leads identified from the verified, digital sidescan sonar record. Also shown is the appropriate regression equation. Leads wider than 100m wide are marked with circles.

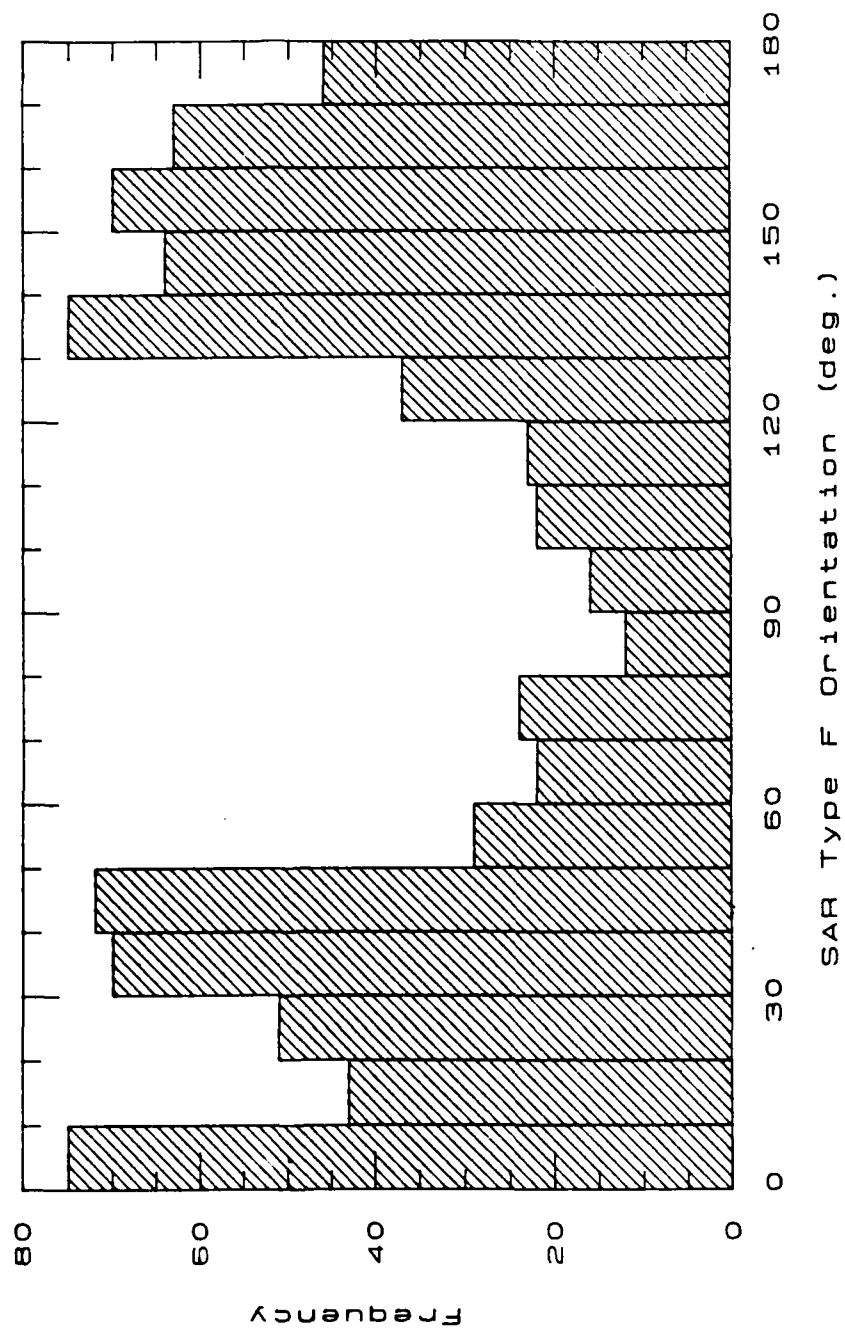


Figure 6. Frequency distribution of all SAR Type F feature (possible ridge sail) orientations, derived from the digital SAR 'map'.

along track distance (km) at which the lead crossed the centre line. Leads wider than 100m are shown with a circle, narrower ones by a dot. Figure 5 indicates both clustering and a trend. The lead orientations are not widely scattered. There is clustering around a linear trend, with θ decreasing along the track. The best-fit regression line through the data is also shown on Figure 5. It seems that the stress system that gave rise to the leads was slowly changing in direction, with a wavelength greater than 140km. Figure 5 also indicates a tendency for leads to become less frequent with increasing distance, showing that the sea ice field may have been less divergent in the eastern part of the area. We conclude from the submarine data that there is evidence of a non-random distribution of lead orientation that matches that of ridges.

5.6.7.3 Lead width

The overall mean width of the 38 leads in the sidescan data set was 79.4m and their median width was 35.3m. The small number of leads in the sample makes it impossible to test this dataset for fit to a functional form. However, the dataset is unique because all other published lead width distributions (for example, Wadhams and Horne, 1980; Wadhams, 1981) consist of along track lead widths derived from upward-looking sonar data, rather than real widths measured at right angles to the lead axis, along a significant length of that axis.

Table 9 compares the exceedence frequency of these data with two other published datasets, from the Beaufort Sea in April 1976 (USS Gurnard: Wadhams and Horne, 1980) and M'Clure Strait in February 1960 (USS Sargo: McLaren, Wadhams and Weintraub, 1984). The results from the 1987 exercise are remarkably similar to the 'Sargo' distribution and not dissimilar to the 'Gurnard' results.

The main difference is the lower frequency of narrow leads (less than 50m wide) detected by the sidescan sonar in 1987. Probably, this results from the classification technique, in that narrow cracks were often incorporated into the floe of which they formed part, whereas on an upward-looking sonar record they would be detected and recorded as separate entities. The similarities among these three datasets strongly suggest that there is some natural function governing the width distribution of leads, applicable throughout the Arctic.

Minimum Lead Width (W)	Mean distance (km)		
	These data North of Greenland (May 1987)	'Sargo' M'Clure Strait (Feb. 1960)	'Gurnard' Beaufort Sea (Apr. 1976)
0	3.0	1.3	0.2
50	7.2	7.4	10.3
100	11.4	12.2	24.1
150	19.1	18.9	38.4
200	28.6	25.0	67.6
500	114	100	237

Table 9. Lead width exceedence frequencies from this sidescan sonar derived data set, compared with two previous data sets, derived from upward-looking sonar. Mean distances between encounters with a lead of width at least W metres are tabulated.

5.6.7.4 Lead spacing

If leads are placed randomly, the distribution of spacings between successive leads along a given line should be a negative exponential. The 38 leads in this sample have a spacing distribution that differs from random.

5.6.8 Summary

By turning the original sidescan sonar chart roll image into an ice type map, we can test hypotheses about the nature of the sea ice morphology in the Arctic. This adds value because we are dealing with the under surface of the ice cover. Beneath sea level is where most of the sea ice volume is located and the underice surface is important operationally. Before this exercise, the underside of the ice was inaccessible to such analyses. In conclusion, there are a number of important positive and negative associations between juxtaposed features of the sea ice underside. The significance of these associations would be confirmed or denied by further analysis. Also, it has been shown that ridges and multiyear ice features tended to occur singly, separated by other ice types, rather than being clustered randomly along track.

Lead Spacing (km)	Number
0 - 1	8
1 - 2	6
2 - 3	14
3 - 4	3
4 - 5	1
5 - 6	1
6 - 7	0
7 - 8	0
8 - 9	0
9 - 10	2
10 - 11	0
11 - 12	1
12 - 13	0
13 - 14	0
14 - 15	0
15 - 16	1

Table 10. Distribution of lead spacing in the 140km sidescan sonar data set.

As Table 10 shows, the distribution is strongly peaked in the range two to three kilometres, suggesting that the lead system in this region was created by a single stress event, represented by a slowly varying stress field of high spatial coherence and of roughly uniform magnitude. It seems that there was a preferred distance over which a single lead-opening event is capable of relieving the stress upon the sea ice field.

Analysis of the pressure ridge orientations showed they did not differ greatly from random but may have a similar orientation to the leads. The spacings of pressure ridges was a good fit to a log-normal distribution. The spacing of ridges along track appears to be random, as the spacing distribution is

approximately negative exponential and the distribution of ridges in discrete bins is Poisson.

Lead orientations were non-random, being concentrated within a narrow band of angles in a generally NE-SW orientation. This preferred orientation changed slowly along the length of the sample, implying a causative stress mechanism with a characteristic length scale exceeding 140km. Lead widths did not fit a simple distribution but did agree well with earlier measurements made in the Arctic in winter. Finally, lead spacing was not random, being primarily in the range 2 to 3km.

5.7 SAR Classification

The SAR data were available as a digital image on magnetic tape. The imagery was analysed using an in-house GEMS image analysis system. That portion of the SAR image that encompassed the region of best collocation was identified and extracted. By identifying unambiguous tie points on the SAR image, the route of the platform could be determined. To do this, it was necessary to assume that the platform moved in a straight line between tie points. Using this method, a swath of 727 metres wide (47 SAR pixels) was extracted and straightened, to give an area similar to (but slightly larger than) that of the sidescan swath.

The SAR image was then contrast stretched to aid classification of the ice types. The extracted image was image-written and enlarged to enable classification of the SAR and subsequent digitising. When SAR areal statistics were generated (see Section 5.8 below), the full 727m wide swath was used but when direct comparison with sidescan was undertaken, the SAR map was trimmed to average 673m wide (the average width of the sidescan swath). The SAR map started 1.17km into the sidescan map.

The enlarged hard copy SAR image (covering roughly the same area as the length of sidescan) was classified manually according to pixel brightness and image texture. No attempt was made to classify SAR according to ice type or possible sea ice related features. This was a deliberate policy, to reduce to a minimum the possibility of bias in the SAR classification. The classification scheme used for the SAR imagery was:

Class A: Very dark return (black) features, tending to have some linearity.

Class B: Dim black / dark grey, slightly mottled (only a shade lighter than A) seen along edges of A, or replacing A in narrower linear features.

Class C: Light grey regions with some texture and faint lines running through them (a shade lighter than B). This class tends to be along the edge of Classes A and B and may be floe shaped. This class does not include clear lineations.

Class D: Faint lineations within C (similar to F below but fainter).

Class E: This class includes non-linear (floe-) shaped regions with a mottled strong mid-to-dark grey return. The region has a textured, or bumpy, appearance, the degree of which is variable. Very faint white lines across a uniform area may be included in this region.

Class F: Narrow linear lines of very bright (white) return.

Class G: The remaining area is 'matrix', a mottled region of mid-grey and white returns suggesting a bumpy non-linear terrain with no distinct shape.

A class for unclassifiable regions is not needed on SAR because the image quality is uniform across the swath. While no attempt has been made to assign ice types to the classes listed above, we might expect the following associations:

Class A may represent, or be associated with, open water or frazil ice within a lead. Class B may represent refrozen lead. Class C may represent firstyear ice. Class D may represent ridge sails in firstyear ice. Class E may represent multiyear ice. Class F may represent ridge sails.

The classified SAR feature map was digitised in the same way as the classified sidescan data.

5.8 SAR Statistics

Statistics of the SAR features (A to G) were generated in the same manner as described earlier for sidescan. The areal fractions are shown in Table 11 and these are compared with those of the sea ice types derived from sidescan imaging over the same area. Overall, the SAR imagery indicated that Type G covered 49.7% of the study area, Type F 9.5% and Type E 29.5%. Types A to D accounted for 11.3% in total (Table 12).

Ice 'Type'	Number		Total Area (incl. edge) (10 ⁶ m ²)	Areal Fraction %	Areal Statistics (10 ³ m ²)*	
	Within Swath	Total (incl. edge)			Mean	St.Dev
A	10	28	0.90	1.00	32.2	62.4
B	130	228	3.84	4.27	16.8	31.2
C	100	204	5.04	5.59	24.7	29.1
D **	55	62	0.34	0.38	5.5	3.2
E	352	620	26.60	29.54	42.9	61.4
F	658	826	8.57	9.52	10.4	-
G	-	-	44.75	49.70	-	-
Total	1305 +	1968 +	90.04	100.00	-	-

* For features entirely within the 700m swath width (ie. not edge features)

** Lineations within Type C

+ Does not include residual class - Class G (matrix)

Table 11. SAR sea ice surface classification for the same region as the underside was classified using sonar data.

Sidescan		SAR	
Type	% Area	Type	% Area
Lead w	1.1	A	1.0
Lead l	1.9	B	4.3
Firstyear	1.8	C	5.6
		D*	0.4
Multiyear	29.7	E	29.5
Ridge	14.7	F	9.5
Matrix	49.7	G	49.7
Uncl'fd	1.1	-	-
Total	100.0	Total	100.0

* Lineations within C

Table 12. Comparison of SAR classification with sidescan classification along 119km of best collocation.

The Type F (possible ridge sail) orientation distribution dipped close to 90° , i.e. normal to the aircraft track (Figure 6), in a similar, though much more noticeable, way to that indicated by the validated sidescan, for ridge keels.

The data swath is wide enough that, for the case of random ridge sail orientations, we would expect a uniform distribution of observed angles. The observed result suggests that ridge sails observed on SAR have a strong tendency to lie parallel to, or rather within an angle of between 0 and 50° from, the line of flight. This is likely to be a function of the way that SAR images sails and thus indicates either that not all sails present are being detected by the SAR, or indeed that Type F is not necessarily equivalent to ridge sails seen *in situ*. This lends a cautionary note to further comparative analyses.

Assuming that the actual distribution of sails is at least as uniform as indicated by that of ridge keels and that SAR images ridge sails as bright linear features (which one expects), then a large proportion of sails are missed by the SAR.

Type B features (possibly refrozen leads) had a distribution that was strongly peaked at the low end, while the distribution of Type F (possible ridge sails) was not significantly different from that of a two parameter log-normal. Type E (possibly multi-year floes) and Type C (possible first year ice) also fitted log-normal distributions. Thus it appears that the log-normal has some general validity for describing the distributions of floe area and of bright linear features (possibly ridge sails). The absolute feature numbers in the case of the present dataset are too small to confirm the validity of the log-normal over all other distributions.

In the same way as was done in our analysis of the sidescan imagery, SAR Type F features were extracted along a transect, a total of 176 features. The spacing between individual Type F features (from start to start) was investigated. The mean spacing was 668m, the median was 351m. Figure 7 shows the distribution of spacings. It illustrates the close fit of the observed distribution to a two parameter log-normal distribution. Indeed the observed distribution was found to be insignificantly different from a log-normal. The spacing data were also compared with a negative exponential (not shown) but the fit was not as good because of the fall off in the frequency of spacings below 100m. For longer spacings, the observed distribution closely matches a negative exponential and thus indicates that Type F features were distributed approximately randomly along track.

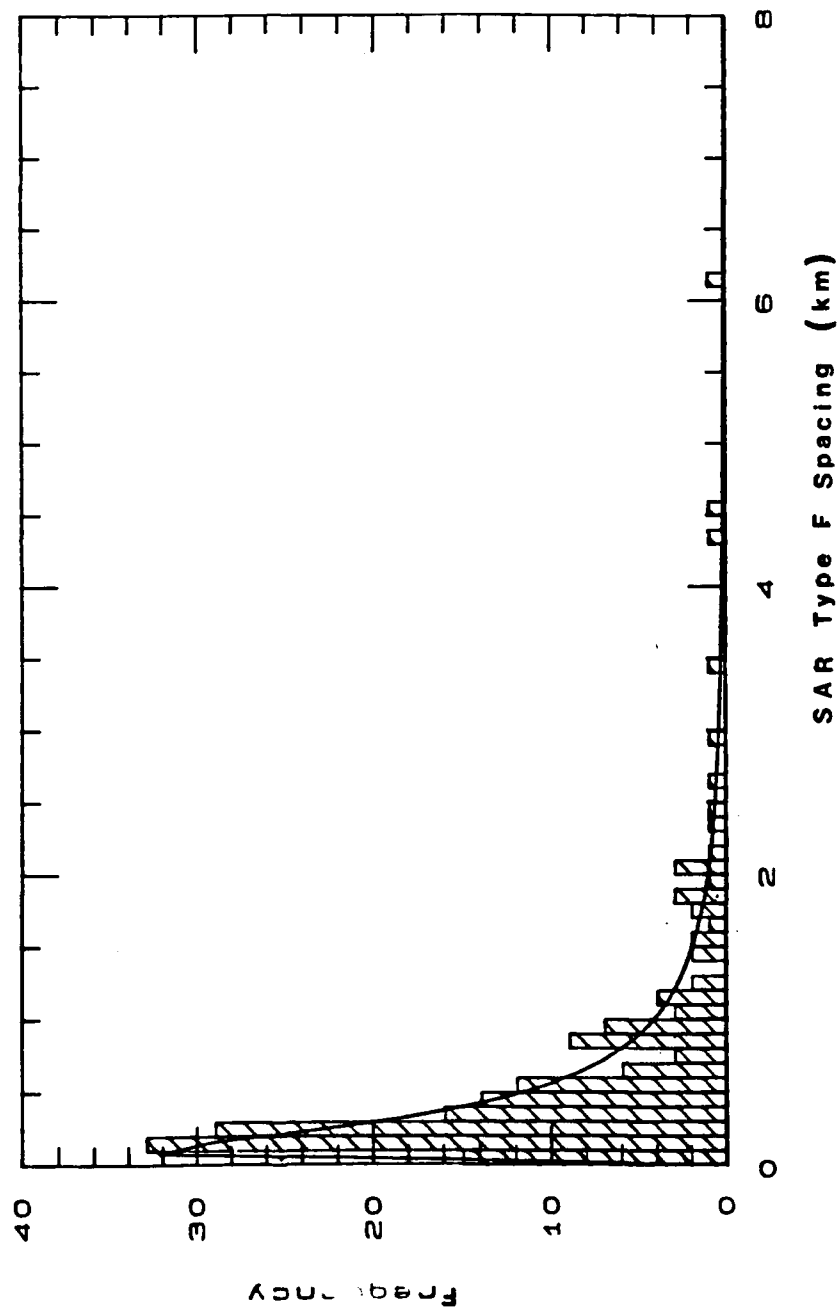


Figure 7. Frequency distribution of SAR Type F feature (possible ridge sail) spacing, derived from the digital SAR 'map'. Also shown is the appropriate log-normal distribution.

5.9 Sidescan / SAR comparison

The comparison of the SAR and sonar-derived ice classification is detailed in a paper in preparation (Wadhams and Sear, 1991). The present draft of this paper is included here as Appendix III. Below, the work is summarised and the results outlined.

5.9.1 Areal fractions

Table 12 compares the areal percentages of SAR 'types' with those of sidescan, discussed earlier. The difference in total area (Tables 7 and 11) is explained by a) the 6.36km gap in the sidescan record and b) the difference in the sidescan and SAR swath widths used.

As Table 12 shows, the same proportion of the study area is covered by Type G as by Matrix. Also, the areas of multi-year ice and E are the same. This correspondence between imagery classified independently is very encouraging. It confirms that X-band SAR successfully distinguishes multi-year ice and rubble fields. Similarly and as expected, the SAR distinguishes dark leads (open water). As expected, using X-band SAR, it is less easy to tell apart refrozen leads and first-year ice. Finally, as suggested by analysis of orientations, the X-band SAR appears not to image ridges in the same way as does the sonar. The area of possible ridge sails on the surface is significantly smaller than that of keels, suggesting that the two types do not correspond (one-to-one).

5.9.2 One-to-one feature comparison

5.9.2.1 Methodology

A feature-by-feature comparison was undertaken using the transparent overlays of sidescan and SAR 'maps'. These were to the same scale and covering the same region, representing the classification of the ice surface (based on an interpretation of SAR) and ice types based on the underice surface (derived from a validated sidescan map). If the collocation were perfect and if the upper ice surface as classified from SAR perfectly matched the lower ice surface as classified from sonar, then we would expect the two sets of transparencies to show a 1:1 correspondence between areas covered by a particular sidescan ice type and a particular SAR surface type.

Perfect correspondence was not expected because of the less than perfect matching of the images on a scale of metres or tens of

metres, the fact that there is a genuine difference between the geometry of the upper and lower ice surfaces and because the sidescan and the SAR image the ice in different ways. [Sidescan responds almost entirely to the surface gradient of the ice. Thus, it is best at displaying roughness and texture. On the other hand, SAR responds both to surface roughness and to the conductivity profile in the upper layers of the ice cover. Thus, it so shows distinct differences between ice of different thicknesses and ages but similar roughness.]

The quality of match between the two sensor outputs was tested. The reference ice type chosen was pressure ridges, identified on sidescan. Ridges were chosen because, in the validation testing of the sidescan against upward-looking sonar, almost all features identified as pressure ridges on sidescan really were pressure ridges. These areas could then be matched against SAR to see whether there was a statistically valid preferred ice type in the SAR that occurs in the same locations as the ridges on sidescan.

Working between tie points, the sidescan overlays were fitted over the SAR transparencies as closely as possible. Small adjustments were made only if some very clear feature such as a lead was present, that can be expected to give perfect correspondence between top and bottom (except for the effect of relative motion during the few hours between the collection of the two datasets). For every ridge on sidescan, the estimated fractions in tenths of the area of the ridge underlain by different SAR ice types was recorded. A total of 1364 ridges were examined on 74 frames of sidescan (corresponding to 119km of track). Every ridge was given the same weight regardless of size. The results were compared with the overall relative areas occupied by different ice types on the whole SAR dataset, to see whether the 'hit rate' exceeded chance expectation. It was assumed that hit rate would be independent of ridge size. This was a conservative assumption since we expected large, prominent ridges to match better than small ridges.

5.9.2.2 Results

Data were analysed for groups of ten frames (each corresponding to about 15km of track) to test for repeatability and were then combined. The overall results are shown in Table 13 and indicate associations (positive or negative) between SAR ice types and the location of ridging on sidescan. Two significance levels are listed for each association. The first assumes that each association can be tested independently and the second (more conservative) assumption is that since seven statistical

tests were carried out in aggregate, the significance level of an individual test should be reduced by a factor of seven. As an example, the results for SAR Type F are explained here. Classification F showed the strongest positive association with sidescan ridges. Table 13 indicates that 9.52% of the area of the whole ice field (as seen by SAR) is occupied by ice of type F. If there was no association between sidescan and SAR images, 9.52% of the area of ridged ice on the sidescan image would be overlain with Type F. In fact, 17.07% of the sidescan ridged ice is underlain by Type F using a sample of size 1364. The observed percentage is 9.49 standard deviations away from that expected by chance. This is a departure that is significant at better than the 0.01 level (1% level). Since the same test is applied to seven ice types, a conservative reduction in significance level gives a result for Type F that is still significant at better than the 0.01 level.

From the results shown in Table 13 the following conclusions are drawn:

1. The spatial coincidence between sidescan ridges and SAR ice classifier F is highly significant.
2. There is a positive association between sidescan ridges and SAR ice type C, significant at the 0.01 level.
3. There are negative associations between sidescan ridges and SAR ice types A and E, which are significant at the 0.01 level.
4. There is a negative association between sidescan ridges and SAR ice type G, which is significant at the 0.05 level.
5. There are no significant relationships between the occurrence of sidescan ridges and SAR ice types B and D.

The positive association between ridges and Type F is only twice the level expected by chance. This may indicate that while, in many cases the same features were identified, they were not orientated in similar directions on the top and bottom surfaces of the ice. On occasion, major lead systems are well collocated but individual ridges and areas of multiyear ice observed using the sonar are hard to match to similar features seen on the SAR. Many SAR Type F features are not seen on the sidescan and even where ridges and Type F features are observed in the same region individual features can not be unambiguously matched.

Ridges Present	Ridges Overlain by SAR Types						
1364	A	B	C	D	E	F	G
Number	1.7	46.5	102.1	10.7	338.7	232.8	631.5
Percentage	0.1	3.4	7.5	0.8	24.8	17.1	46.3
Total % Area of Type	1.0	4.3	5.6	0.4	29.5	9.5	49.7
Significance Level:							
Independent	<0.002	Not	<0.002	<0.01	<0.002	<0.001	<0.01
Aggregated	<0.01	Not	<0.01	Not	<0.01	<0.001	<0.005

Table 13. Results of matching SAR map transparencies to areas occupied by ridging on corresponding sidescan map transparencies

5.9.2.3 Discussion

It is gratifying that a strong positive association is found between the occurrence of ridging on the ice underside and the perception of a bright linear feature on the topside that, *a priori*, could be assumed to be a prominent ridge crest (SAR Type F). However, the observed occurrence is only about twice the level expected by chance, so the coincidence of imagery is not perfect. This imperfection is due to a combination of small-scale mismatching in the final image overlaying, to possible ridge sail crests (SAR) and ridge keel crests (sidescan) being angled differently and to a real failure of ridges always to be identifiable on the upper and lower surfaces using these sensors.

The second positive association, between sidescan ridges and SAR Type C, is more problematic. Type C ice is light grey, floe-shaped, with some texture and with faint lines running through it. Where possible, the lines were extracted and classified separately as Type D. *A priori*, we expect Type C to be first year ice and that the lines are either first year ridges or else correspond to the cracks that are observed to criss-cross first year floes on the underside. Such cracks would be strong targets for SAR and because SAR penetrates the ice vertically, the aperture synthesis process may give such a feature an apparent width in a SAR image that is greater than

its real width. Nevertheless, it appears that Type C ice corresponds significantly to ridged area on sidescan. This implies either that the faint lines, even when not separated, are indeed first year ridges, that are wider underneath than on the upper surface, or else that the entire area of Type C corresponds not to first year floes but to ridged ice of some characteristic kind. The negative associations, of ridges with apparent open water and multi-year ice reasonable and understandable and the insignificant associations seen between Type F and some of the SAR types may be a function of the small sample sizes.

Qualitatively, an excellent match between prominent features on each type of image might occur in some location and a match of similar quality would occur perhaps three or four kilometres downstream but the intervening region might show no match at all. This could not have been because of local mismatch in collocation but appears to be because the terrain consisted of a nondescript heavily deformed rubble, that was difficult to categorise both on SAR and sidescan. The data were obtained in the heavily ridged area north of Ellesmere Island and much of the region comprised rubble with few undeformed floes visible. This reduces the effectiveness of analysts in obtaining matching and suggests that a similar analysis should be done of coincident imagery in a less strongly ridged region of the Arctic.

Also worthy of note is that in areas where an excellent matching of transparencies could be achieved because of the presence of a characteristically shaped lead, the coincidence of ridges was no better than in the dataset as a whole. This implies that there is a real difference between ridge identifications from each sensor.

Finally, it was observed in a few cases that a sidescan ridge of prominent and distinct shape was coincident with a SAR feature of similar distinct shape and yet the SAR classification was B, C or D rather than F.

5.9.2.4 Conclusion

Although there is a significant correlation between SAR and sidescan as far as ridge identification is concerned, the correspondence is not 1:1. Under-ice features which we know to be ridges can correspond to above-ice SAR signatures that are variable enough to lead an observer to place them in a number of different categories. This must lead to continuing caution in attempts to quantitatively interpret SAR imagery in terms of ice type. Further validation studies are needed. For example, it

appears that the true nature of the upper surface and particularly of ridges, can not be seen using a single X-band SAR image. Thus, we strongly recommend that a region should be imaged by two SAR flights at right angles, better to pick out all possible ridge sails, whilst coincident underice sidescan and upward-looking data are collected that give the most reliable large scale ice type data possible.

6 DATA PACK

A key aspect of the work undertaken during this year was to produce a useful package consisting of all major data sets, covering the best region of collocation of all data sets. The generation of a data map (discussed earlier in this document) provided the information required to define that region for further analysis. The data pack was delivered to ONR, directly from SAIC Cambridge in mid-1990. It was classified as 'UK Confidential' (but see the letter attached to the data pack) and consists of the data sets used in this year's analysis (sidescan, upward-looking sonar and SAR data) and others (for example AMMR and AOL) that remain to be correlated rigorously with submarine and SAR data over the region of best collocation.

The sidescan chart roll was digitised and classified in sections representing approximately 700 x 1500m (as described above). 50 features were matched on the SAR and sidescan to provide a list of tie points. Unambiguous positions were achieved for 40 of these tie points. The digitised sidescan data were converted to distance along track (in metres) using the tie point information.

The submarine track and the sidescan swath were marked on the SAR image and that portion of the SAR image corresponding to the sidescan swath was digitised. The digital SAR data were then converted to distance along track (in metres), so that these data coincided with the digital sidescan data. In order to overlay either the digital sidescan or digitised SAR features on the SAR image, it was necessary to convert digital data from distance in metres along track to SAR pixel locations. This was achieved using the appropriate tie point data.

The upward-looking sonar data, representing sea ice draught at 1m intervals along track) were tied to the SAR image by another set of tie points. These tie points can be used in a similar manner as described above to overlay the upward-looking sonar data onto the SAR imagery.

The data pack consists of a VAX compatible magnetic tape containing the following files:

- 1 SAR image as supplied to SAIC by JPL.
Filename: JPLSAR.BIN
- 2 SAR image with overlaid AMMR, AOL and submarine data tracks.
Filename: ALL.BIN
- 3 Extracted and straightened portion of the SAR image to match the submarine sidescan swath.
Filename: SWATH.BIN
- 4 Tie point data used to collocate the sidescan and SAR.
Filename: TIEPOINT.DAT
- 5 Digitised sidescan sonar feature map.
Filenames given in: SSNAMES.LIS
- 6 Digitised SAR feature map for same area as Item 5.
Filenames given in: SARNAMES.LIS
- 7 AMMR data corrected for collocation with SAR.
Filename: AMMRCORR.DAT
- 8 AOL data corrected for collocation with SAR.
Filename: AOLCORR.DAT
- 9 Upward-looking sonar data for the same section of submarine track as the digitised sidescan sonar feature map.
Filename: UL.DAT
- 10 Tiepoint data used to collocate the sidescan and SAR with the UL data.
Filename: ULTIEPTS.DAT
- 11 An example Fortran program for reading SAR data.
Filename: BINREAD.FOR

The data pack also included the following items:

- 12 A contact print of Item 2 (ALL.BIN), showing tracks on the SAR image.
- 13 A listing of the VAX save set.
- 14 Accompanying documentation.

Details of the data pack data formats, including those of the SAR imagery and AMMR data are given in the documentation supplied with the data pack (Item 14 above).

7 SUMMARY

The project described above resulted from a unique experiment, undertaken in the Arctic in Spring 1987. Arctic sea ice from north of Ellesmere Island to Fram Strait was remotely sensed from above below, using aircraft and submarine-borne sensors. Data collocation was achieved over a large region in the region north of Ellesmere Island (between approximately 60 and 140km long and 700m wide) for various combinations of sensors.

Work undertaken and completed in 1989 has been discussed briefly in this report and is referenced in two papers (in press). Work completed during FY 1990 is discussed more fully here but is also referenced in two team papers (one submitted and one in preparation) and a further two submitted by one member of the project team. During FY 1990, SAIC has submitted reports on individual aspects of the analysis undertaken this year.

During FY 1989, technical work was concentrated on a detailed statistical comparison of various remotely sensed data for a 20km and a 60km section. Also 3500km of upward-looking sonar data were analysed statistically and work began on analysing the underice surface in wave number space.

During FY 1990, the analysis of the ice in wave number space was completed and technical effort was concentrated on a rigorous comparison of sonar and SAR-derived ice classifications for a region of best collocated data. The under-surface of the sea ice field over 140km x 700m has been classified and that classification verified by using submarine sonar. Areal statistics of the underice surface have been generated. The available data afforded an opportunity to compare airborne remotely sensed data, interrogating the ice surface, with the underice data. These latter data providing the most reliable classification of sea ice yet available for such a large area. The efficacy of X-band SAR imaging of the upper ice surface was tested with respect to known ice types and the results presented have implications for SAR imaging of sea ice fields that are generally applicable.

A data pack has been produced and issued. This consists of processed data from all major sensors, for the region of best

collocation. The data pack is a valuable resource for future multisensor study of the region and is lodged with ONR.

8 PROGRAMME STATUS

The list of Phase III Continuation tasks in the Scope of Work was modified slightly, as described in this document, in order to ensure that the technical work carried out was relevant to the needs of the funding agencies and was of the highest quality. The work completed, including the issuance of several project reports and the submission of a scientific paper (one further pending), satisfies the project requirements as outlined in the Scope of Work.

9 ACKNOWLEDGEMENTS

This report was prepared by Dr C Sear. The technical effort described was coordinated by Dr Sear, in collaboration with SAIC's consultant, Dr Wadhams. Unless otherwise stated the work was undertaken entirely by SAIC Cambridge staff (including Dr Sear, Ms A Scoon, N Flack, M Fearon and D Evans) and Dr Wadhams. Administrative support in Cambridge was given by Ms M Cowan and managerial support by A Cowan.

10 REFERENCES

- Comiso, J.C., P. Wadhams, W. Krabill, R. Swift, J. Crawford and W. Tucker 1991. Top/bottom multisensor remote sensing of Arctic sea ice. *J. geophys. Res.* In Press.
- Hibler, W.D. III, W.F. Weeks and S.J. Mock 1972. Statistical aspects of sea ice ridge distributions. *J. geophys. Res.*, 77, 5954-5970.
- McLaren, A.S., P. Wadhams and R. Weintraub 1984. The sea ice topography of M'Clure Strait in winter and summer of 1960 from submarine profiles. *Arctic*, 37, 110-120.
- Sear, C.B. and P. Wadhams 1991. Statistical properties of Arctic sea ice morphology derived from sidescan sonar images. Submitted to *Progress in Oceanography*.
- Wadhams, P. 1981. Sea-ice topography of the Arctic Ocean in the region 70°W to 25°E. *Philosophical Transactions of Royal Society London*, A302, 45-85.
- Wadhams, P., J.C. Comiso, A.M. Cowan, J. Crawford, G. Jackson, W. Krabill, R. Kutz, C.B. Sear, R. Swift, W.B. Tucker and N Davis 1991. Concurrent remote sensing of Arctic sea ice from submarine and aircraft. *Int. J. Remote Sensing*. In press.
- Wadhams, P and T. Davy 1986. On the spacing and draft distributions for pressure ridge keels. *J. geophys. Res.*, 91, 10697-10708.
- Wadhams, P. and R.J. Horne 1980. An analysis of ice profiles obtained by submarine sonar in the Beaufort Sea. *Journal of Glaciology*, 25, 401-424.
- Wadhams, P. and C.B. Sear 1991. Upper and lower surfaces of Arctic sea ice compared by the use of sidescan sonar and synthetic aperture radar. (In preparation).

11 APPENDICES

11.1 Appendix I. The Autocorrelation Function and Power Spectrum
of the Underside of Arctic Sea Ice

11.2 Appendix II. Submitted Paper:

Statistical properties of Arctic sea ice morphology
derived from sidescan sonar images

11.3 Appendix III. Draft Paper:

Upper and lower surfaces of Arctic sea ice compared by
use of sidescan sonar and synthetic aperture radar

**THE AUTOCORRELATION FUNCTION AND POWER SPECTRUM
OF THE UNDERSIDE OF ARCTIC SEA ICE**

**A REPORT UNDER
PHASE III CONTINUATION
Continuing Data Analysis of 1987 Data Sets
in Government Fiscal Year 1990**

Prepared for the following funding agencies:

**Office of Naval Research
Department of the Navy
Arlington VA**

**NASA
Washington DC**

**and
The Office of the Oceanographer
U.S. Navy Observatory
Washington DC**

**Contract No. N00014-89-C-0014
SAIC Project No. 1-494-03-380**

**Science Applications International Corporation
Polar Oceans Associates
Westbrook Centre, Milton Road
Cambridge CB4 1YQ**

27 March 1990

THE AUTOCORRELATION FUNCTION AND POWER SPECTRUM OF THE UNDERSIDE OF ARCTIC SEA ICE

ABSTRACT

Using data from the 1987 British Arctic submarine cruise, autocorrelation and spectral analysis techniques are used to investigate the nature of the roughness of the underside of Arctic sea ice and its geographical variation.

1 THE PHYSICAL BASIS

1.1 Introduction

The purpose of undertaking this analysis was to gain insight into the geometrical properties of the underside of Arctic sea ice (in particular spatial correlative properties), in order to ascertain the statistical nature of underside roughness. Applications of this type of analysis are to ice-ocean frictional coupling, internal wave generation by ice, ice forces on structures and acoustic scattering by the underside of the sea ice.

1.2 The autocorrelation function

Let the draught of the ice underside be represented by $y(x)$ where x is horizontal distance. Within a sample space k , the autocorrelation function $R_{yy}(\tau)$ is given by:

$$R_{yy}(\tau) = E[y_k(x)y_k(x+\tau)] \quad (1)$$

where E indicates expected value and τ is a lag.

Only positive values of τ are considered, since it is well known that (Bendat and Piersol, 1986) for a second order stationary random process, with a constant mean and variance:

$$R_{yy}(\tau) = R_{yy}(-\tau) \quad (2)$$

Considering only the normalised autocorrelation function:

$$\bar{R}_{yy}(\tau) = R_{yy}(\tau) / (R_{yy}(0)) \quad (3)$$

In the case of a dataset of finite length X , we have:

$$\bar{R}_{yy}(\tau) = \left(\frac{1}{X}\right) \int_0^X y(x) y(x+\tau) dx \quad (4)$$

which becomes a sum rather than an integral if the dataset consists of ice draughts at finite spacings, rather than being continuous.

The general shape of $\bar{R}_{yy}(\tau)$ indicates the length scale over which the ice underside shows significant correlation (i.e. the typical scales over which individual physical features of the ice bottom, such as floes, ridges and leads extend). An informative simple measure of this is the lag at which the autocorrelation function first falls to zero.

Significant periodicity in the autocorrelation function would also be evidence of similar periodicity in ice bottom features. For example, a preferred spacing for ridges or leads.

A third and very important property of the autocorrelation function is that at small lags it can yield insight into the roughness of the ice surface, defined in terms of its fractal dimension. Consider a surface where, for very small increments in x , the draught y varies as τ^α , thus:

$$|y(x+\tau) - y(x)| \sim \tau^\alpha, \tau \rightarrow 0 \quad (5)$$

Such a surface is said to obey the Lipschitz condition (Rothrock and Thorndike, 1980) and α is the Lipschitz exponent. Only if $\alpha=1$ is y differentiable. When $\alpha=0$, the derivative of y is infinite. Thus, the range $0 < \alpha < 1$ defines a range of continuous but undifferentiable functions, with α being a measure of the 'roughness' of the surface.

Here it is assumed that these relationships hold for ice draught, since there is no reason to doubt that they do (Rothrock and Thorndike, 1980).

For such a surface, it can be shown using (1) that, for small lags:

$$R(\tau) \sim R(0) - c\tau^{2\alpha} \quad (6)$$

Thus, by examining the variation of $R(\tau)$ near zero lag, it is possible to test whether sea ice obeys the Lipschitz condition and if so, what is its Lipschitz exponent. Normalising (6), we find that:

$$\ln(1-\bar{R}(\tau)) = -2\alpha \ln \tau + c' \quad (7)$$

where c' is a constant.

Thus, a log-log plot of $(1-\bar{R}(\tau))$ against τ gives a measure of α .

If the ice underside is rough function (i.e. continuous but undifferentiable), the amount of detail displayed by any representation of it will increase as the interval between successive horizontal increments decreases, assuming a perfect measurement technique (i.e. zero beamwidth). Such a profile is not a simple line, but rather a fractal (Mandelbrot, 1977). Mandelbrot showed that a set of points in a plane can be assigned a dimension, the so-called Hausdorff or fractal dimension D , depending on the extent to which the set of points resembles an area (Dimension 2) or a smooth line (Dimension 1). A rough ice profile will have a dimension between 1 and 2, with the actual value being a measure of its 'roughness'. Mandelbrot showed that the Hausdorff dimension is related to the Lipschitz exponent by:

$$D = 2 - \alpha \quad (8)$$

Thus, it may be possible to measure the roughness of the underside of sea ice by using the draught data collected by Upward-looking Sonar.

1.3 The Power spectrum

The power spectral density function is defined as the Fourier transform of the autocorrelation function. Thus:

$$S(k) = R_{yy}(\tau) e^{-i2\pi k\tau} \quad (9)$$

where $k = 1/\lambda$ (the wave number). It expresses the variance (energy density) present in the underice profile at a wave number k , per unit increment in k .

Mandelbrot (1977) showed that if a function obeys the Lipschitz condition, then in most cases the power spectral density varies as k^p , where:

$$p = -2\alpha - 1 \quad (10)$$

Thus, if $p < -3$ the profile is smooth (differentiable), while if $-1 < p < -3$ the profile is rough. If $p = -1$ the power spectrum is not integrable and the surface has infinite variance (that is, it can be described as 'fully rough'). In the special case of $p = -3$ there is no natural length scale to the surface. It would then look the same when viewed under any degree of magnification. A number of natural surfaces have spectra which lie close to this state (Jæger and Schuring, 1966; Nye, 1973).

2. DATA AND ANALYSIS METHODS

The dataset used comprised corrected ice draught data from a 1987 submarine cruise, extending from the North Pole into Fram Strait. The data were collected on 19th, 20th and 21st May, 1987 using an Upward-looking Sonar operating at 48kHz, with a quoted beamwidth of less than 5°. The data were recorded digitally and on paper chart.

Extensive data reduction was necessary to generate a clean and corrected dataset for this analysis. The digital data points were recorded at uniform time intervals (of about 0.25s) and these had to be converted to distance intervals using boat speed values calculated from navigational fixes on the ship's inertial navigational system (SINS). In doing this, account was taken of rates of acceleration and deceleration during the frequent speed alterations which

the boat carried out. The along track data points were then corrected to a uniform interval of 1m using a square-law interpolation routine. Next, the data (hitherto expressed as a range to the reflecting underside) were converted to draught data making use of a manual analysis of the chart records, insertion of sea level values wherever observed, generation of a smoothed curve through these values and subtraction.

The corrected dataset was then divided into 35 sections (Sections 1 to 35), each 50km long, from north of Greenland to Fram Strait. The analysis for autocorrelation function and power spectral density was carried out over successive 2km subsections within each section, with ensemble averaging to improve the statistical reliability. Each 2km subsection had to be complete, with no gaps, for the spatial analysis to be valid. It was decided that sections containing fewer than five such complete subsections would not give reliable statistics and these were ignored. Seven sections were rejected (Sections 4 to 6 and 17 to 20), leaving 38 remaining, which were analysed.

Geographically, the sections concerned can be divided into three groups. Group 1 (Sections 1-12) comprises the central Arctic Basin, a line from the North Pole south approximately along 55°W, to 85°N. Group 2 (Sections 13-28) comprises the Greenland Offshore Zone, a transect across the north of Greenland towards Fram Strait. Group 3 (Sections 29-35) comprises Fram Strait south of 81°N, a region with broken-up floes and much open water because of the proximity to the Greenland Sea.

The normalised autocorrelation function was computed using a statistical package (GENSTAT) routine, for lags of up to 1000m. The routine uses the indirect approach of computing the spectral density using FFT (Fast Fourier Transform) techniques, then computing the inverse Fourier transform of the power spectrum. The power spectral density was computed using conventional FFT techniques for wave numbers of up to 0.5m^{-1} (the Nyquist frequency) and plotted on log-log and log-linear scales. Results for each subsection were ensemble averaged to yield results for a whole section, and the random error computed as $1/n^{1/2}$, where n is the number of subsections in a section (Bendat and Piersol, 1986). No attempt was made to estimate bias error.

3 RESULTS

The results of the analysis are shown as Figures 1 to 35 (for simplicity, each section defines the figure number, so there are no Figures 4, 5, 6, 17, 18, 19 or 20). On each figure, the heading '2.N' refers to ensemble averaged results for Section N. The standard error in the power spectral density is shown in each case.

4 INTERPRETATION

4.1 Autocorrelation function

The general appearance of the autocorrelation functions (Figures 1 to 35) is straightforward. There is some evidence of oscillations but only in Section 34 are clear secondary peaks observed. This was the most easterly section of the profile, encompassing the ice edge and including a great deal of open water. It is possible that a systematic preferred spacing of leads is occurring (perhaps because of the presence of ice edge bands, which frequently have regular spacings, Wadhams, 1983).

The lag at which the autocorrelation function first reaches zero is shown in Table 1, which also shows the Lipschitz exponent. Preliminary tests of the fit of data to Equation 7 showed that a typical plot of $\ln(1 - R)$ against $\ln r$ has a slowly increasing slope for lags of up to 8m, then a relatively constant slope for lags up to about 20m, then a decreasing slope. The relationship is meant to be used at small lags to compute α .

However, it is likely that at the smallest lags, the autocovariance is artificially increased by the fact that the sonar had a beamwidth of about 5° (giving a surface beam diameter of about 8m) and so gives a smoothed profile. Therefore, the range of lags from 8m to 20m was used to obtain a best value for each section, by linear regression.

If averages are taken over each geographical group of sections (as described above), then Group 1 has a zero-crossing range of 267m and an exponent of 0.510. Group 2 has 263m and 0.547 and Group 3 has 337m and 0.454. These are not large differences but indicate the following:

Section	Lag (m) at which R crosses zero	Lipschitz exponent	Hausdorff dimension
1	271	0.560	1.440
2	389	0.520	1.480
3	362	0.448	1.552
7	195	0.527	1.473
8	271	0.513	1.487
9	317	0.409	1.591
10	146	0.518	1.482
11	331	0.557	1.443
12	120	0.540	1.460
13	202	0.537	1.463
14	313	0.535	1.465
15	390	0.403	1.597
16	265	0.669	1.331
20	448	0.667	1.333
21	227	0.710	1.290
22	175	0.711	1.289
23	248	0.510	1.490
24	180	0.438	1.562
25	204	0.341	1.659
26	248	0.526	1.474
27	298	0.556	1.444
28	215	0.514	1.486
29	226	0.516	1.484
30	407	0.518	1.482
31	388	0.444	1.556
32	357	0.426	1.574
33	318	0.472	1.528
34	290	0.456	1.544
35	371	0.348	1.652

Table 1. Properties of autocorrelation functions

- i. A slightly longer coherence length for ice features in Fram Strait than in the Arctic Basin, possibly a consequence of the dominance of the profile by floes and wide leads rather than by pressure ridges.
- ii. A relatively small Lipschitz component in Fram Strait and a relatively larger one in the Greenland Offshore Zone. This implies that fractal roughness as defined by the Hausdorff dimension is highest in Fram Strait and lowest in the Greenland Offshore Zone where the physical roughness (for example, mean ice draught and frequency of ridges) is greatest. This is an interesting paradox.

Within each group there are wide variations, however and the trends noted above may not be significant. However, it is interesting to compare the results with those obtained from a cruise by another British submarine to the Fram Strait and Arctic Basin in the summer of 1985 (Calvert, 1988, pers. comm.). Then, Lipschitz exponents lay in the range 0.5 to 0.8, suggesting a lower fractal roughness in summer which may result from smoothing of the ice surface by melting.

4.2 Power spectrum

It can be seen that the power spectral densities when plotted on a log-log scale show three distinct slope domains:

- i. At low wave numbers (very long wavelengths of 300m or more), the decay of the spectrum with increasing wave number is slow (p in Equation 10 is of the order of -1). This corresponds to wavelengths where the autocorrelation function shows little or no coherence.
- ii. At moderate wave numbers (corresponding to wavelengths of between about 300m and 10m), the spectrum falls off as a power law, with p values which are discussed further below.
- iii. At high wave numbers (corresponding to wavelengths of less than 10m), there is a 'knee' in the spectrum followed by a more rapid fall off in energy density with increasing k .

It has already been shown that the autocorrelation function has anomalous properties at lags of 8m or less and that 8m is approximately the surface beam diameter of the sonar. Thus, it is likely that the smoothing of the underice profile caused by sonar beamwidth is producing an anomalously rapid fall off in energy at wave numbers corresponding to wavelengths of less than the surface beam diameter.

Thus, this part of the spectrum can be regarded as an artefact of the sonar system and further investigation of its properties lies beyond the scope of this report.

The region of moderate wave numbers (ii. above) was studied further by measuring the slope of the linear part of the log-log spectrum and defining the range of wave numbers over which this linearity occurred. Results are given in Table 2.

In Table 2, three of the sections (22, 27, 29) have two gradients, since the spectrum changed slope within the range of moderate wave numbers. On the whole, however, there is remarkable consistency. The log-log plots show a straight line from about 10m wavelength (corresponding to the beginning of beamwidth-induced smoothing) to a wave number corresponding to about 200m wavelength. The exponents show some very low values, especially in the Fram Strait sections, but mostly these also within a limited range.

Taking simple arithmetical means, by geographical region, as before, the following results are obtained. The central Arctic Basin (Sections 1-12) has a mean exponent of -2.21 over a range of validity from 14m to 213m wavelength.

The Greenland Offshore Zone has a mean exponent of -2.19 from 15m to 146m if the first quoted slopes in Table 2 for Sections 22 and 27 are used (but -2.33 from 18m to 165m if the second set of slopes are used). The Fram Strait zone has a mean exponent of -1.91 from 12m to 163m using the first slope in section 29 but -1.99 from 16m to 179m using the second slope.

It is clear that the Arctic Basin and Greenland Offshore Zone have similar p values (valid over a somewhat more restricted range of wavelengths for the Greenland Offshore Zone), whilst the Fram Strait data suggest a lower p value. Translating these into Lipschitz exponents using Equation 10, values are obtained of 0.61 for the

Section	P	Range of validity (m)	
		From	To
1	-2.32	10	158
2	-2.09	10	229
3	-2.15	10	316
7	-2.07	10	178
8	-2.21	10	115
9	-2.36	40	347
10	-2.27	16	158
11	-2.17	10	219
12	-2.25	9	200
13	-2.25	10	58
14	-2.57	25	316
15	-1.58	13	275
16	-2.78	10	115
20	-2.75	20	91
21	-2.66	11	158
22	-2.06 / -3.24	10 / 29	29 / 95
23	-2.00	10	182
24	-1.91	10	219
25	-1.86	10	69
26	-2.44	10	69
27	-1.70 / -2.36	10 / 40	40 / 219
28	-1.94	10	275
29	-1.69 / -2.27	9 / 36	36 / 145
30	-2.19	20	182
31	-1.76	16	457
32	-2.17	11	50
33	-1.51	10	87
34	-2.39	10	76
35	-1.66	10	251

Table 2. Exponents governing wave number spectrum and their ranges of validity

central Arctic, 0.60 to 0.67 for the Greenland Offshore Zone and 0.46 to 0.50 for Fram Strait. These values agree reasonably well with Lipschitz exponents estimated in a completely different way from the autocorrelation functions.

5 CONCLUSIONS

Our general conclusions are:

- i. The underside of Arctic sea ice is a rough surface which obeys the Lipschitz condition, with exponents in the range 0.5 to 0.8.
- ii. The autocorrelation function at small lags (8m to 20m) has a uniform slope from which the Lipschitz exponent and Hausdorff dimension may be calculated. At very small lags the autocorrelation function is affected by the finite beamwidth of the echo sounder.
- iii. The power spectral density of the ice surface $[S(k)]$ varies as k^p , where p takes average values between -1.9 and -2.2 at wavelengths between 10m and about 200m. Using Mandelbrot's relation (Equation 10), the Lipschitz exponent can be derived from the p value and agrees quite well with exponents estimated from the shape of the autocorrelation function.
- iv. At wavelengths below 10m the power spectrum falls off more rapidly, which again is a product of the smoothing effect of sonar beamwidth upon the ice profile.
- v. The fractal 'roughness' is greatest in the Fram Strait region and is fairly consistent over the rest of the Arctic Basin region sampled. This is despite the fact that the physical roughness (expressed in terms of mean and r.m.s. ice draught) is lowest in the Fram Strait region.

6 ACKNOWLEDGEMENTS

This report was drafted by Dr P Wadhams and edited by Dr C Sear. It is issued by SAIC Cambridge. Dr Wadhams undertook the analysis described as a consultant to SAIC. This work follows on from effort undertaken during GFY 1989 and is intended to round off that work.

7 REFERENCES

Bendat J.S. and Piersol A.G. 1986. **Random Data. Analysis and Measurement Procedures** (2nd Ed.). Wiley, New York.

Calvert I.A. 1988. Low lag autocorrelations of the underside of sea ice. **Unpublished Report for Diploma in Mathematical Statistics.** University of Cambridge.

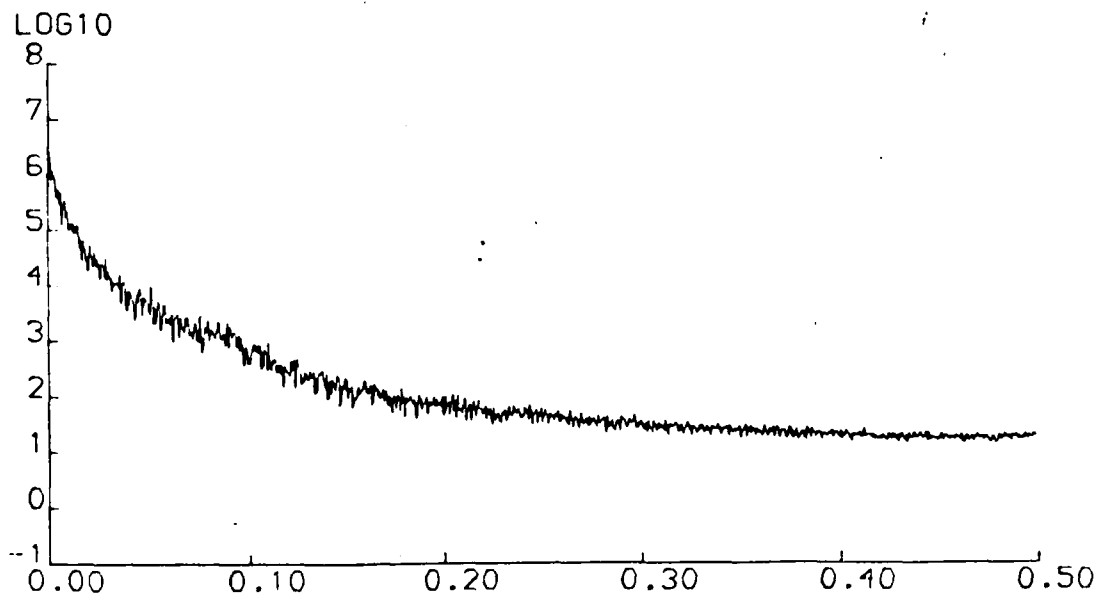
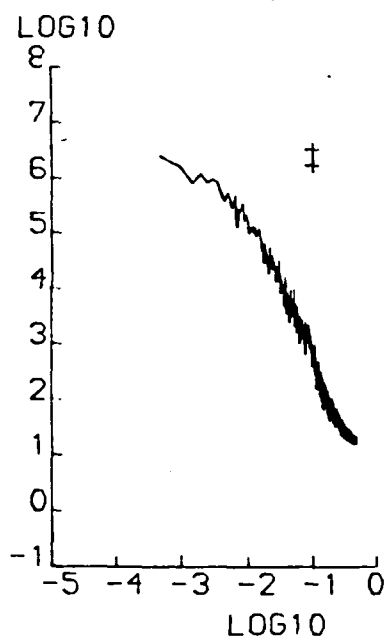
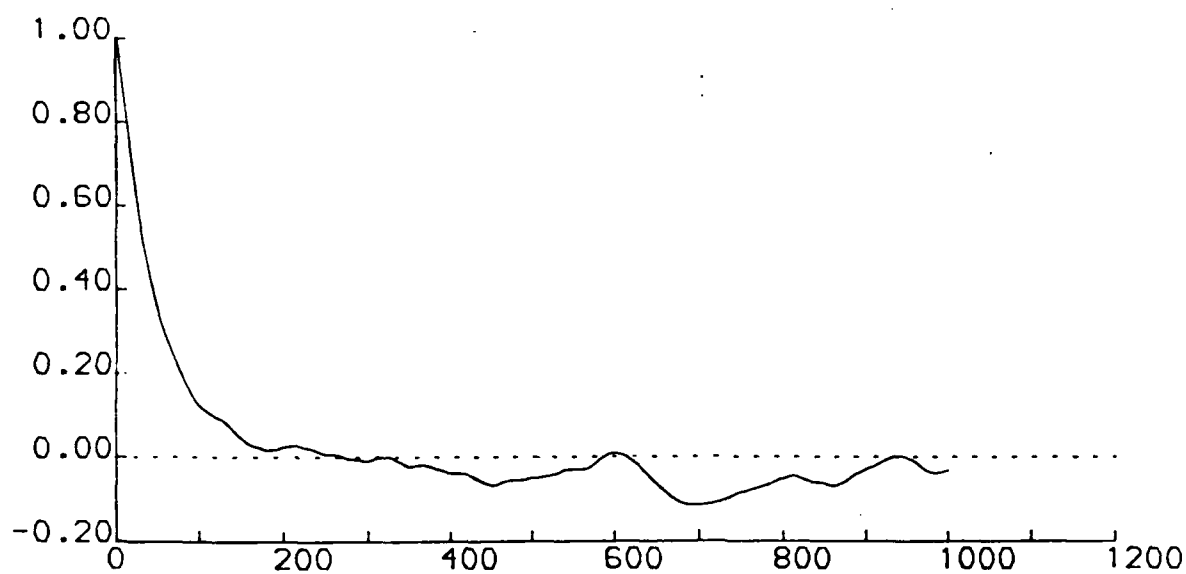
Jäger R.M. and Schuring D.J. 1966. Spectrum analysis of terrain of Mare Cognitum. **J. geophys. Res.**, 77, p5954-5970.

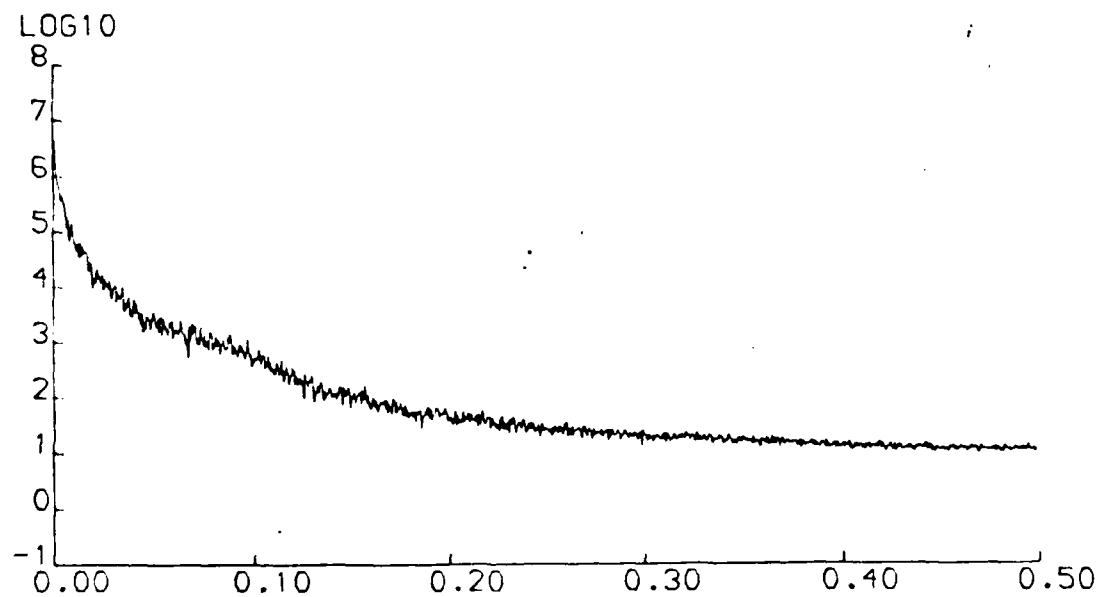
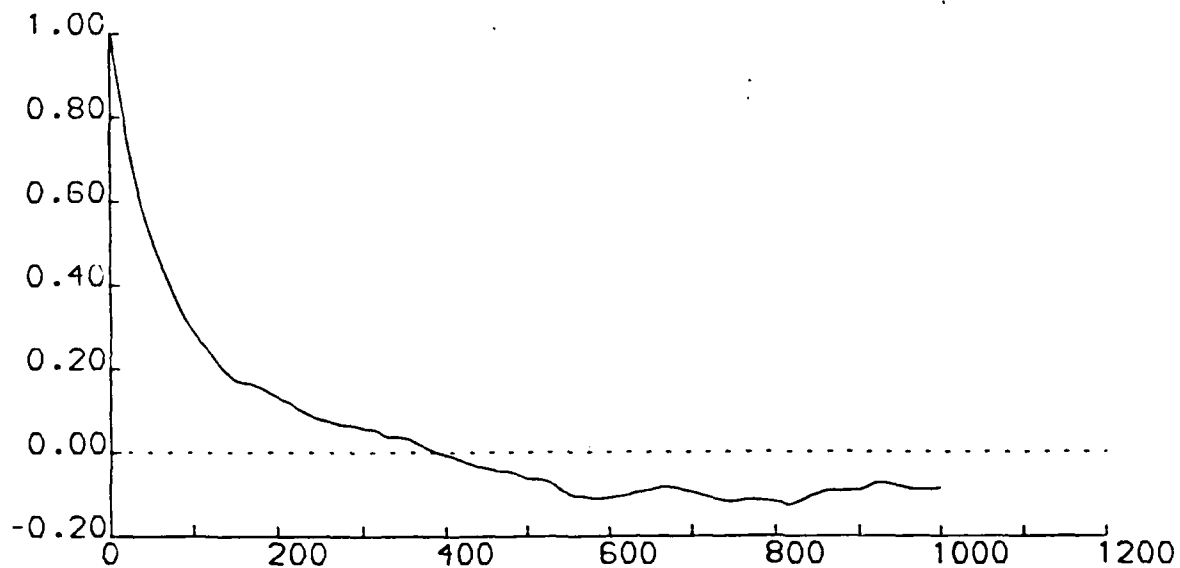
Mandelbrot B.B. 1977. **Fractals. Form, Chance and Dimension.** Freeman, San Francisco.

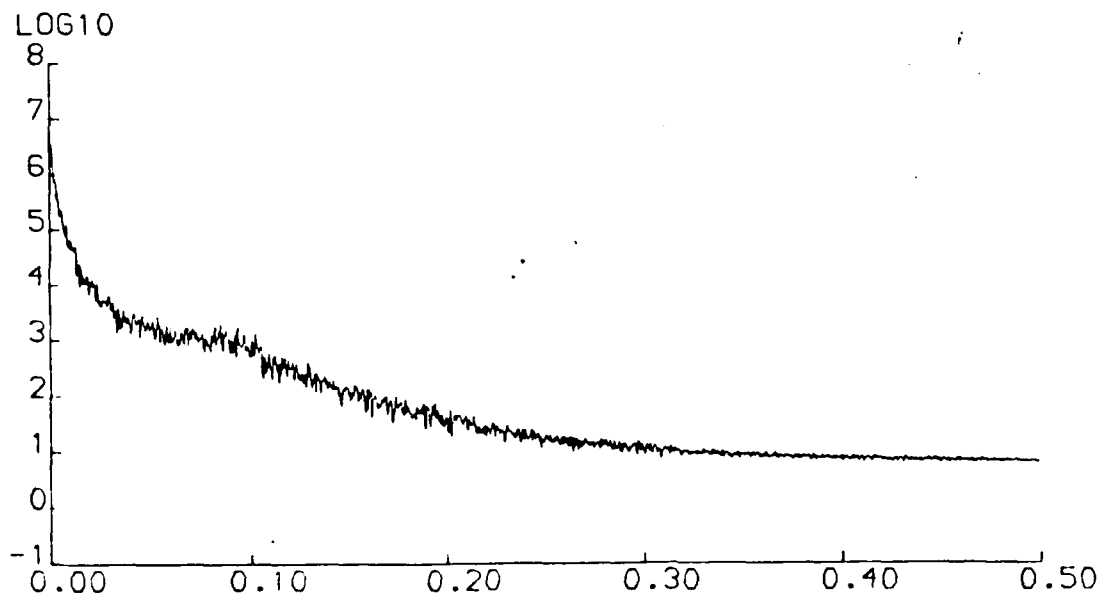
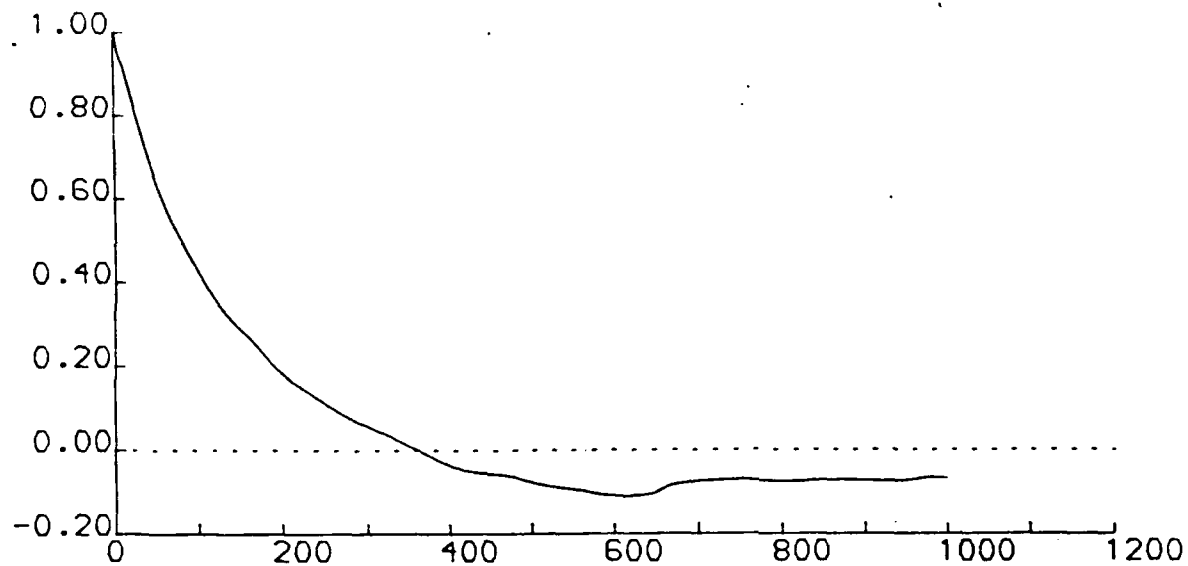
Nye J.F. 1973. A note on the power spectra of sea-ice profiles. **AIDJEX Bull.**, 21, p20-21.

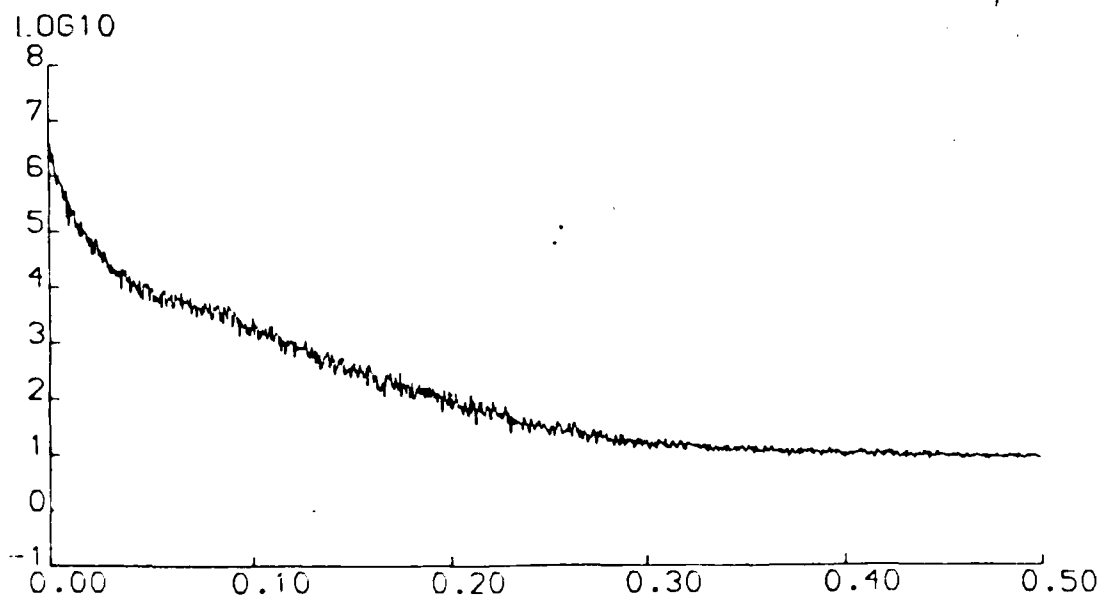
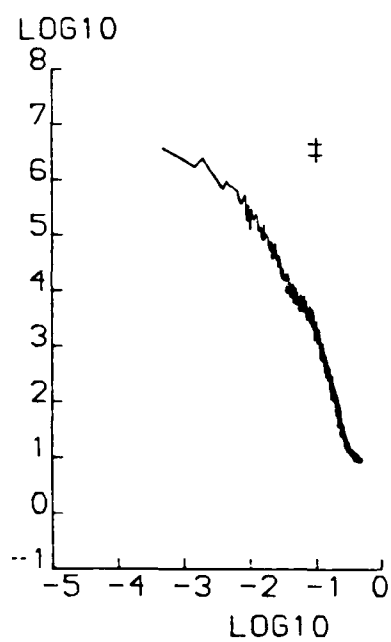
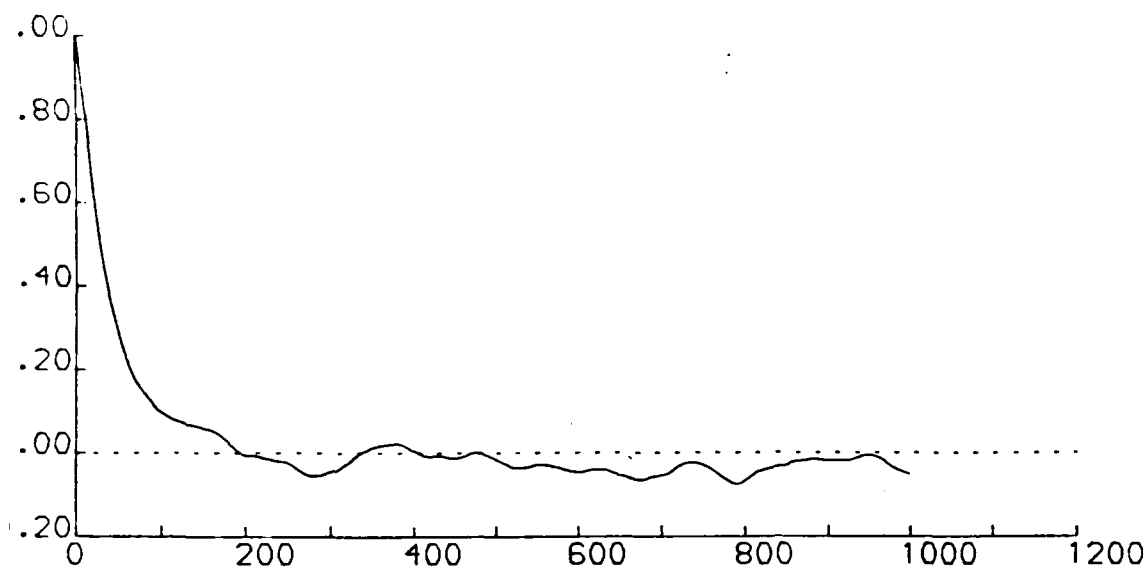
Rothrock D.A. and Thorndike A.S. 1980. Geometric properties of the underside of sea ice. **J. geophys. Res.**, 85, p3955-3963.

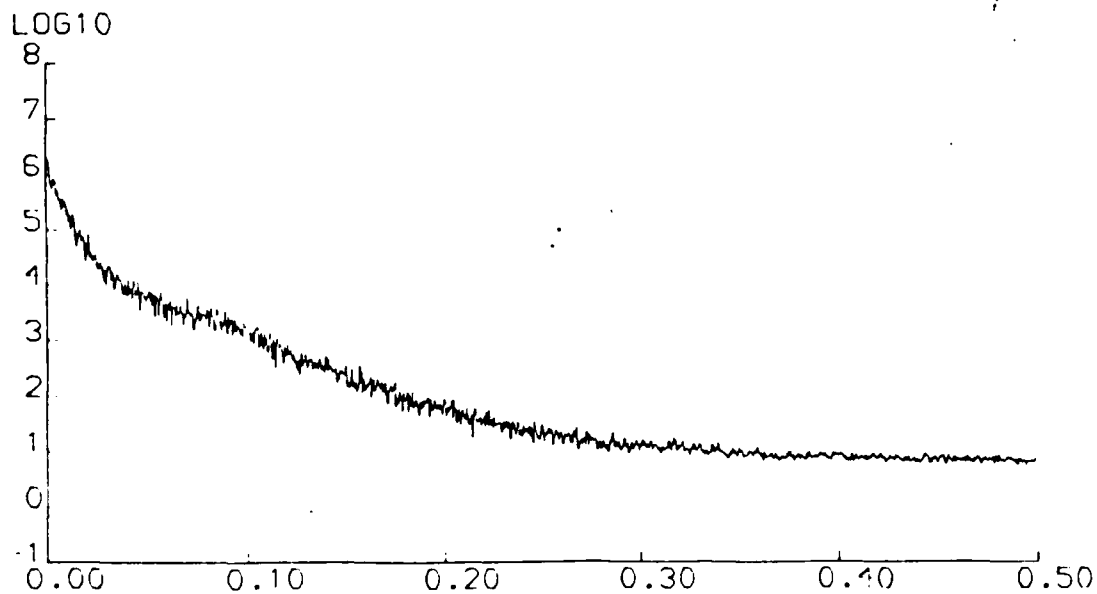
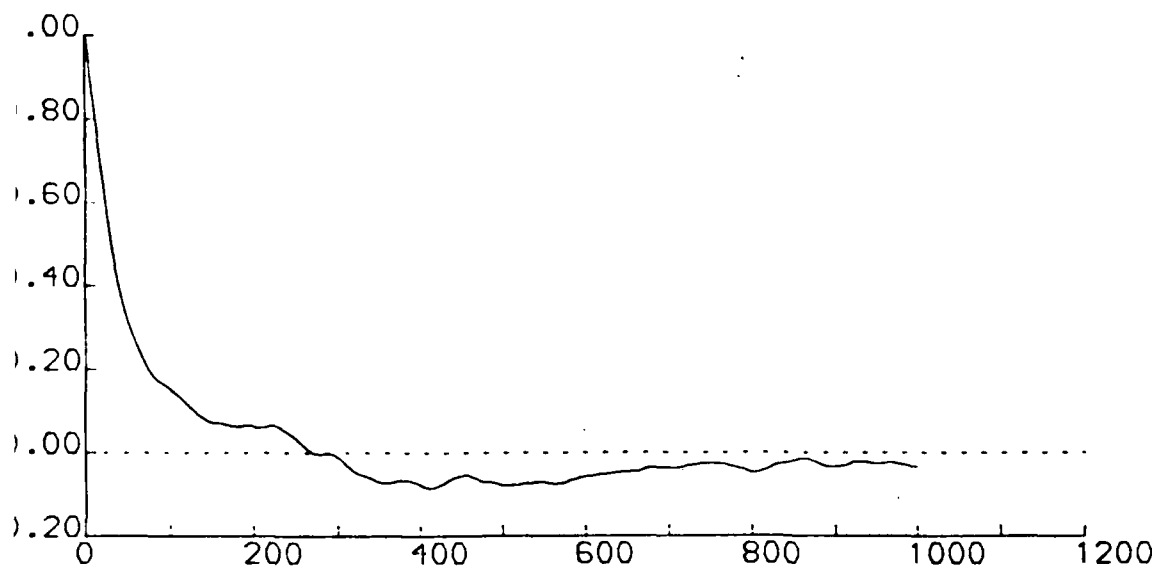
Wadhams P. 1983. A mechanism for the formation of ice edge bands. **J. geophys. Res.**, 88, p2813-2818.

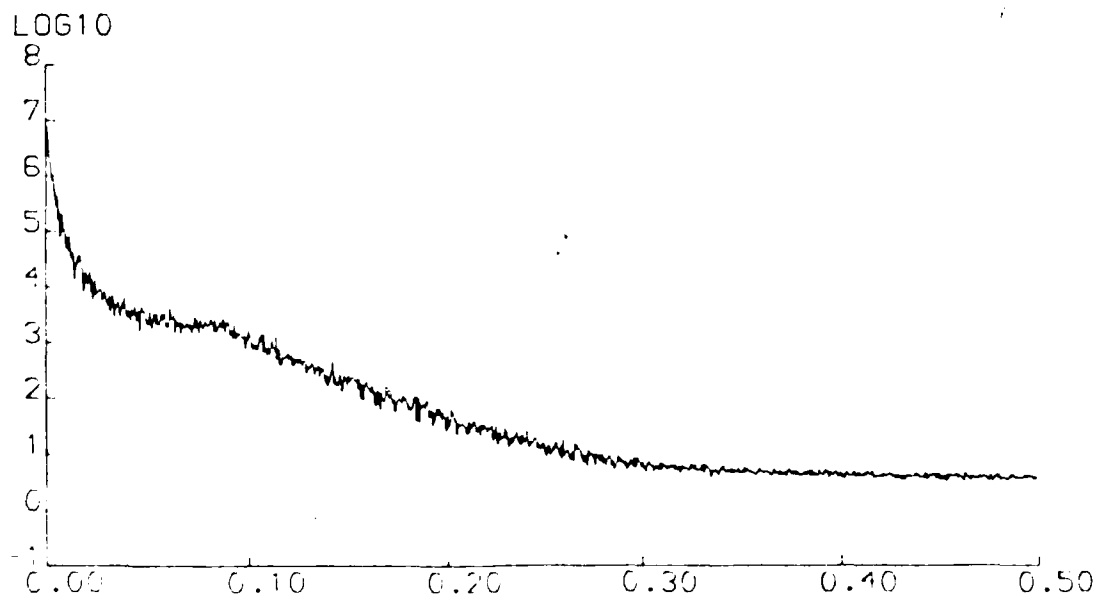
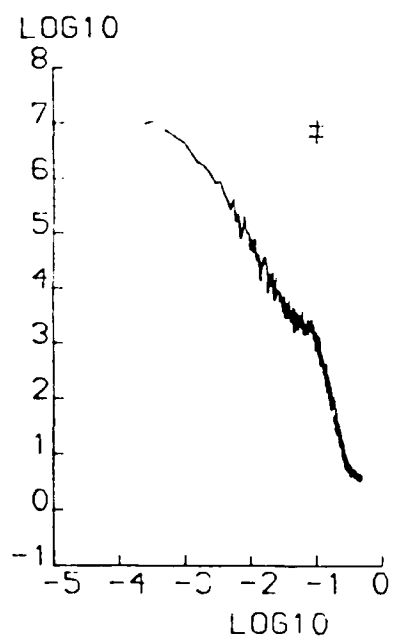
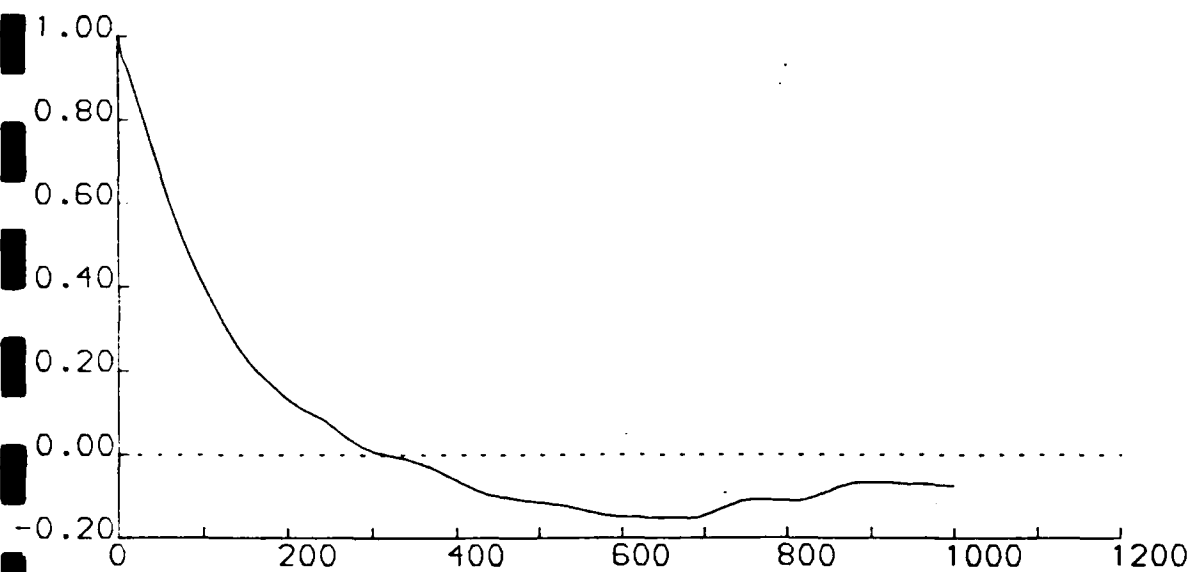


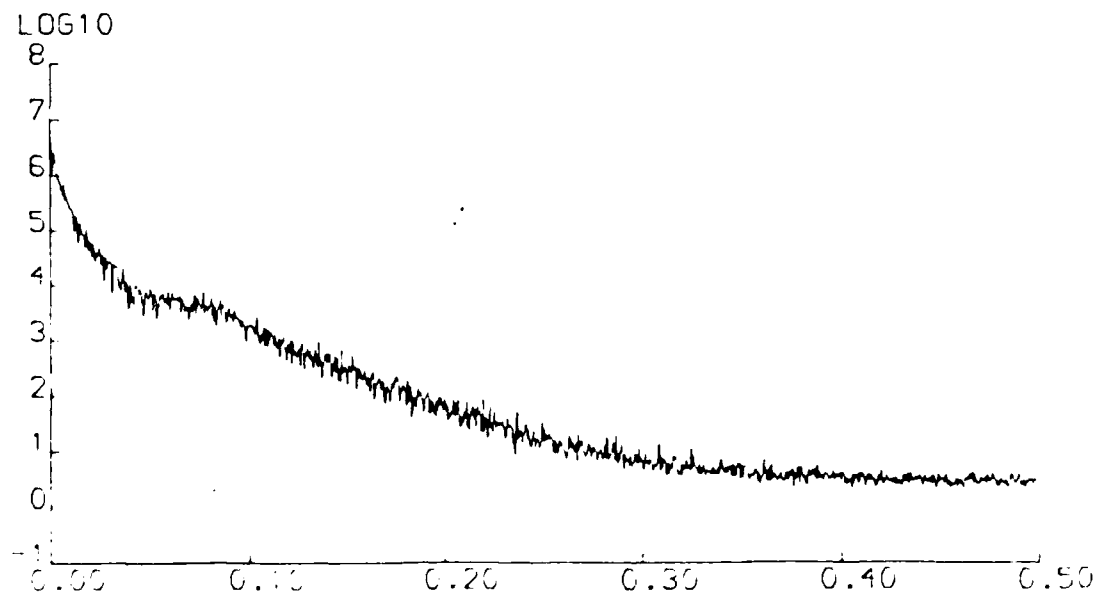
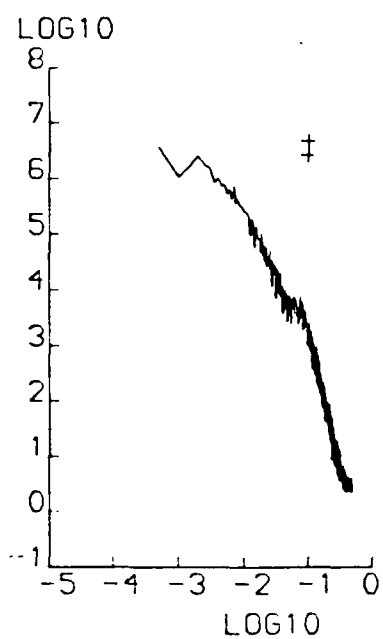
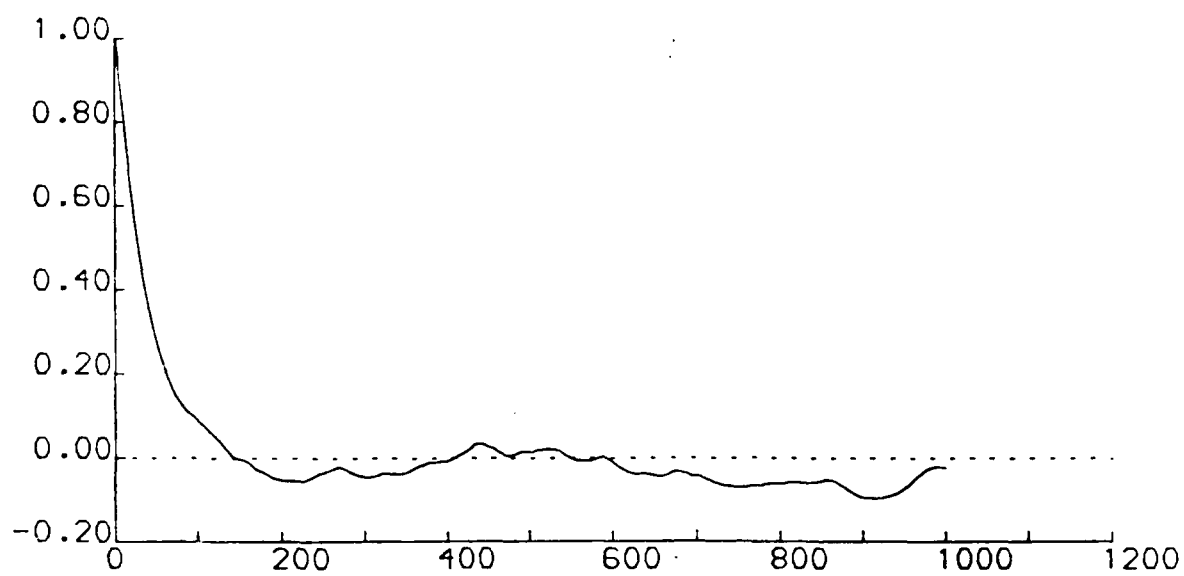


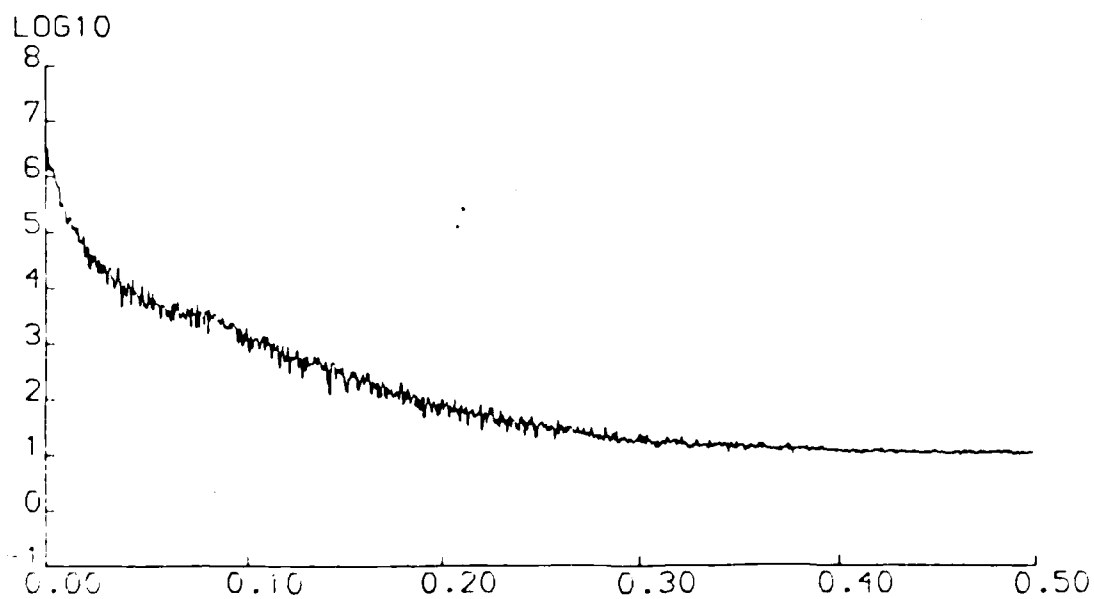
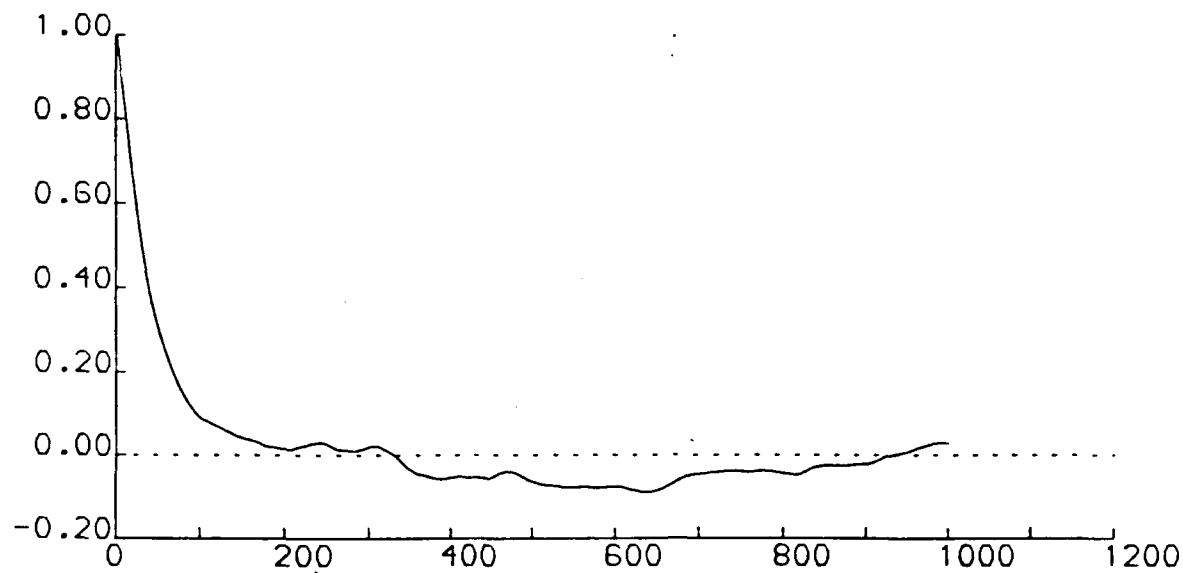


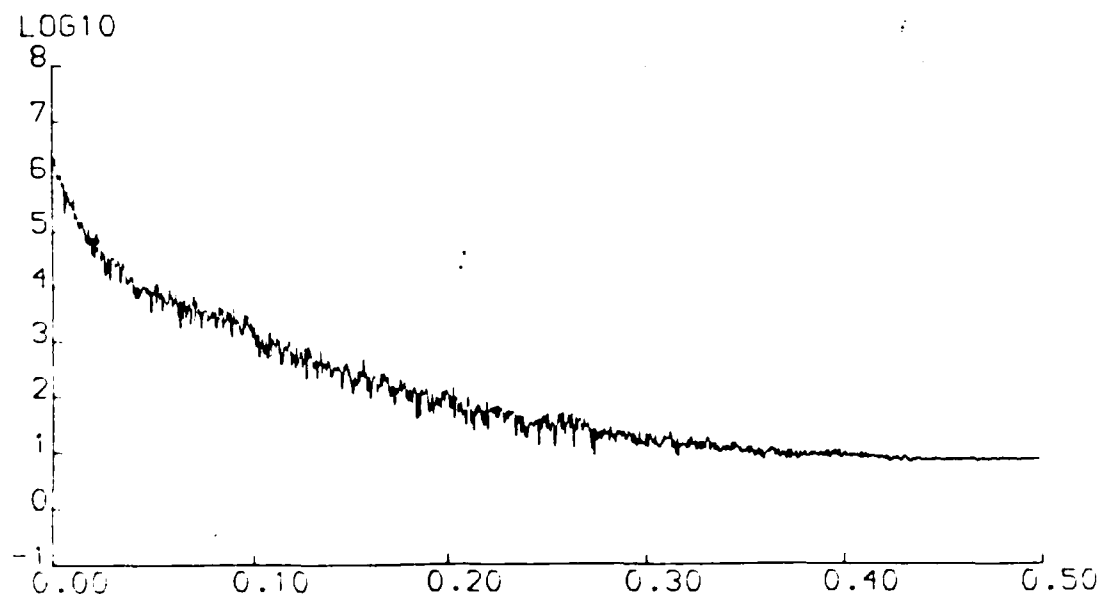
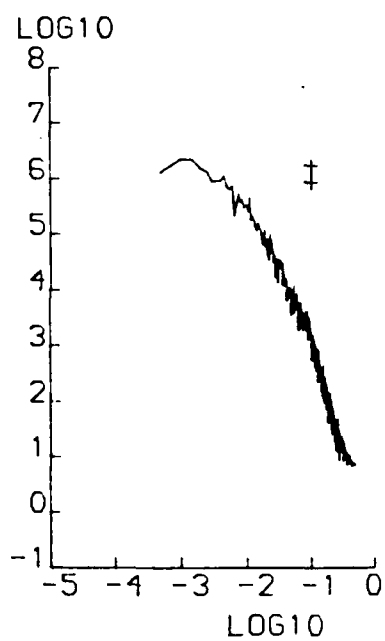
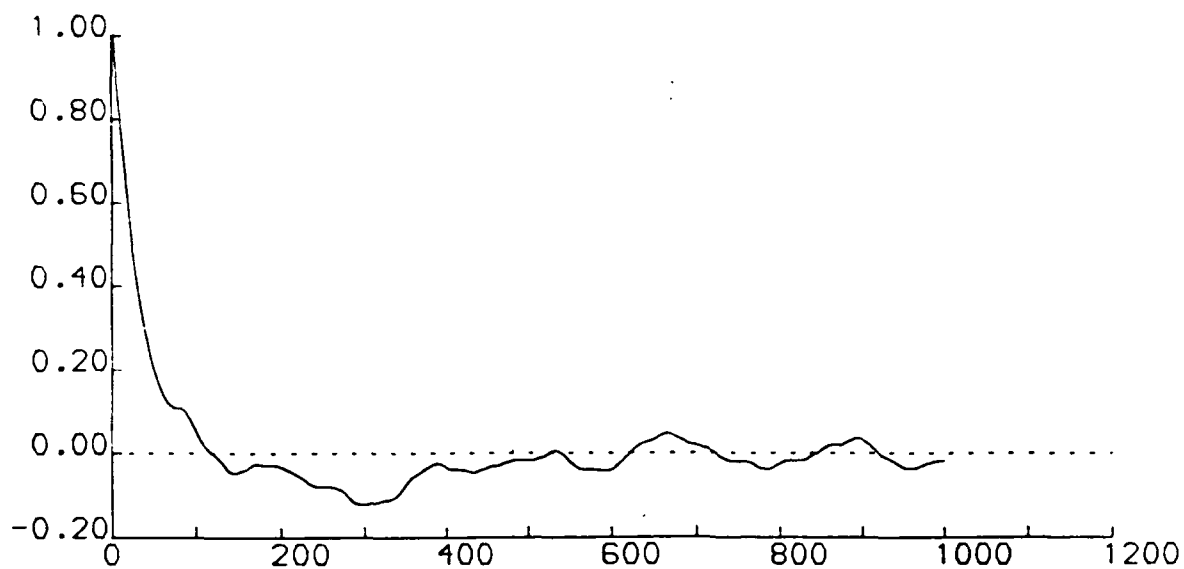


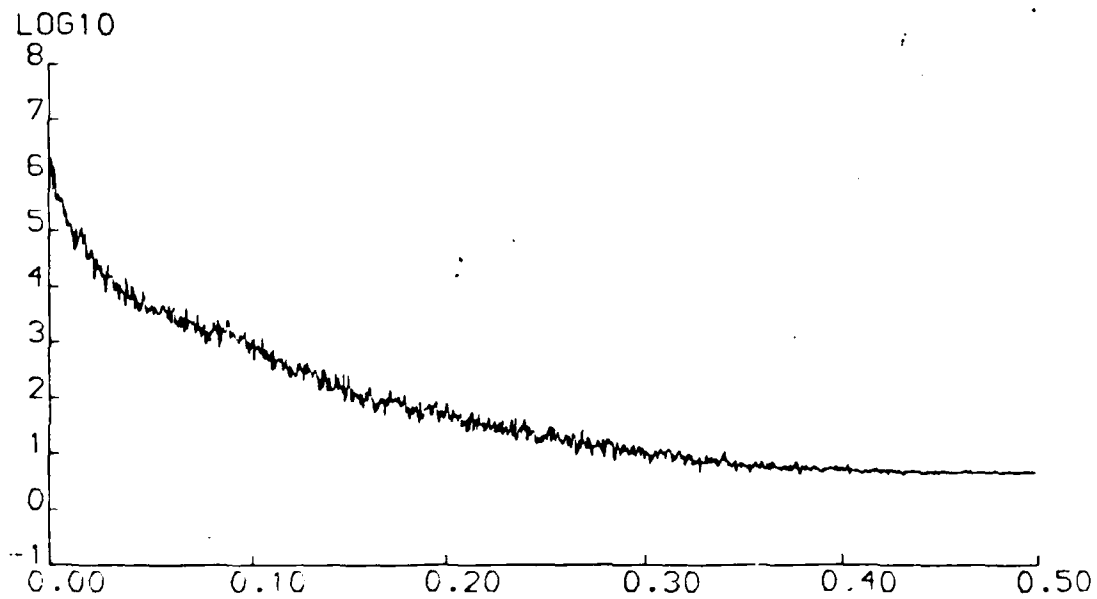
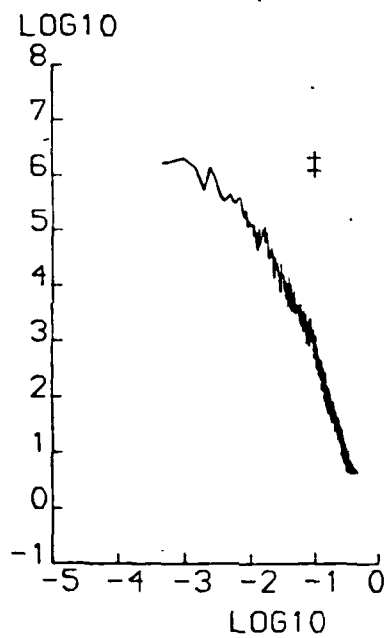
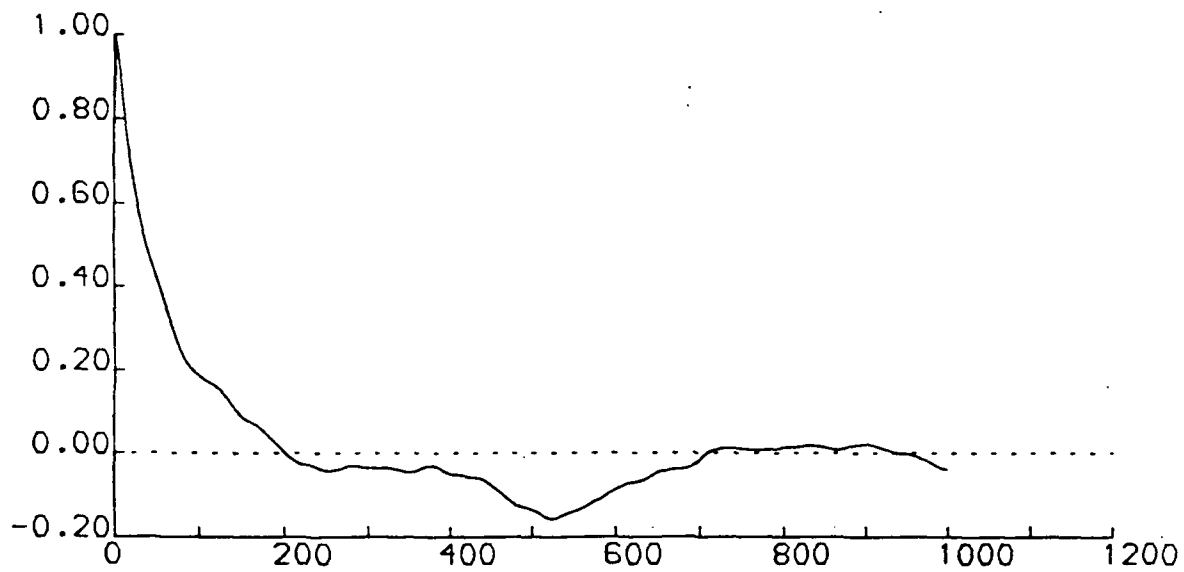


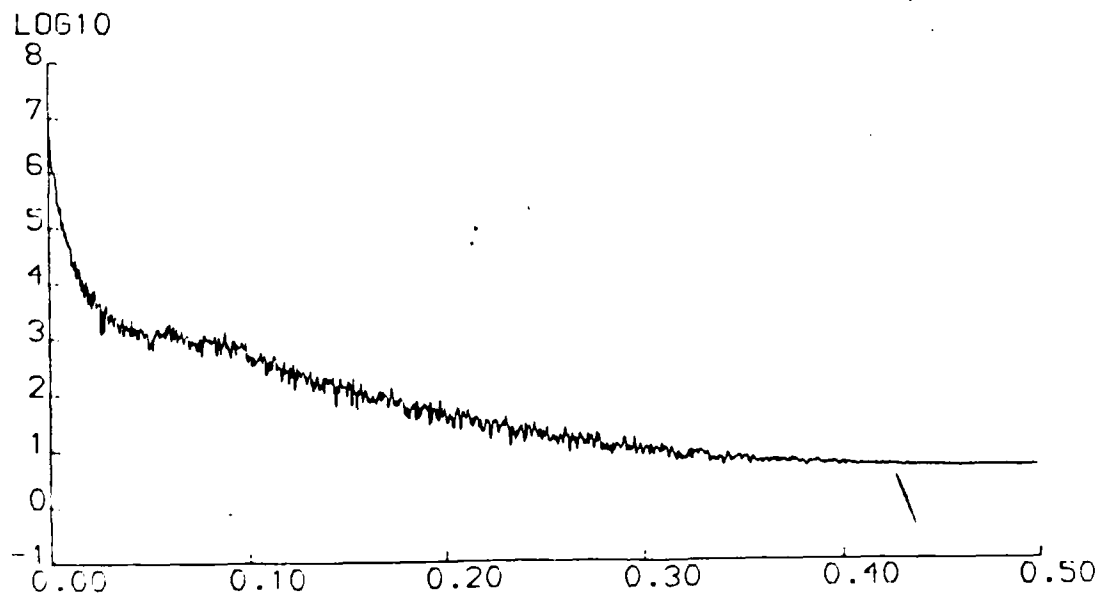
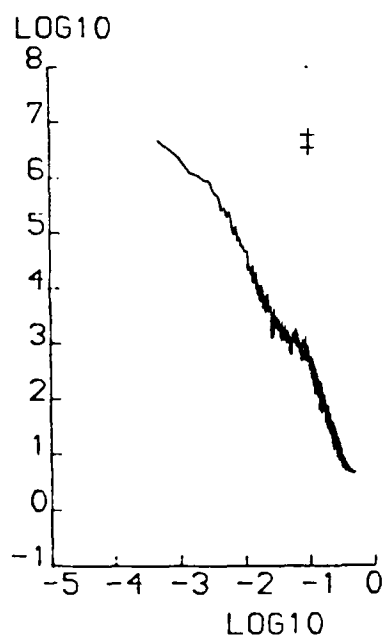
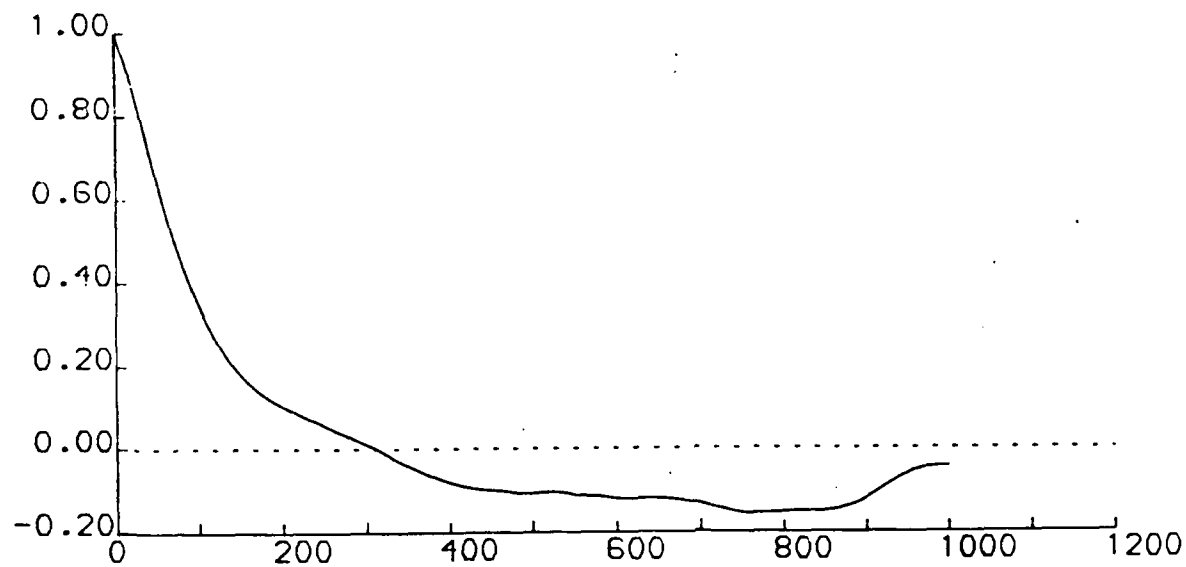


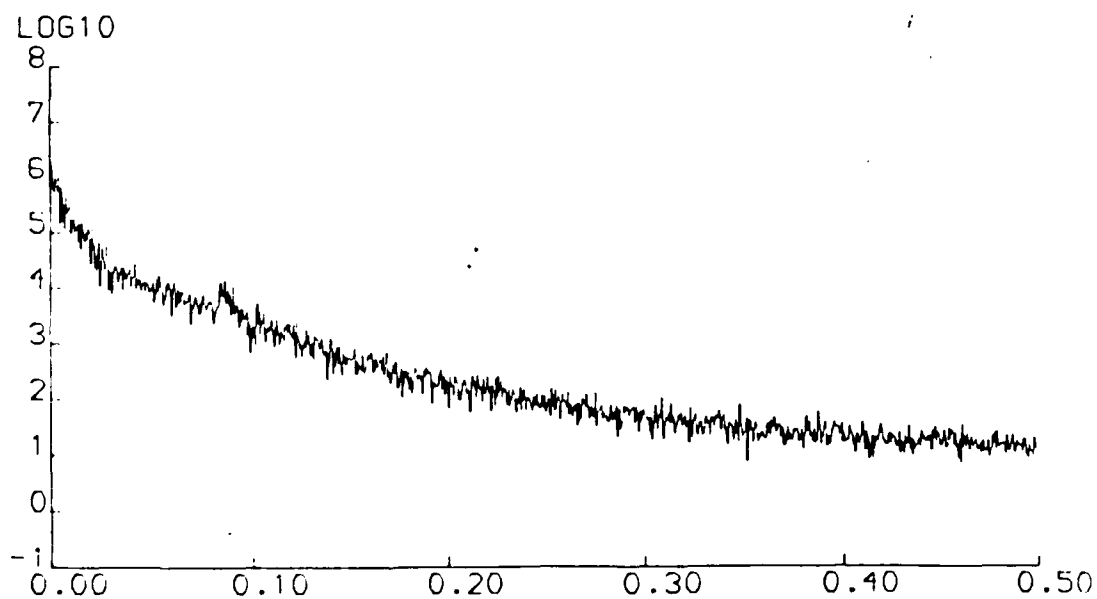
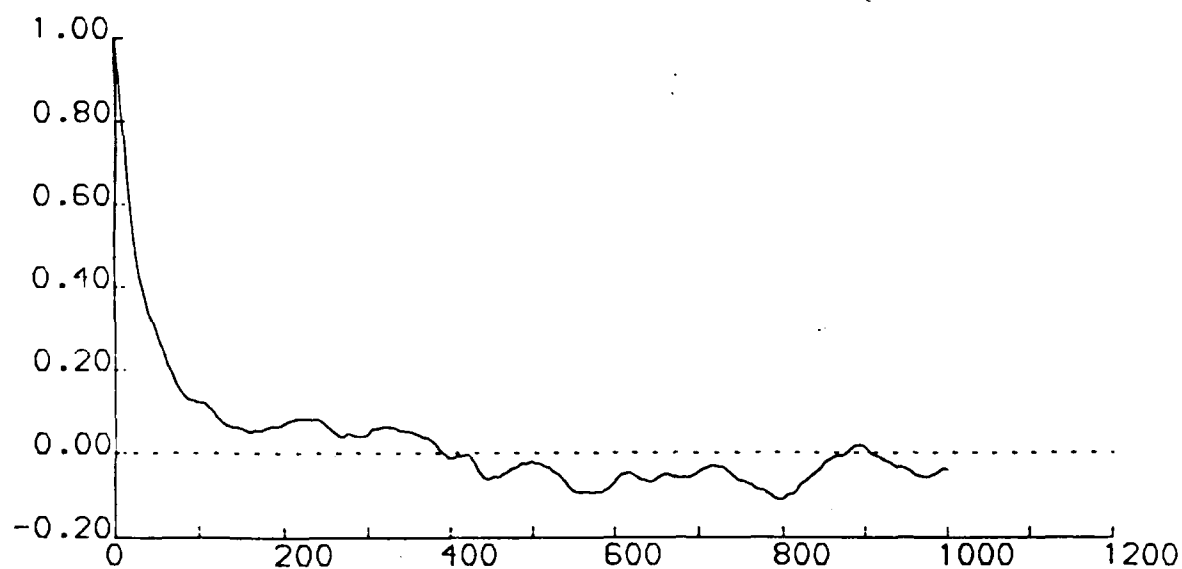


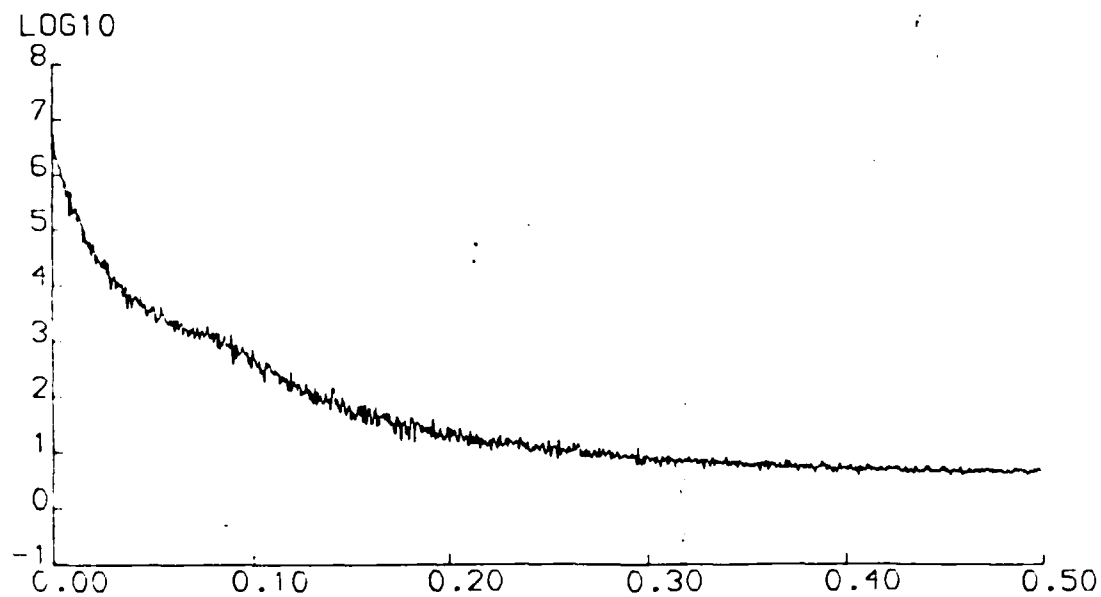
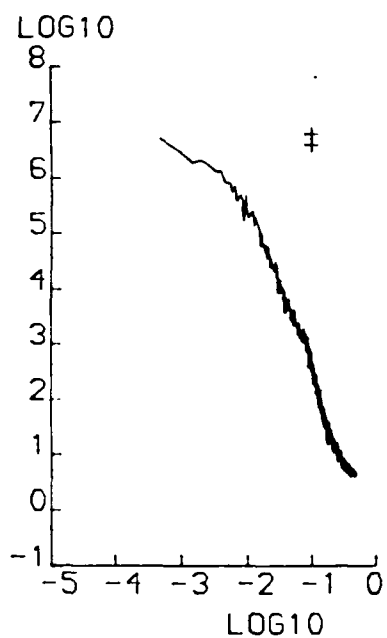
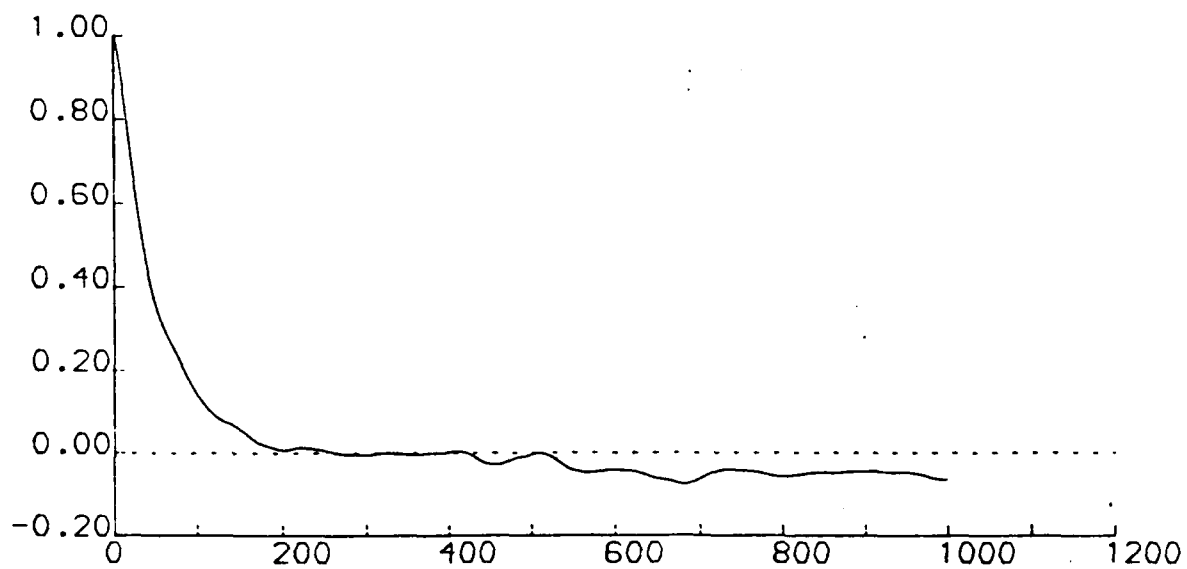


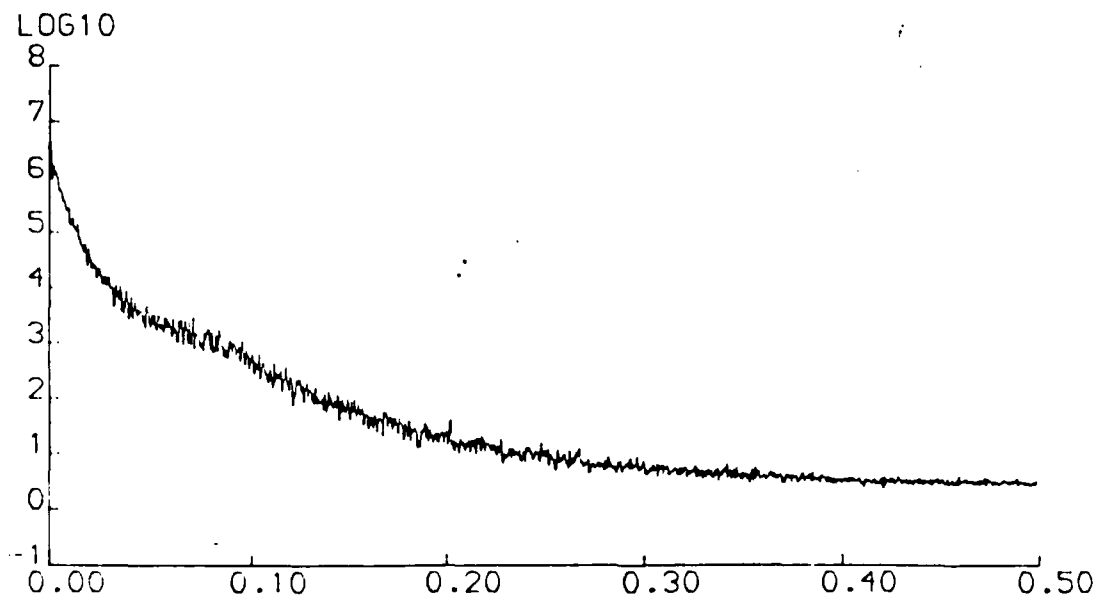
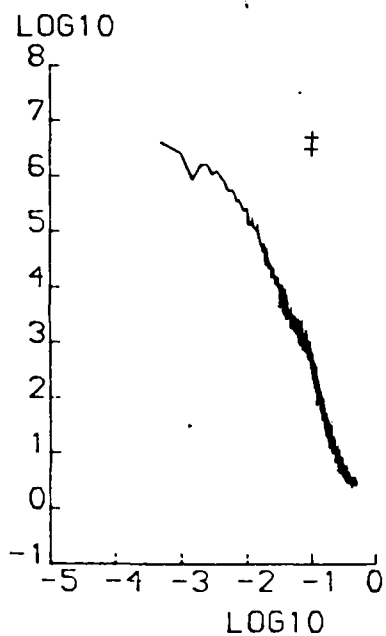
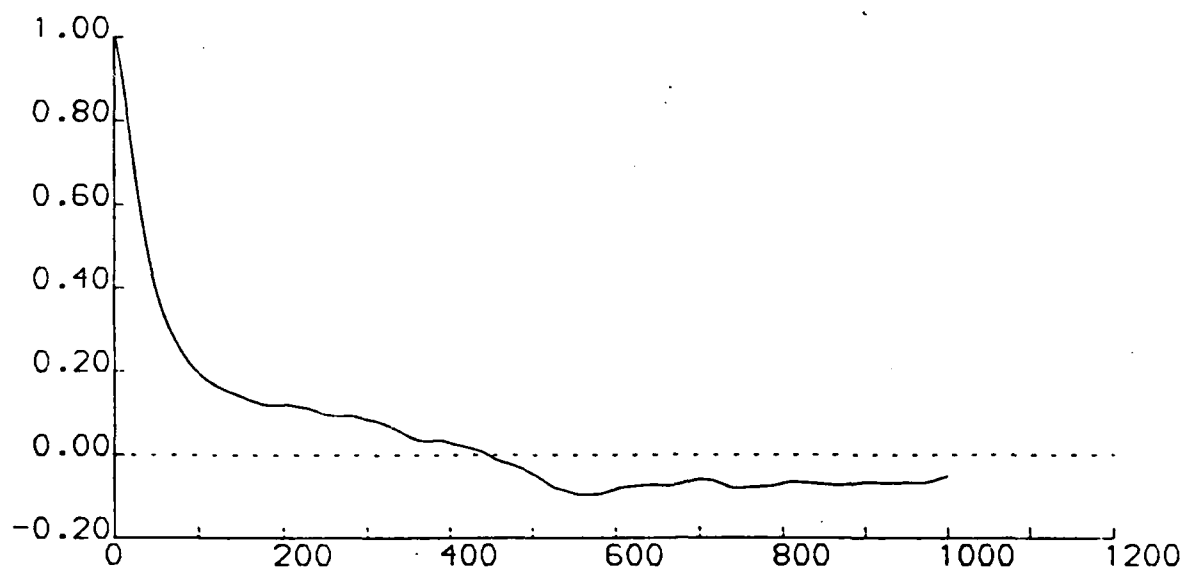


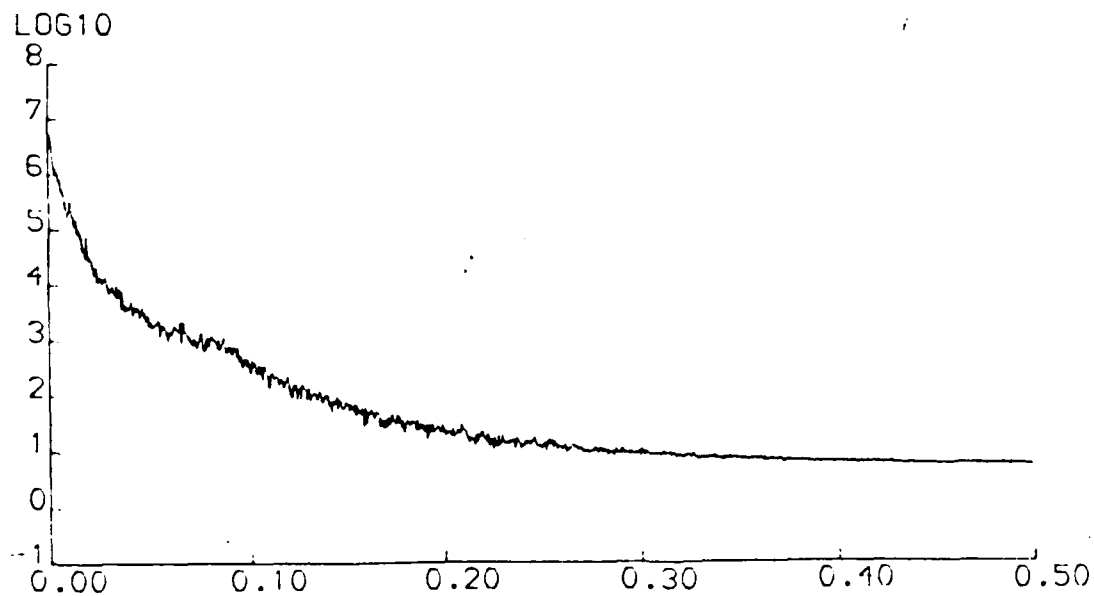
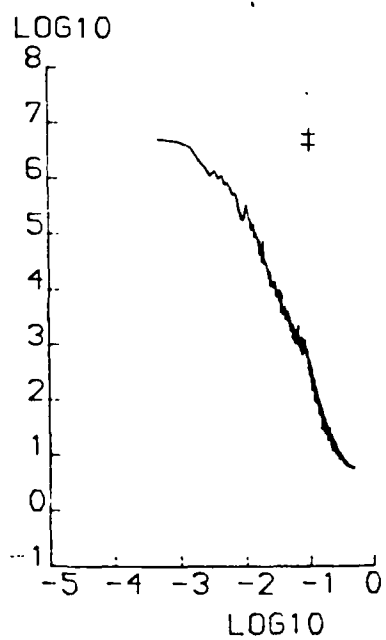
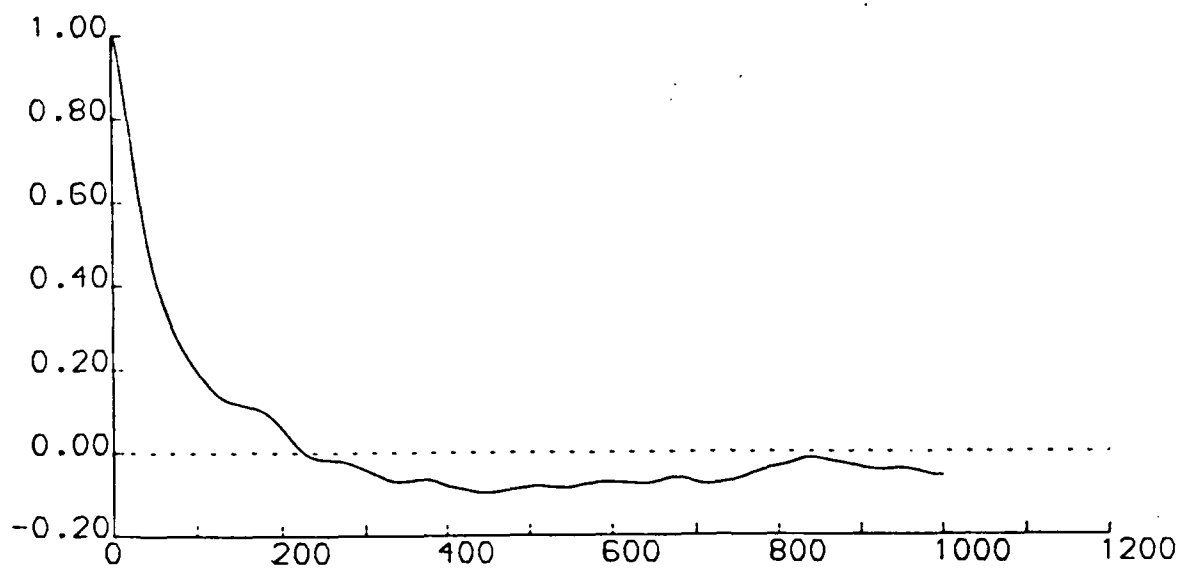


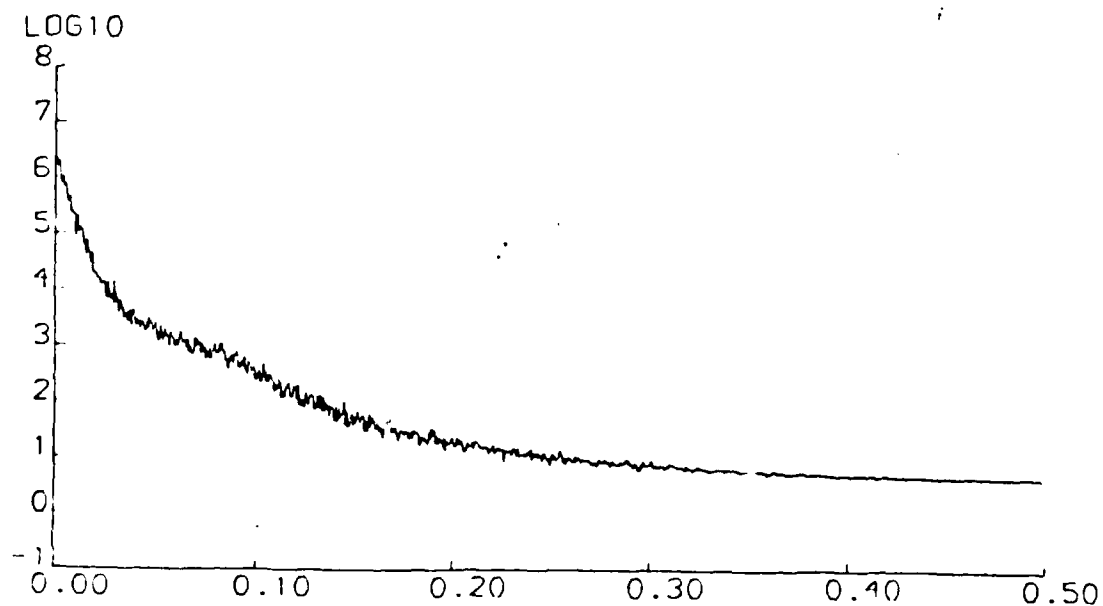
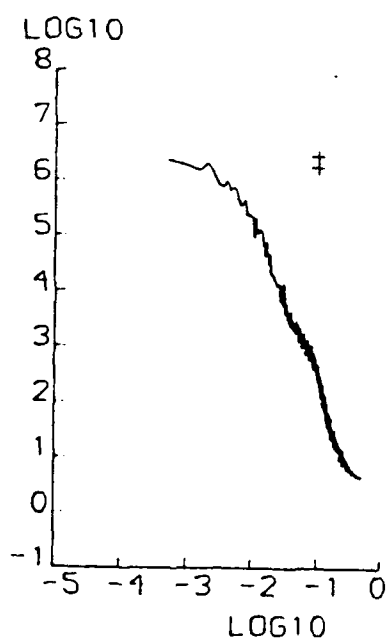
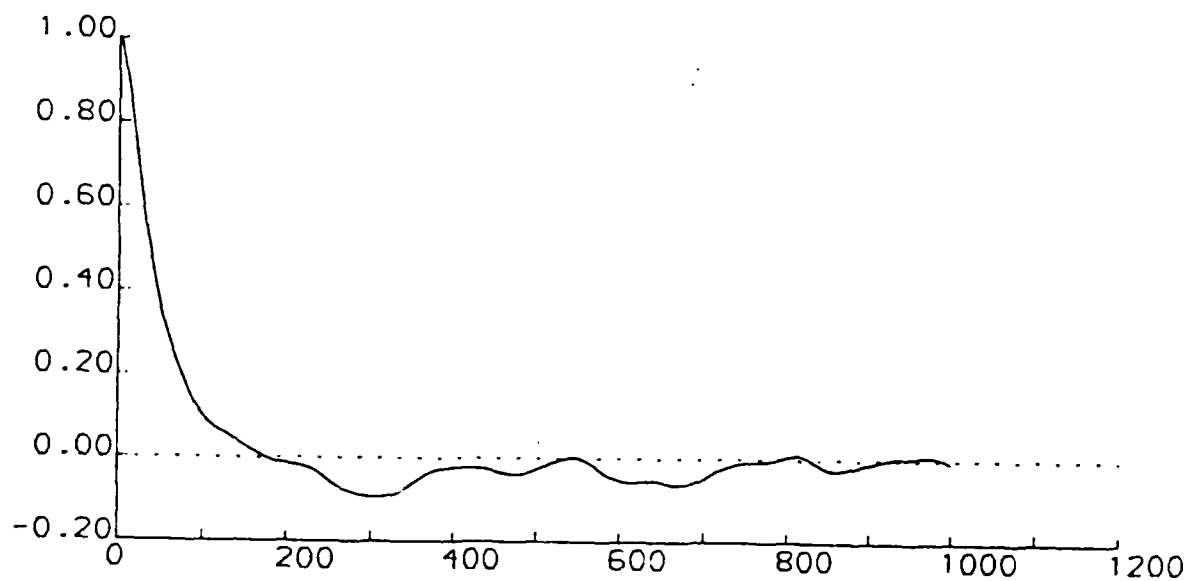


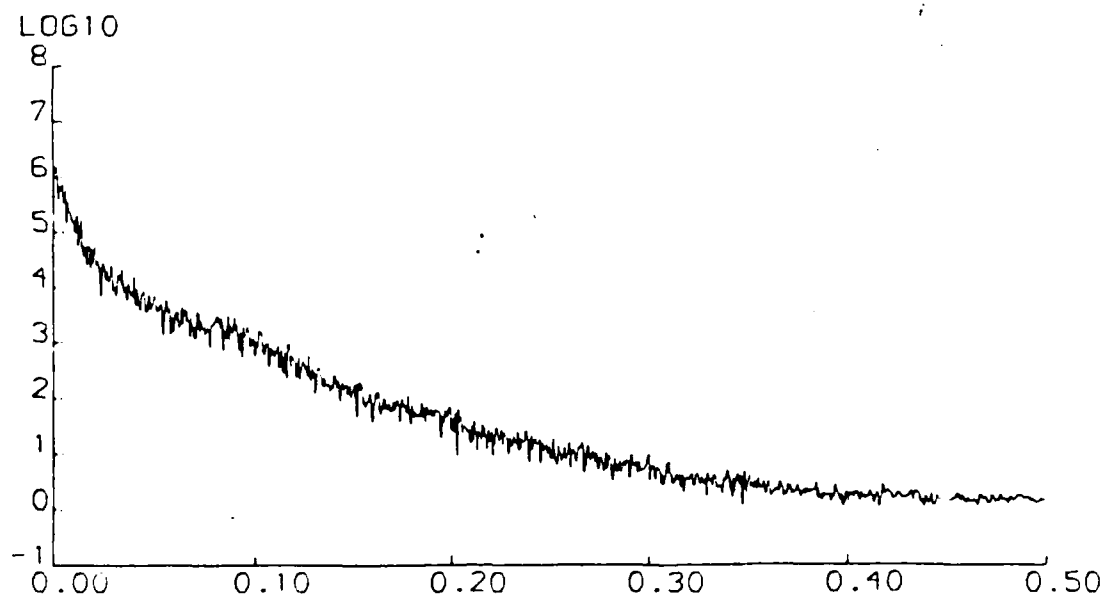
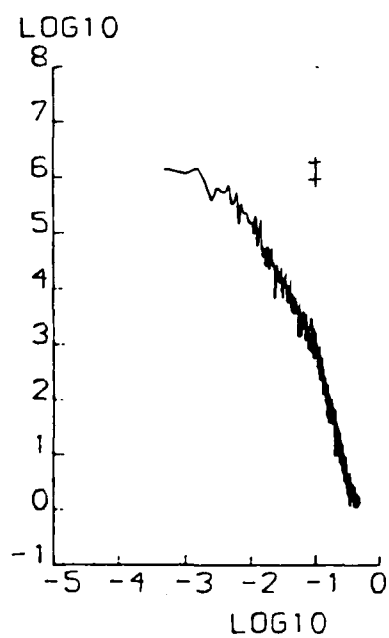
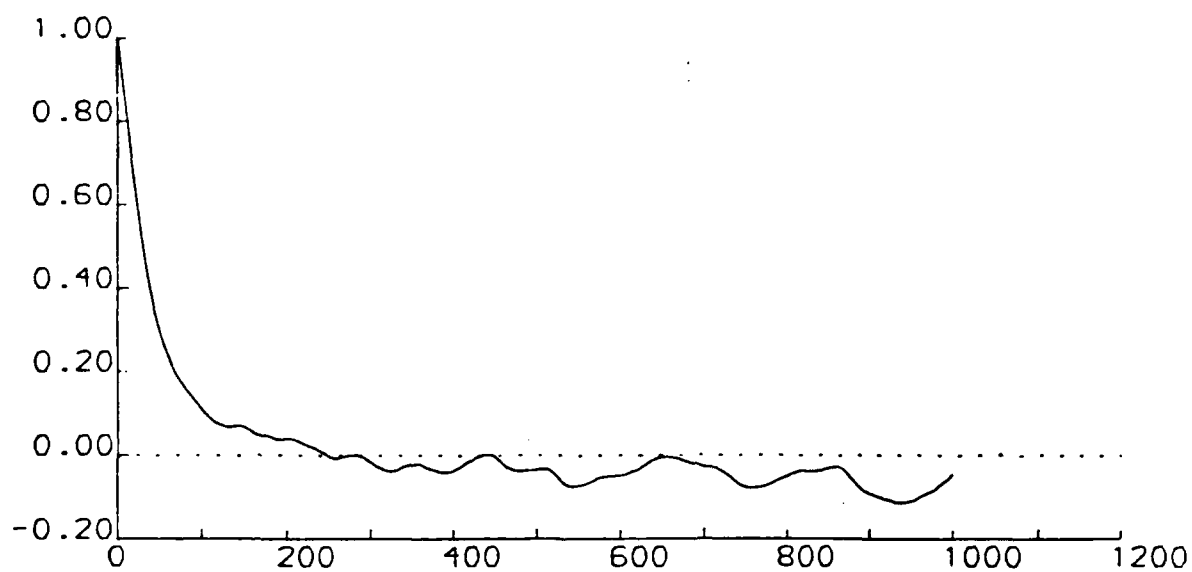


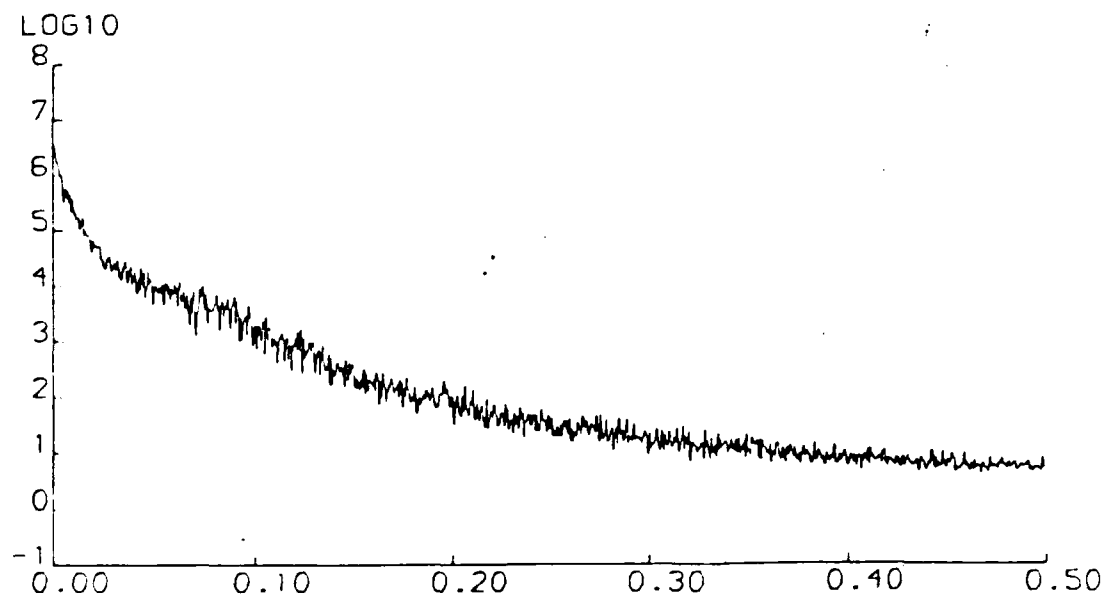
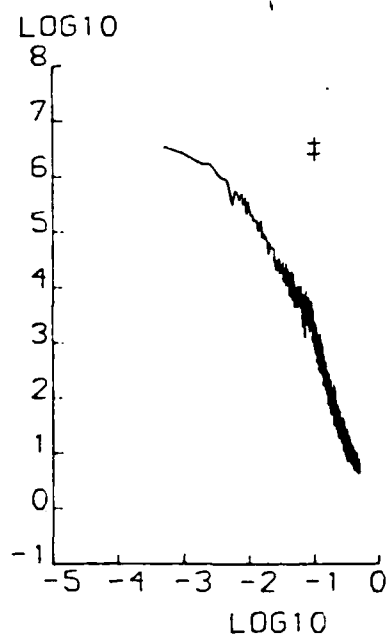
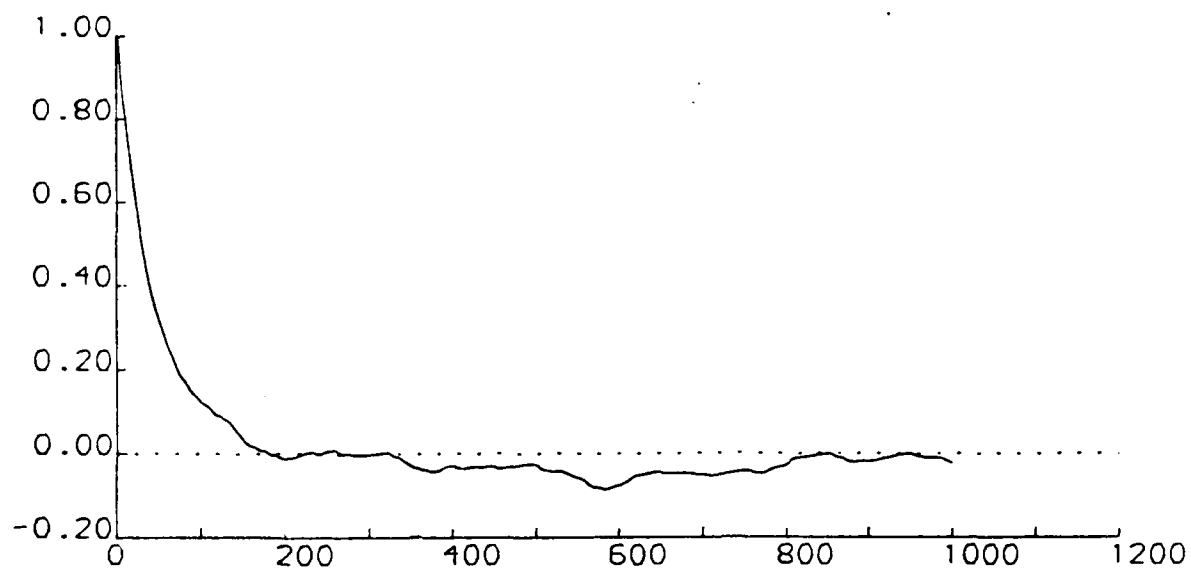


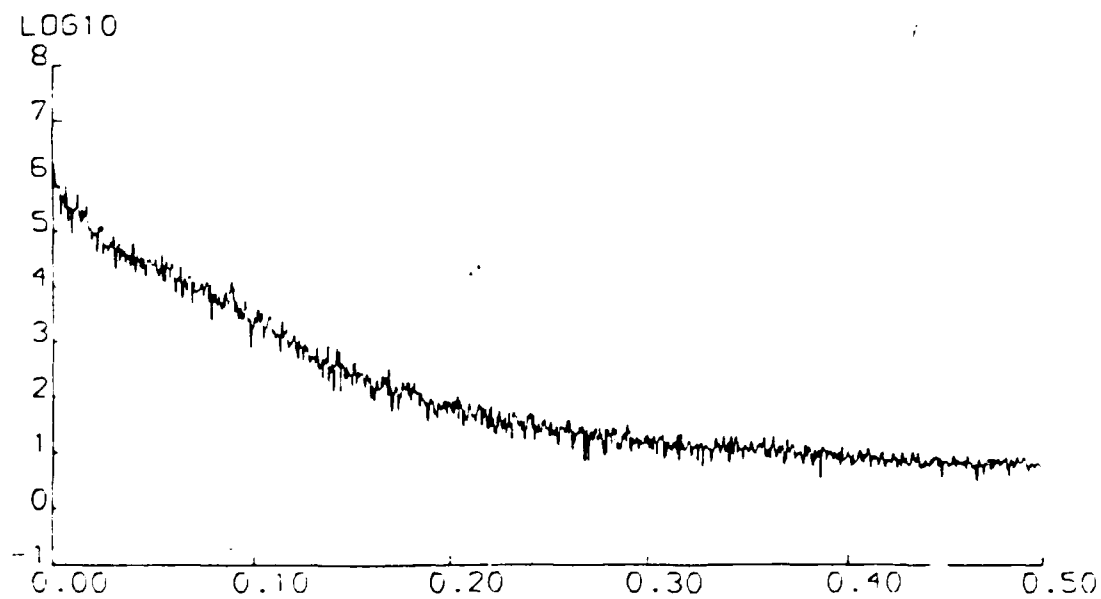
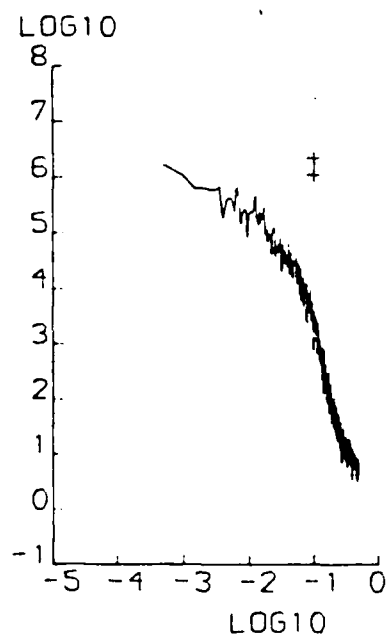
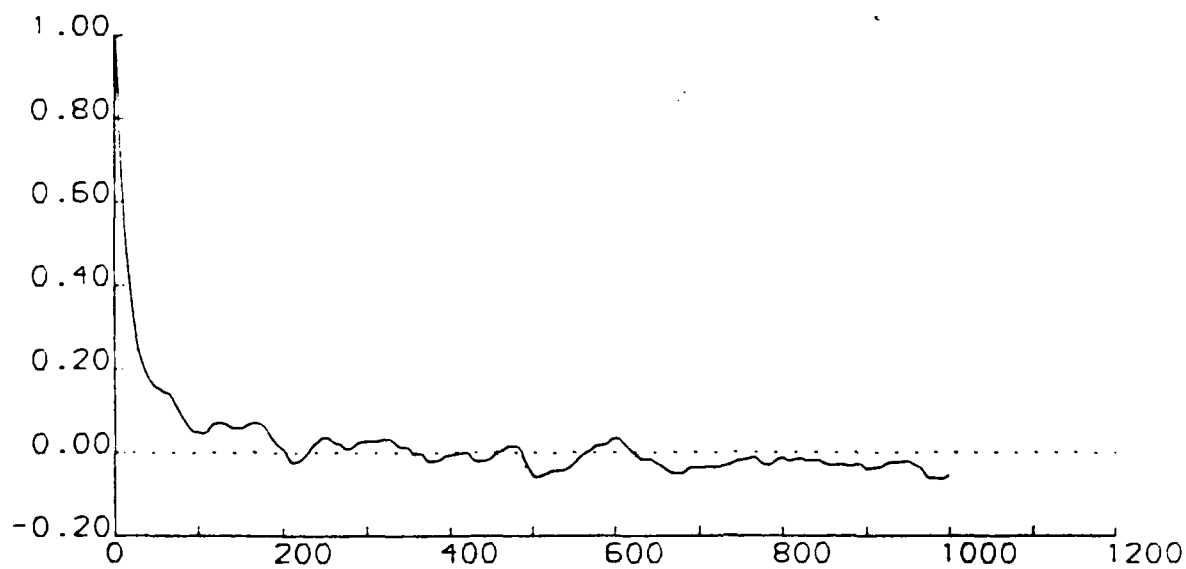


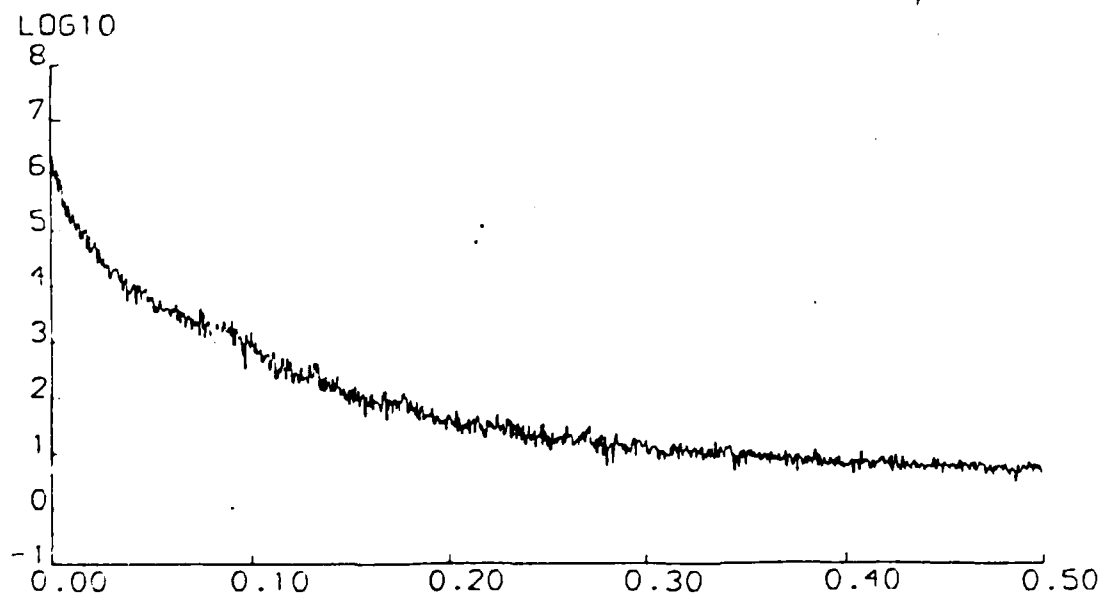
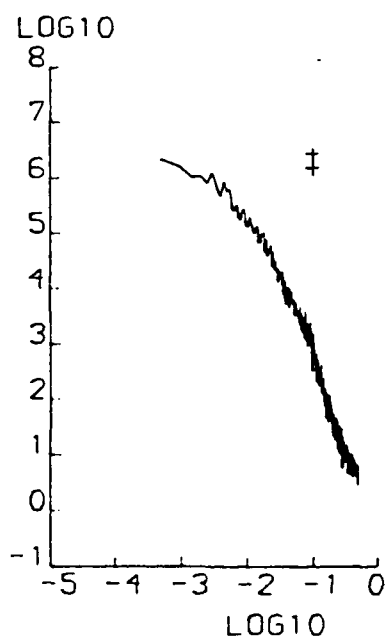
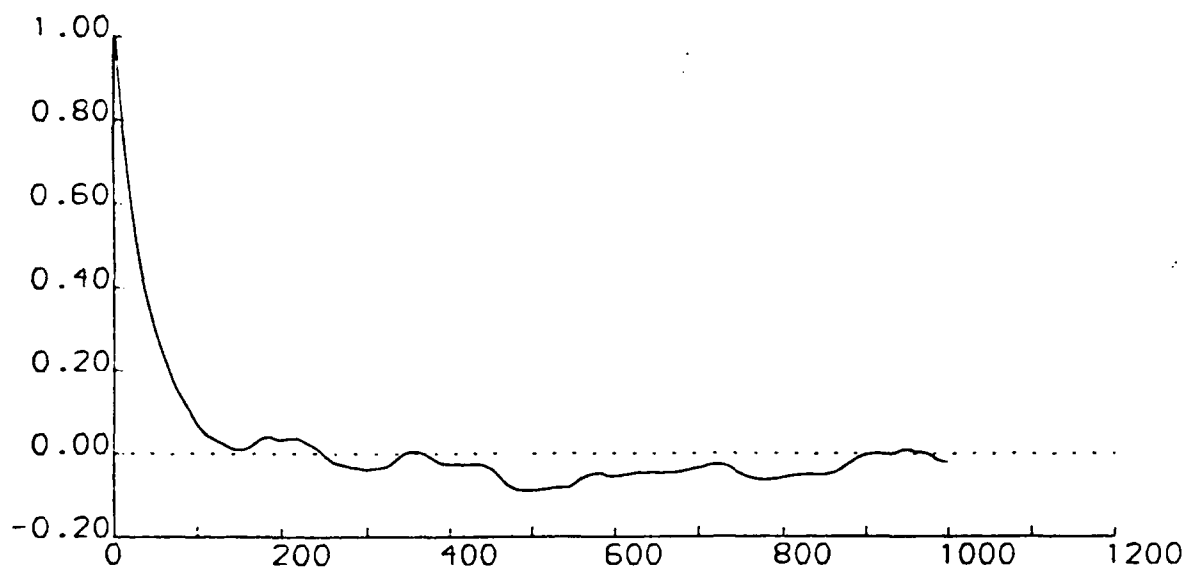


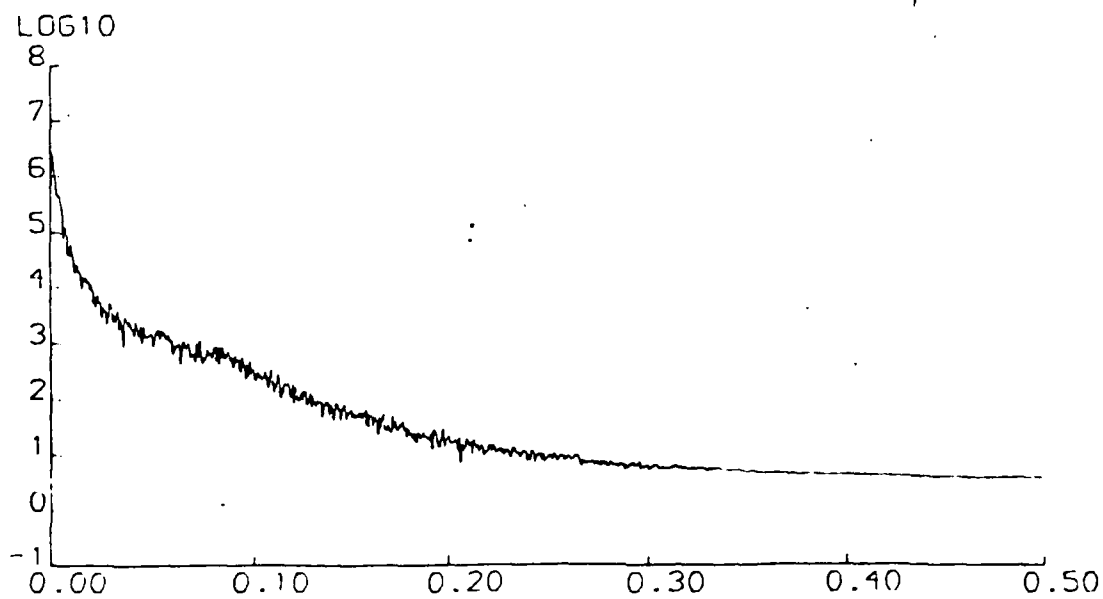
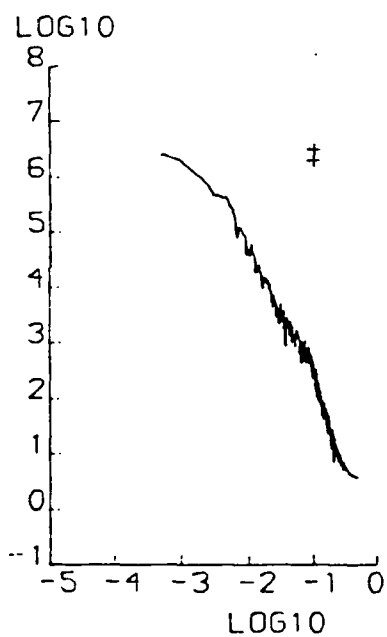
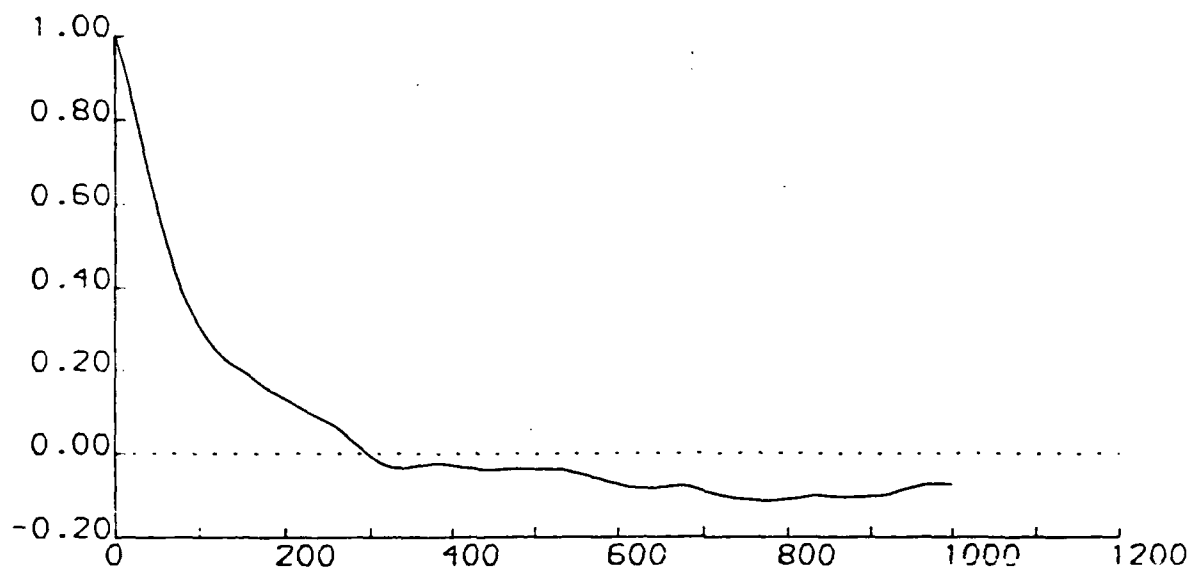


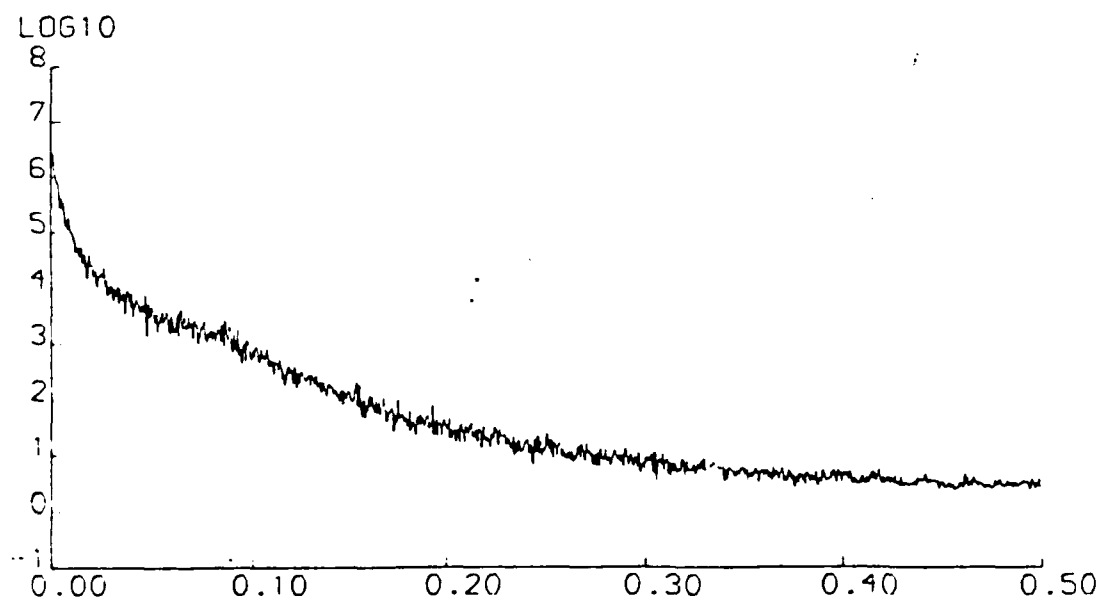
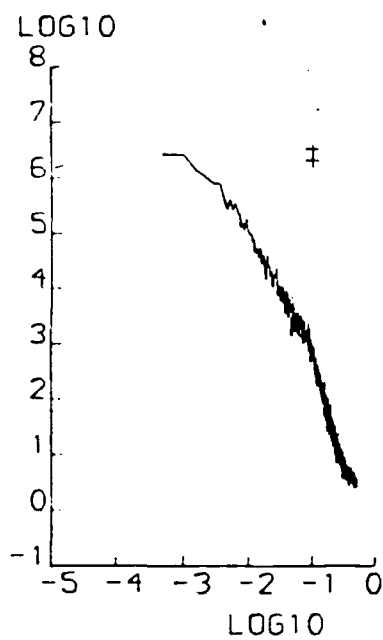
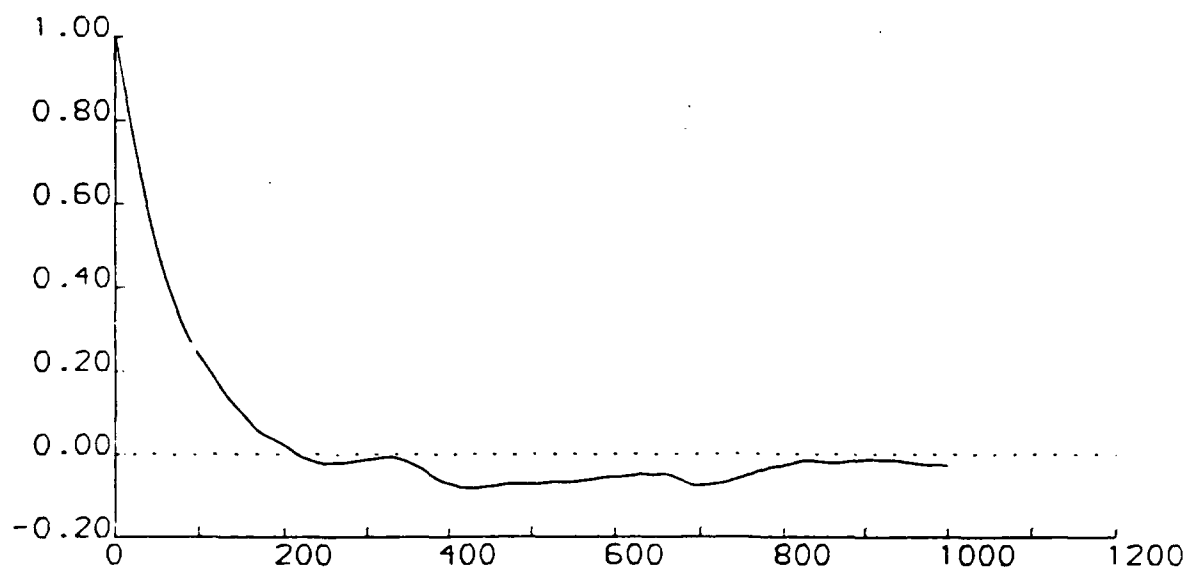


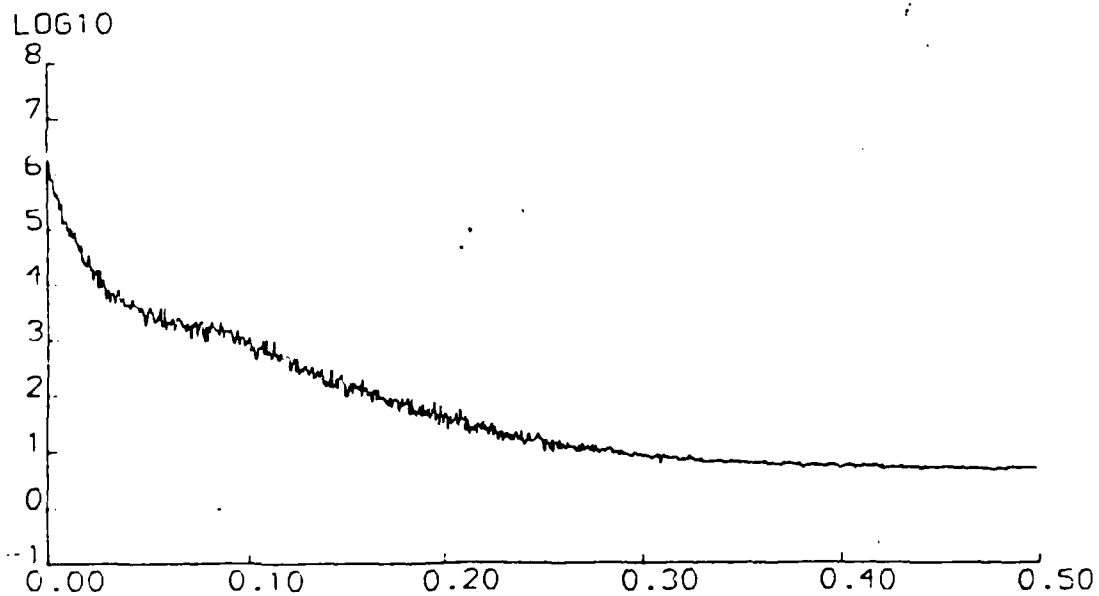
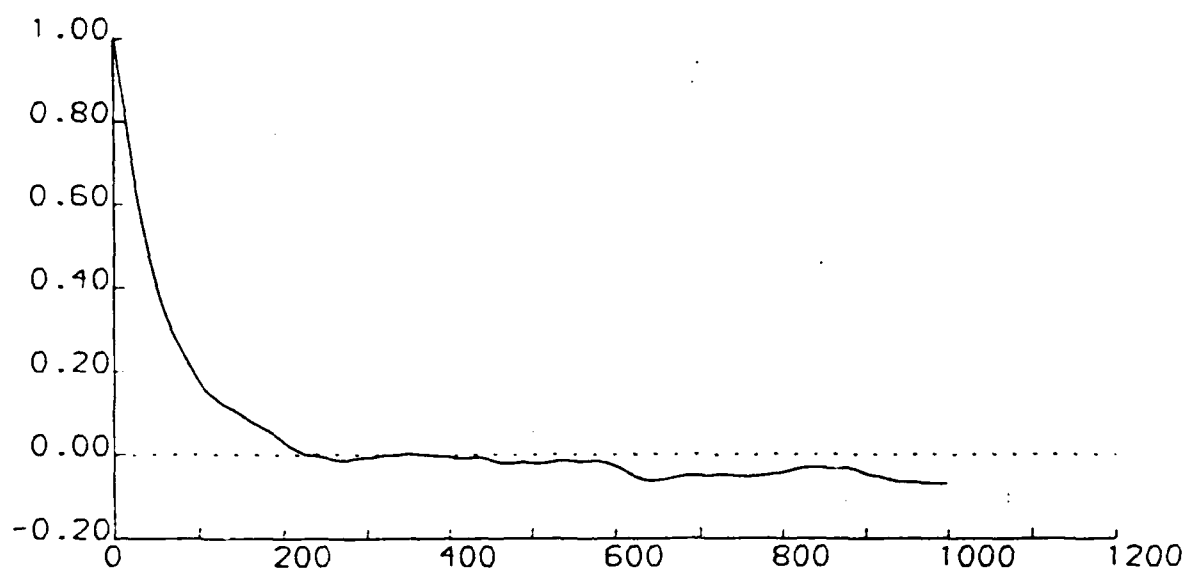


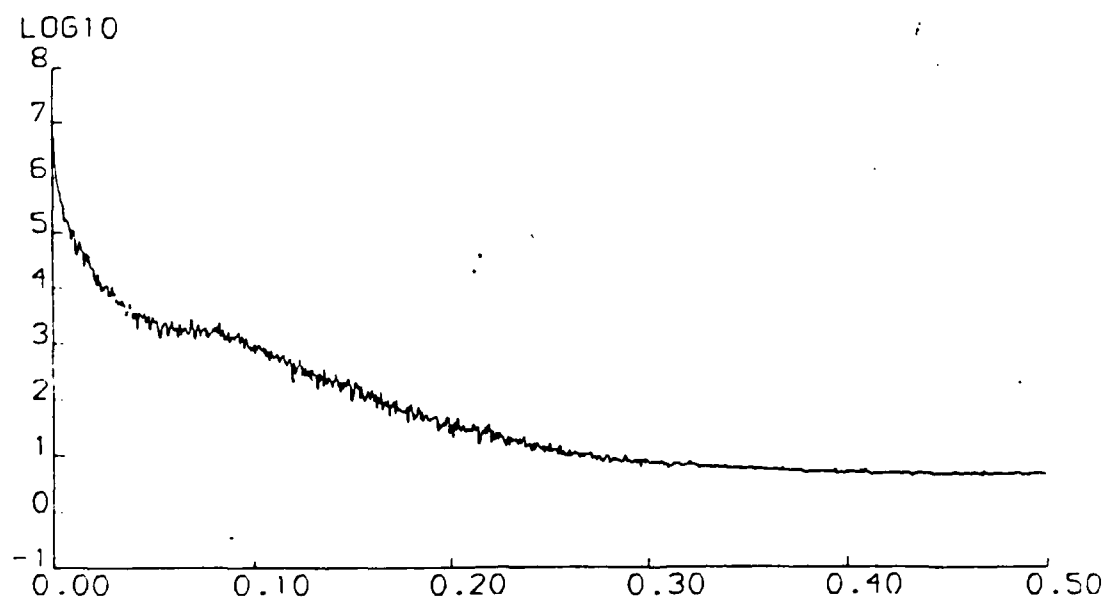
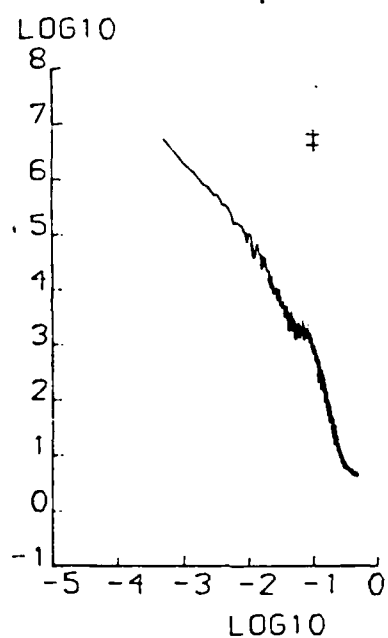
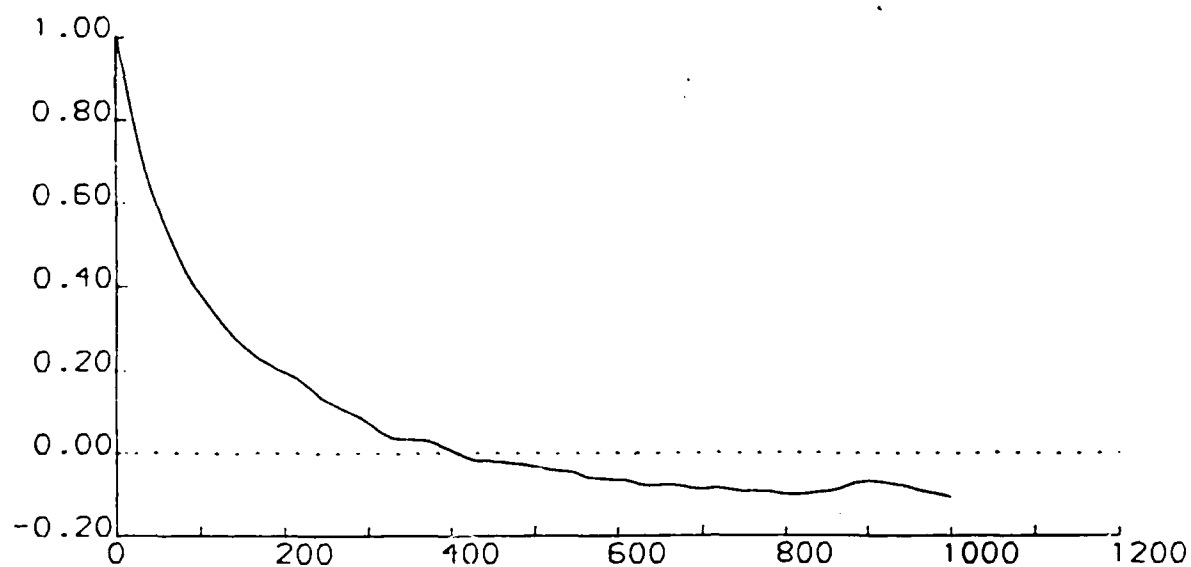


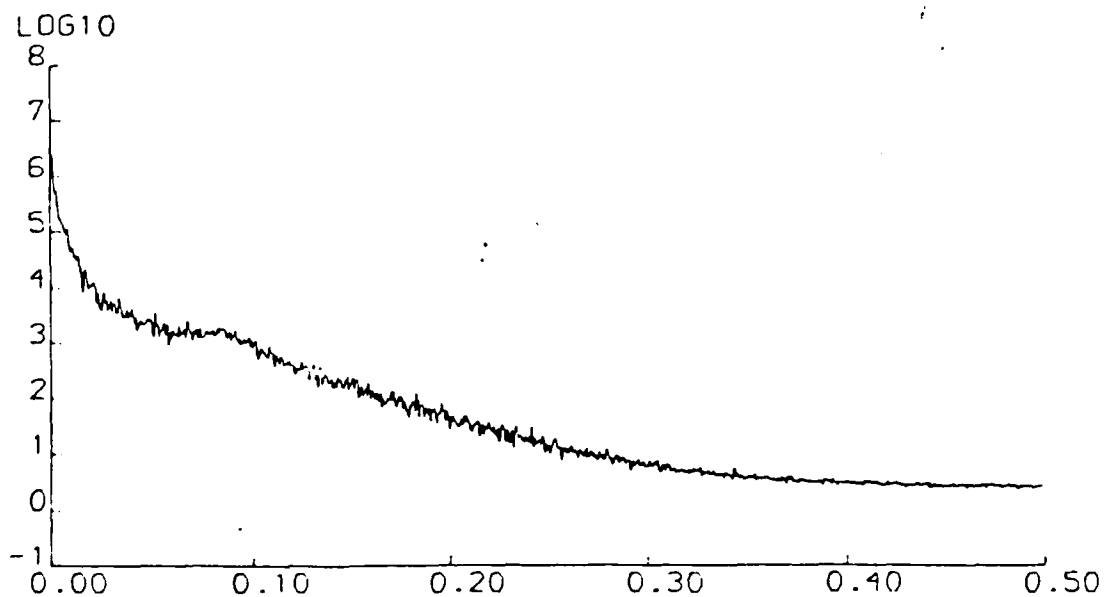
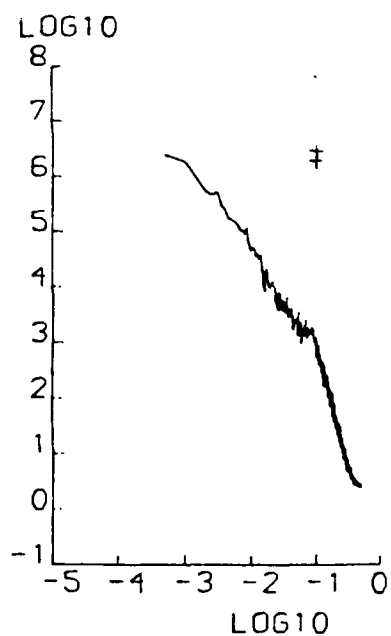
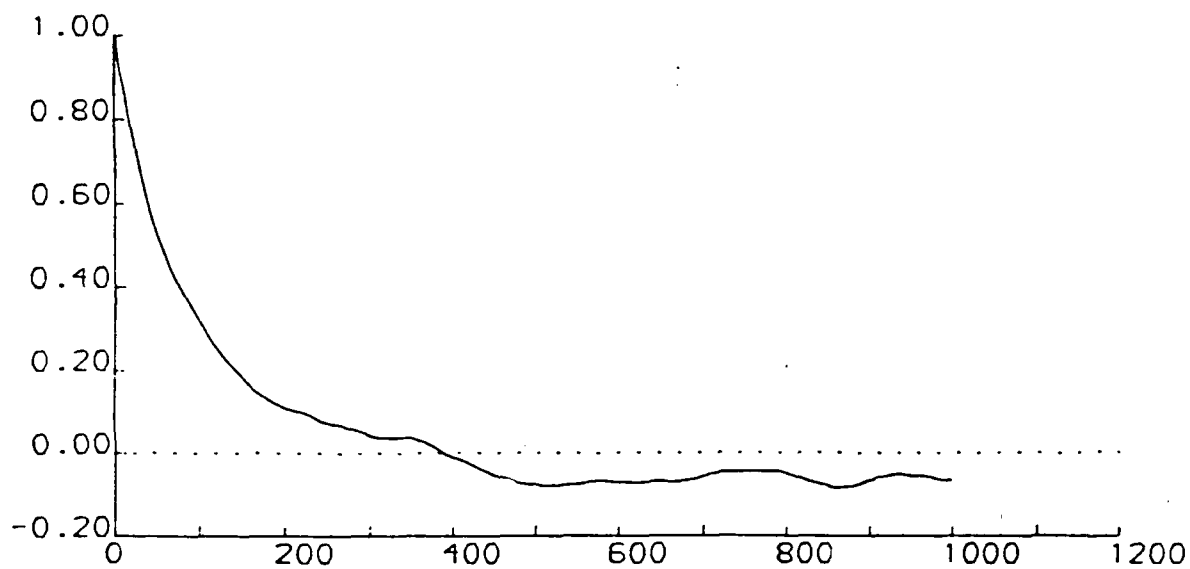


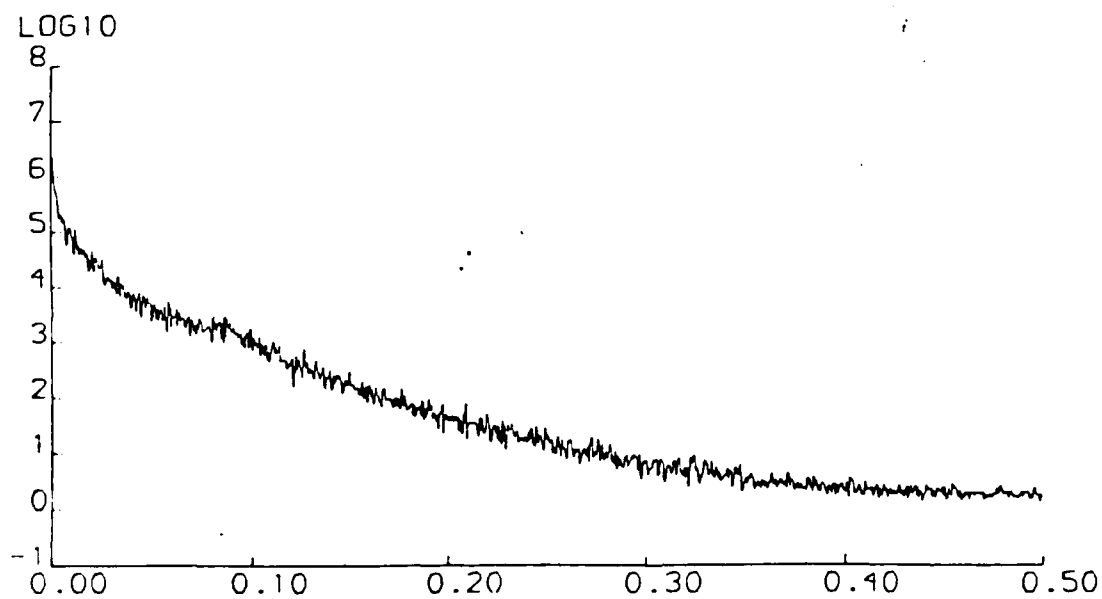
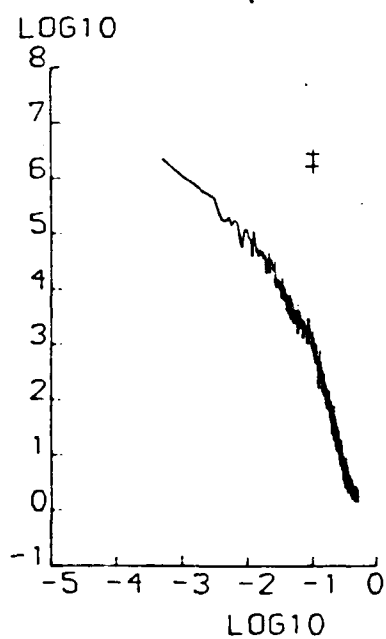
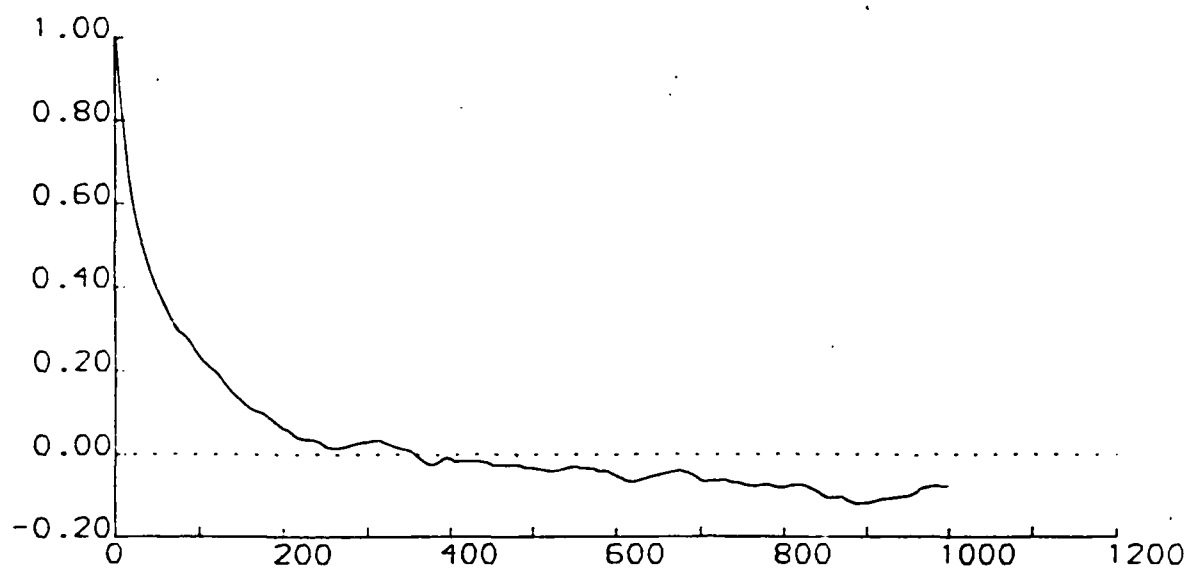


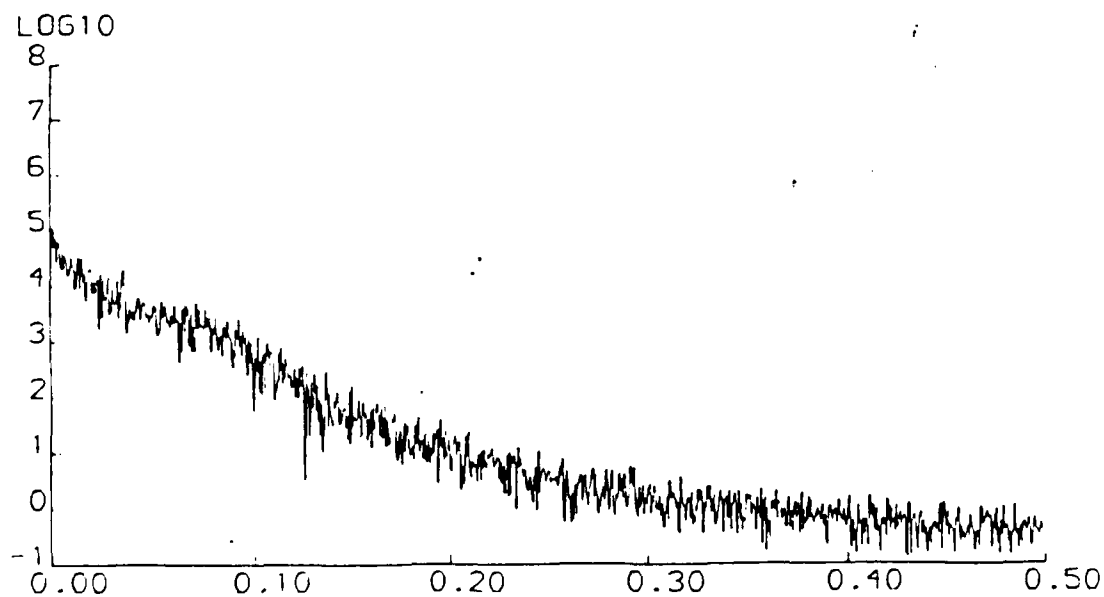
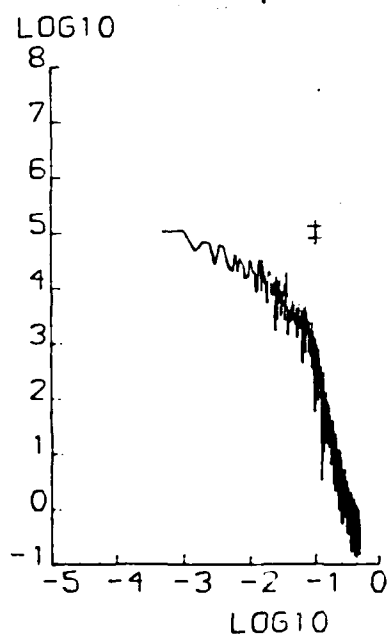
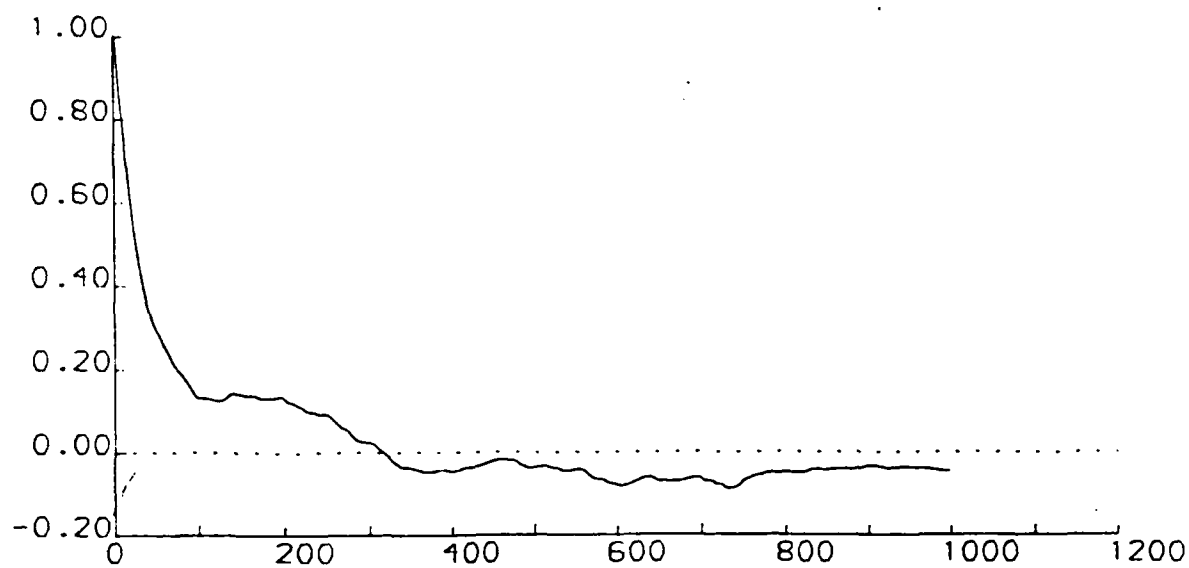


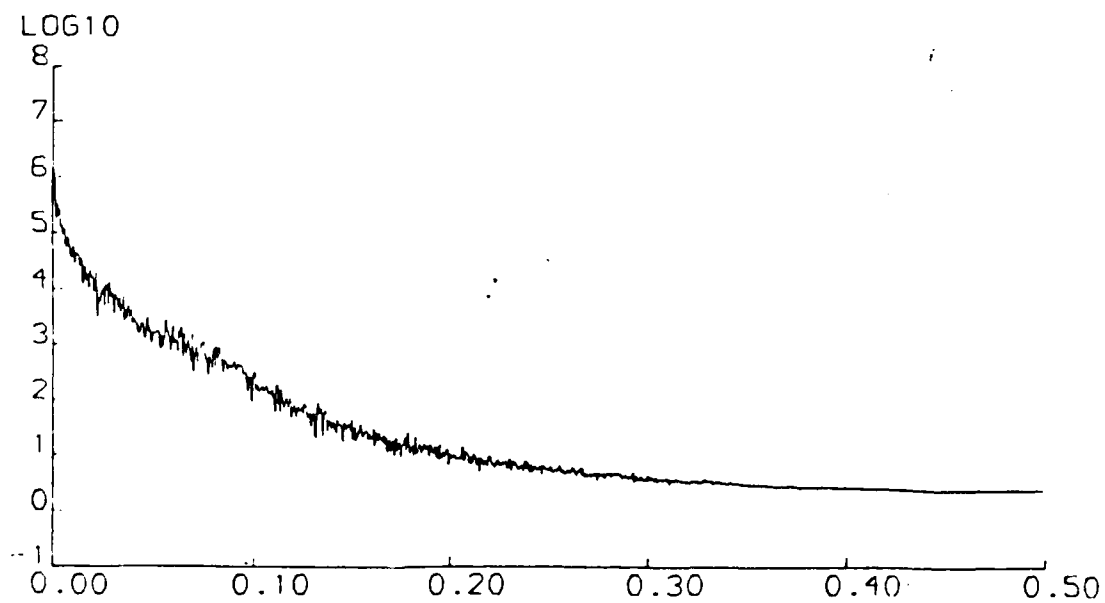
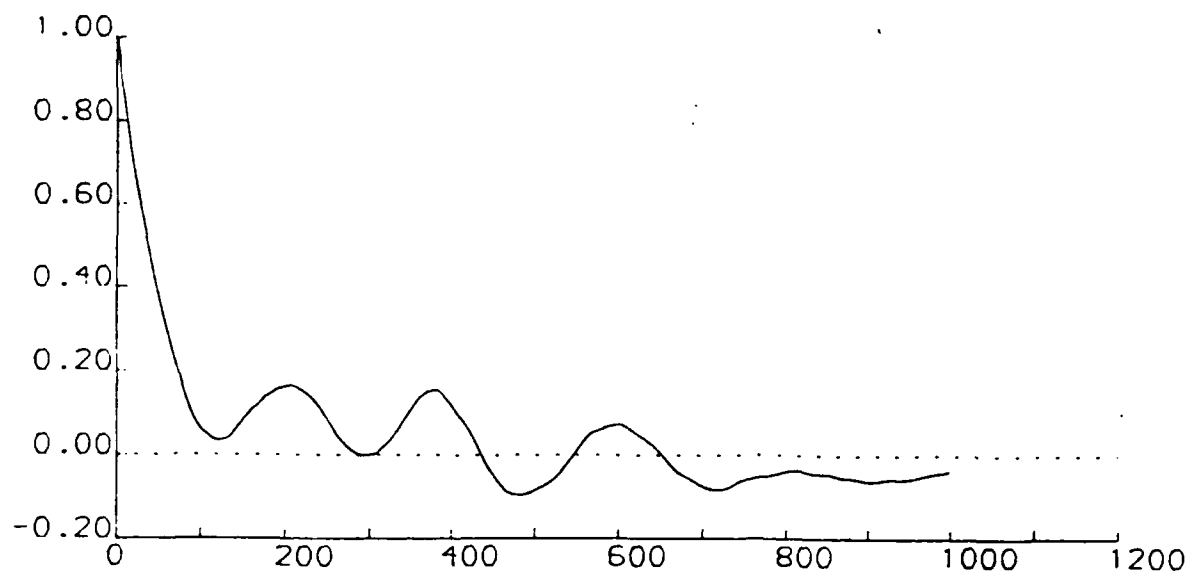


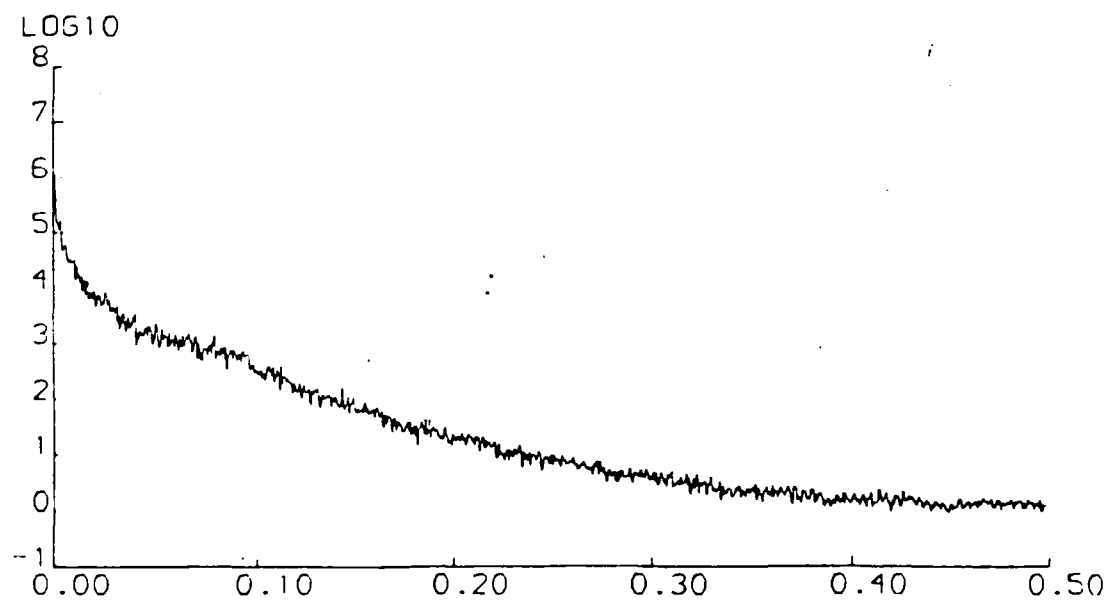
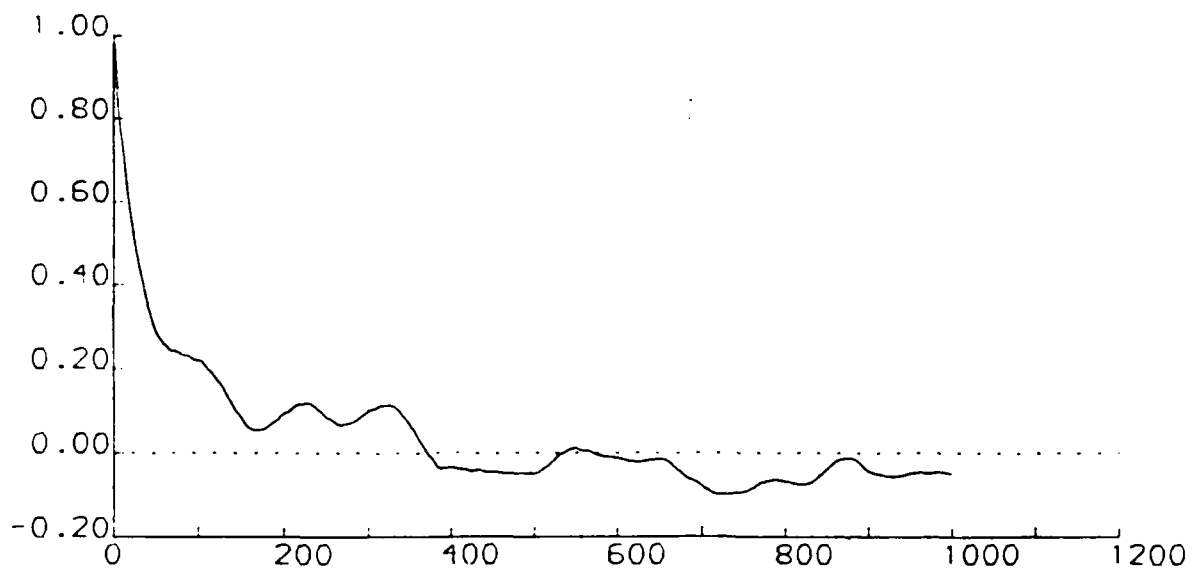












**STATISTICAL PROPERTIES OF ARCTIC SEA ICE MORPHOLOGY DERIVED
FROM SIDESCAN SONAR IMAGES**

C B Sear¹

&

P Wadhams²

4 October 1990

¹ Science Applications International Corporation,
Polar Oceans Associates. Block A2, Westbrook
Centre, Milton Road Cambridge CB4 1YQ, United
Kingdom.

² Scott Polar Research Institute, University of
Cambridge. Lensfield Road, Cambridge CB2 1ER,
United Kingdom.



ABSTRACT

Using a transparent overlay technique, the authors have classified a 140km long stretch of sidescan sonar imagery of the Arctic sea ice underside (700m swath width) into regions occupied by unique ice types. The categories used were multi-year ice, first year ice, pressure ridge, apparently open ('dark') lead, apparently refrozen ('bright') lead and randomly deformed ice. The validity of the technique was tested by comparing these classifications with data obtained simultaneously using a narrow beam upward-looking sonar. The resulting pattern of ice types was tested statistically for associations between adjacent regions, the distribution of lead widths, spacings and orientations and the distribution of ridge spacings and orientations.

Significantly non-random sequences of ice types were observed, lead orientations and spacings were clustered and were set to preferred values, and ridge spacings fitted a negative exponential distribution. The quantity of uniformly deformed ice (with no apparent linearity) was much greater on the underside of the ice than has ever been observed on the upper surface.

1 INTRODUCTION

A multi-platform study of Arctic sea ice, including sensors both below and above the ice, was carried out in May 1987 (COMISO et al. 1990; WADHAMS et al. 1990). Here we discuss the analysis of sidescan sonar data collected under the ice by a British submarine which provided a defined pattern map of sea ice type for a region north of Ellesmere Island, in a zone of intense deformation. These data provide a first opportunity, to differentiate unequivocally ice types for this region in winter and thereby provide important validation data for remote sensing.

The sea ice cover of the Arctic and Antarctic has a complex and variable morphology. It presents an intimate mixture of ridges and hummocks, open and refrozen leads and undeformed ice of various ages and thicknesses. To date, most statistical treatments of the ice cover have dealt with it as a sum of distinct structural elements (typically ridges, undeformed ice and leads) which can be analysed separately. However, there have been fractal treatments of sea ice cover (ROTHROCK and THORNDIKE, 1980) which ignore such distinctions and treat the ice surface as a single statistical process.

The elemental approach has been used in the statistical analysis of one dimensional ice profiles, derived from upward-looking sonar profiles of the ice underside and laser profiles of the upper ice surface. This is justified by reference to the characteristics of two-dimensional imagery of the ice surface, such as aerial photographs. However, imagery of the upper ice surface is often misleading because, during ice deformation, most of the deformed ice is thrust beneath the existing ice surface, giving the ice underside a much rougher morphology than the upper surface (with mean ridge keel width of 4.33 times mean ridge sail width, WADHAMS, 1981). The exaggerated relief of the underside of the ice provides information on ice draught and ridge morphology not readily obtainable from above.

Clearly, to achieve an adequate picture of the real structural elements which make up the ice cover, it is necessary to examine two-dimensional imagery of the ice underside as well as of the upper surface. Small areas of the ice underside may be photographed but the only adequate means of obtaining of large areas of imagery is by acoustic imaging.

The first attempts to image the underside of sea ice were made by lowering a rotating transit sonar through holes in the ice (KAN, CLAY and BERKSON, 1974) giving imagery over a circle of limited radius. Imaging from a moving platform using sidescan sonar was recognised as a more effective technique. Sidescan sonar (TUCKER and STUBBS, 1961) employs a vertical fan-shaped beam which is narrow in the fore-and-aft axis and wide in the athwartships (broadside) axis. An acoustic shadow picture can be obtained of the terrain over which the sonar is being towed. Normally two channels (port and starboard) are used to construct the total beam pattern. Sidescan has been used extensively to survey seabed features and was first successfully used to survey ice in 1976 (WADHAMS, 1978). The sidescan sonar towfish was inverted and mounted on the upper casing of a British submarine, which profiled the ice from below at a depth of about 75m. 40km of image data were collected before failure, proving the value of the technique. The data also demonstrated that the ice bottom surface was, indeed, much rougher than the topside, to the extent that individual pressure ridges are often obscured by fields of apparently random rubble.

In May 1987, this type of experiment was repeated, with a sidescan sonar fitted to another British submarine, as part of a joint submarine-aircraft remote sensing experiment in the Arctic Basin and Greenland Sea (COMISO et al. 1990; WADHAMS et al. 1990). Some 3000km of imagery was obtained from both channels, of which about 1000km was generated at low submarine speed and was generally of the highest quality (some examples are shown in WADHAMS, 1988 and GUOLIANG and WADHAMS, 1989). This imagery of the underside of sea ice is by far the most extensive yet obtained. Here we report on the results of an analysis of some 140km of this imagery in terms of structural elements and compare



the results with previously known properties of the ice cover.

Our aim was to produce, for the first time, an ice type map derived from submarine data, as a step towards generating a transfer function between the under-ice surface and the upper surface. This allows us to test the reliability of ice type identification from above and below. In addition, we can generate useful statistics from the sidescan data, such as the distribution of pressure ridge orientations and lengths, the relative percentages of first year ice and multi-year ice present, the prevalence and orientations of ridges and the distribution of sizes of individual ice floes.

The sidescan data set is a 140km stretch of imagery obtained from north of Ellesmere Island (approximately 85°N). This stretch was chosen for study because good data were obtained from other remotely sensed data sets which overlapped the submarine data. Shorter stretches of 60km and 12km within this were studied intensively in a previous exercise in data comparison (COMISO et al. 1990; WADHAMS et al. 1990).

2 DATA AND DATA PROCESSING

The sidescan sonar profiles were obtained using an EDO Western Model 602 towfish mounted on the submarine's upper casing, aft of the fin. This fed an EDO 706 sidescan in roll form, mapping system, operating at 100kHz, producing output, in roll form on electrically sensitive paper. The geometry of sidescan operation is shown in Figure 1. The towfish contains two transducers, each of which emits a wide beam (beamwidth 2β and depression angle α). These are normally arranged so that the two main lobes overlap at the zenith, giving a relatively uniform signal strength at all angles of incidence. Sound scattered from the ice surface is then received at a time delay (from pulse emission) of $2r/c$, where c is average sound speed through the water from the surface to the transducer (h). Raw sidescan data comprise a map of signal strength against time, with time being converted into range r . However, the EDO system



includes a slant range correction program, which converts range r into lateral distance d , by solving Pythagoras' equation. Also, a variable chart paper speed can be keyed to the boat's speed (V), such that the final product is a 'map' of the ice underside which appears to be geometrically correct.

It should be noted that the geometrical validity of the sidescan image is subject to the following sources of error:

- a) errors in the manual entry of h , V and c . Of these, c is minor; V produces a stretching or squashing, and h produces a loss of data near zenith or a gap along the centre line of the image.
- b) if a pressure ridge has significant draught relative to h (which is often the case), the peak of the ridge will be displayed at a smaller lateral distance than is correct.
- c) if the submarine has a list there will be a mismatch between the reconstructed mapping of the port and starboard channels. This leads to a discontinuity in the line of a pressure ridge crossing the zenith.

In addition, there is always a variation in data quality across the image, since underice protuberances are identified by their acoustic shadows, which are shorter near zenith. This improved ability to detect objects at larger slant ranges is offset by the general decrease in backscatter strength, which sets a limit to the swath width which is imaged.

In summary, the primary data product from this system, was a nominally correct map on electrically sensitive paper of the ice underside out to a lateral range of 500m either side of the zenith (a 1km total swath width).

Figure 2 is an example of the imagery obtained. It shows a photograph of a portion of the sidescan chart roll record. The width of the sidescan swath is 1km and the length of imagery shown in Figure 2 is about 1.5km. Based on the

experience of one of us (PW) in identifying sea ice types from above and below, it was possible to classify the sidescan trace. A series of transparent overlays was prepared of the sidescan sonar imagery, working from photographic prints. It was found that image quality declined severely beyond 350m on either side of the centre line (see Figure 2). On each print, a rectangular area was framed off within which the sonar backscatter was strong enough to give a clear image. Thus, this frame represented a swath width of approximately 700m, centred on the submarine track (zenith) and was typically of length 1200 to 1500m (depending on the ratio between submarine speed and sonar chart speed). Within each frame the whole area was divided into classes which represent different ice types, as interpreted by an experienced analyst.

3 SIDESCAN CLASSIFICATION

The ice types used and the criteria for identification on sidescan imagery (and upward-looking sonar profiles) are shown in Table 1. A total of 85 frames of sidescan sonar were analysed. Initially, classification was based solely on interpretation of the texture of the underside of the sea ice. For example, linear features that appear 'flat' and relatively dark on the sidescan are classified as leads, whereas bright linear features with shadowing on one side look like ridge keels. Some comments on interpretation are given below.

a) Multi-year ice (m) is a coherent area of ice field with a rugged appearance, featuring distinctive 'bulges' like inverted lunar craters on an otherwise smooth local topography. These bulges are unaccompanied by corresponding depressions and are discussed further in WADHAMS (1988) and WADHAMS and MARTIN (1990). This experiment provided the first evidence of this distinct and easily recognisable topography for multi-year ice.

b) First year ice (f) is characterised by a smooth underside, frequently criss-crossed by a pattern of narrow cracks.

c) Ridges (r) are clearly identifiable as a linear set of broken ice blocks. Where several ridges appeared to cross or run in parallel, an attempt was made to trace the crest line of each individual ridge (ridge crests were marked on overlays and subjected to statistical analysis).

d) 'Bright' leads (L1 or l) are narrow linear stretches or areas, which possess a bright sonar return, characteristic of a smooth surface with a relatively poor backscatter, giving mainly specular reflection. Our assumption was that these areas correspond to thin, smooth ice and that such leads were recently refrozen. In most cases the concurrent upward-looking sonar data supported this assumption but in a few cases a 'bright' lead correspond to an upward-looking sonar return characteristic of open water. Thus, the classification of leads remains equivocal. This is discussed further in section 4.4 below.

e) 'Dark' leads (L2 or w) give a strong sonar return, characteristic of high local roughness. These were assumed to be open portions of leads, ruffled by the wind.

f) Matrix (Mx) are areas which comprise deformed ice blocks (as opposed to undeformed ice) but where the blocks have no identifiable linearity which would allow separation into distinct linear pressure ridge keels. Such areas are common in this data set, as they appeared to be in the 1976 data set (WADHAMS, 1978). This is another of the important ice characteristics revealed by sidescan sonar, because it is seldom that large areas of random deformation occupy the upper surface of sea ice. After the classification of the imagery into the other categories, areas of matrix remained and were therefore rarely simple, bounded shapes.

g) Unknown (u) was used for bounded regions that fitted none of the other categories. This was generally because of poor sonar return, near the outer limit of range resolution.

Figure 3 (immediately below Figure 2) shows the classification of the stretch of sidescan image shown in Figure 2.

In order to provide statistics of ridge orientation, the angle subtended between each ridge crest and the centre line of the sidescan imagery was specified. Finally, all features (other than matrix) that were not completely enclosed by the sidescan swath (and thus were not complete on the imagery) were classified as edge features in order that they could be removed from analyses of feature statistics.

Our classification indicates that the appearance of organisation (ridges and floes) on the ice upper surface does not necessarily correspond to such organisation in the deformed ice blocks which are thrust beneath the surface. The keels of closely spaced ridges must interact at times to give a random appearance to the underside. Matrix is so prevalent in the dataset examined that, on average, it occupies half of each overlay. Another reason for the prevalence of hummocky, deformed ice is that the experimental area was in the heavily ridged region north of Greenland.

4 ICE TYPE CLASSIFICATION ERROR ANALYSIS

The ice type categorisation on the overlays was deliberately carried out without reference to the accompanying upward-looking sonar ice draught data, obtained by a 45kHz narrow-beam transducer. The sidescan-derived classifications were then compared with the upward-looking sonar data. Classifications which were judged to be false in the light of this comparison were changed. Clearly this could only be done for ice features which straddled the zenith. This section analyses the frequency and types of mis-identification that were found. It represents an assessment of the quality and reliability of the final overlay data product.

In an upward-looking sonar record, ridges can be clearly distinguished from normal multi-year undulations because of the steepness and complexity of the ridge structure. Also, open water in leads gives the profile a 'grassy' appearance. This is a product of the saturation of the sonar recorder because of the high reflection coefficient at

the water-air interface, as opposed to the water-ice boundary. Multi-year ice is distinguishable from first year ice by the former's greater draught and rough, (rather than smooth) surface. In this way, features which crossed the zenith of the sidescan image were compared with the corresponding ice draught profile. Not all features could be inspected, but the confirmed sample gives a measure of the accuracy of the overall classification. Table 1 shows the criteria used for the classification of sea ice using upward-looking sonar profiles.

4.1 Errors and reliability

In classifying the sidescan, two classes of error were possible. A feature, clearly identified using the upward-looking sonar record, might be missed by the analyst when classifying the sidescan because the image was degraded or otherwise difficult to identify. Here, such an error is called a Type A error. Alternatively, a feature seen on the sidescan could be classified incorrectly. We call this a Type B error.

The results are summarised in Tables 2 to 4. Table 2 shows the numbers of original identifications which were found to be correct and which were erroneous. The data comparison was carried out for 86 frames, representing about 140km of track. 767 separate ice features from the initial identification were found to straddle the zenith. An identification was declared to be erroneous if the upward-looking sonar record demonstrated that a different classification was appropriate, even if that classification included the original ice type as part of itself (for example, the addition of a pressure ridge to the centre of an area of matrix, turning it into a ridge and two areas of matrix).

The results shown in Table 2 indicate that on sidescan imagery, the most reliable identification is of pressure ridges. Only some 3% of identifications were erroneous. It is clear that multi-year ice identification was also reliable (87%) but that the identification of first year ice was not very reliable. Only 35% of first year identifications were confirmed by the upward-looking sonar.

A possible reason for this is that the comparison was done along the sidescan zenith, where ice roughness is particularly difficult to see because of the high incidence angle. We also note that the number of first year floes identified was much smaller than the number of multi year floes, which is a feature of the region in which the measurements were carried out where passive microwave monitoring has shown that the ice is usually mainly multi-year.

In about 28% of cases, the matrix category needed correction. This is partly a function of time constraints in the analysis. On each frame of the sidescan imagery, all areas not classified within half an hour were classed as matrix, allowing for the possibility of further subdivision of this class during a subsequent analysis. In almost all cases, 'unknown' areas could be positively classified by comparison with upward-looking sonar data.

The overall success rate is high, at nearly 78%. This confirms the suitability of the classification of sidescan for identifying ice types and regimes and also of the classification technique chosen. Table 3 shows the distribution of new identifications from the erroneous identifications in Table 2. This enables comparison of the number of Type A errors (missed features) and Type B errors (features identified as a given type which were actually not that type).

The use of upward-looking sonar as an aid to classification introduced more multi-year ice areas than were lost. In addition, a very large number of new ridges were introduced by the correction process, whilst almost all of the original ridge identifications are confirmed as being correct. First year ice identification was unreliable in both senses, with many failures to identify first year ice, as well as many identification which were false.

4.2 First year ice

First year ice is identified on sidescan by its smooth, uniform backscatter level and by the presence of narrow line cracks which often criss-cross its surface. The classification is confirmed on upward-looking sonar by a smooth bottom profile of draught greater than 1m but not exceeding 2m. First year ice was relatively scarce in this



region. Ice reaching this region has crossed the North Pole in the Transpolar Drift Stream and most of it is more than a year old. In addition, the net convergence it undergoes as it approaches the Greenland coast preferentially deforms the first year component of the ice regime.

The most common sources of error in identifying first year ice were: simple mis-identification of multi-year ice as first year ice (16 cases). This was because the multi-year ice appeared unusually smooth on the sidescan image, whereas it was identified on the upward-looking sonar by its thickness. Again, this appears to be an instrument problem, a function of the loss of contrast which sometimes occurred on the sidescan, near the zenith. Mis-identification of leads as first year ice (three cases of leads alone, one case of a lead and a ridge) is more of an analytical problem. Refrozen leads have a smooth appearance and are distinguishable from first year ice on sidescan alone, mainly by the shape of the feature. It requires upward-looking sonar to determine whether the ice is thicker or thinner than 1m. This is thought to be the criterion for a transition from a refrozen lead to first year ice.

4.3 Ridges

Ridges were usually clearly identifiable and the line of the ridge crest was marked on the overlay whenever possible. This enabled ridge axis orientation to be studied. There were four cases of mis-identification, compared with the 116 cases of successful positive identification. In two of the cases a refrozen lead was mis-identified as a ridge, because they were narrow linear features only a few metres across. However, upon further consideration of those images, the lack of ice block detail and shadows could have yielded correct identifications. In one case, a wide ridge was re-identified as matrix because upward-looking sonar shows it to have a complex rugged structure and further examination of the sidescan image failed to confirm linearity in the pattern of ice blocks. In one case a 'ridge' was found to be simply a line of strong return and shadow corresponding to an (un-ridged)



boundary between first year and multi-year floes. Overall, it is clear that positive ridge identification on sidescan is highly successful, although many ridges remained unidentified only to be revealed by consulting the upward-looking sonar profiles.

4.4 Leads

As noted in section 3 above, bright leads (l) were identified as those giving a bright sonar return, characteristic of a smooth surface with a relatively poor backscatter. The initial expectation of the analysts was that this would correspond to a recently refrozen lead containing thin, smooth ice. On the other hand, dark leads (w) would correspond to open water. Previous evidence, including observational evidence during surfacings and from upward-looking cameras, has shown that true open water gives a 'grassy' return on upward-looking sonar because of the high reflectivity of the water-air interface compared with the water-ice interface. This saturates the upward-looking sonar recorder levels. It was sometimes the case that open water (as identified by upward-looking sonar) corresponded to Type 1 features. In particular, in leads which were partially refrozen (as shown by the upward-looking sonar), the sidescan usually showed two ice types within the lead. The problem is that, in some cases, Type 1 corresponded to the open side of the lead and in some cases, Type w. There is a real physical problem here which requires detailed analyses of individual leads to resolve.

In view of this ambiguity, Types 1 and w were only corrected to make them internally consistent: all returns brighter than a certain level were re-classed as Type 1 by intercomparison between frames. This accounted for most of the 'corrections' to Type 1, although in one case a mixture of first year and multi-year ice floes had been mistakenly classified as Type 1 because of low contrast at zenith. In addition, there were no fewer than 12 cases of mis-identification of ridges as Type w. However, all these occurred in a single frame, of relatively poor image quality (worn stylus). On this frame narrow ridges were identified as leads because shadows from protruding ice



blocks in the ridges were not clearly distinguishable on the image. Thus, the lead errors indicated underestimate the success of lead classification on sidescan imagery.

As discussed above, it had been thought that a dark, strong return from within a lead must correspond to open water, which is ruffled by the wind and therefore presents a locally rough, strongly reflecting interface. This analysis has shown us that the situation is more complicated and that this assessment is not always accurate, necessitating a deeper study of the phenomenon of lead representation by sonar.

4.5 Error analysis summary

Table 4 shows how the correction procedure gives a revised distribution of ice types. Many more multi-year ice areas were introduced by the correction process than are lost by it. A large number of new ridges are introduced after validation using upward-looking sonar, indicating that sidescan alone is likely to underestimate the proportion of ridges in an ice field. However, almost all of the original ridge identifications are also confirmed as being correct. The classification of sidescan is not very efficient at identifying first year ice in a region of intense deformation. It requires additional information from upward-looking sonar. Following our error checking, proportions of first year ice and dark leads (l) were reduced somewhat, whilst the proportion of bright leads (w) remained the same. However, absolute numbers of features in each of these categories are small compared with other classes (8% of the total for l + w).

We also note that the total number of features is increased from 767 to 899, so the checking procedure enables a finer division into categories to be made. Despite the increased number of multi-year ice features present, the proportion of multi-year features remains almost unchanged, indicating that the original classification was a reliable estimator of the fraction of features that are multi-year ice. The proportion of ice matrix is reduced, reflecting the fact that this is to some extent a residual category, which can be partially re-assigned with the aid of upward-looking



sonar data. Chaotic jumbles of ice along track can be resolved into ridges and floes. Figure 3 is a sample of the verified ice classification discussed above, for the area covered by Figure 2.

The analysis of errors suggests the following question: what further changes would have occurred had we been able to check the entire area of each overlay, rather than just the features which crossed the zenith? To consider this, the proportion of the features in the 700m swath that straddle the zenith was determined. It was found that 25% (number, not area) of features crossed the zenith. Thus, the validation dealt with only 25% of the ice features present. 75% remain unvalidated and the changes shown in Table 4 represent only a quarter of the changes that might occur if the entire sidescan image could have been tested against ice thickness profiles. This is not the same as saying that the magnitude of the changes in proportions in Table 4 should be multiplied by four to yield a final correct set of values. But it does suggest that the correct proportions would involve further changes in the same direction as those indicated in Table 4.

The corrected classification was used in the analyses discussed in Sections 6 to 8 below. The next step in our analysis was to digitise the classified sidescan to produce a digital map of the sidescan imagery.

5 GENERATING AND POSITIONING A DIGITAL SIDESCAN MAP

Each individual feature identified on the sidescan (including those verified using upward-looking sonar data) was allocated an identifier consisting of two letters followed by an identification number. The first letter was used to identify the feature type (r,f,m,l,w or u) followed by the second letter which could either be the same as the first for features entirely within the swath width, or 'e' for shapes which cross the swath edge. For example rr130, fe23, ww29. The result of this was a series of 86 hand-drawn classification maps showing individual ice features.



The classified features were then digitised manually as a series of x,y co-ordinates via a Kontron MOP digitising unit. In addition to feature outlines, the digitising unit outputs various statistics for each closed shape. These include area, perimeter and orientation of the major axis. The digitised images correspond to a track length of around 140km. Each of these images were displayed, plotted and compared with the original classification maps to ensure accuracy.

The submarine that collected the sidescan data did not travel at a constant speed, and sidescan sonar chart speed was not lineked automatically to submarine speed. Chart speed changes were input mauually. Thus, while the across-track scale of the imagery is constant, the along-track scaling is not. Therefore, it is not possible to place any feature or features precisely in space, without recourse to other data.

Here, we have placed the sidescan features by tying the sidescan absolutely at 40 points to coincident X-band airborne synthetic aperture radar (SAR) imagery, collected as part of the same exercise (COMISO et al. 1990). Certain groups of features were identifiable on both data sets and these were used to position the sidescan to within approximately 16m, at each of the 40 tie points. Converting the numbers of SAR pixels between successive tie points to distances and comparing with the physical distance in millimetres between the tie points on the sidescan image, enabled scaling factors to be calculated for each of 39 sections. In addition to this, each image was rotated and translated so as to give a consistent set of x,y values. Then, the images were re-scaled, individually to minimise rounding errors. Unfortunately, the SAR data did not cover the first six sections and it was not possible to identify tie points unambiguously in the next six sections. Hence, co-location with the SAR data was only possible for 74 of the small sections, corresponding to a distance of around 119km. Between successive pairs of these tie points, a constant sub speed/chart speed ratio was assumed and the digital sidescan record adjusted by 'stretching' or 'squashing' the digitised data. In this way, we have achieved the best



possible location of the sidescan, without being unduly biased by subjective matching of SAR and sidescan features. The digitised sidescan record was used to generate areal statistics of the ice types and features studied.

6 STATISTICAL PROPERTIES OF THE ICE COVER

6.1 Areal fractions of sea ice types

Table 5 shows the verified areal percentages of the various ice types seen from beneath the ice as well as statistics of feature size. Because the SAR imagery could provide only a limited view of the ice surface in terms of ice type, the information provided by the submarine data is vital for detailed analysis of the area. These data confirm that the region studied was intensely deformed, resulting in a high proportion of small scale ridging and rubble fields which cannot be seen as belonging uniquely to any of the 'classical' sea ice types. Also, previous deformation events resulted, by spring, in a relatively small areal fraction of undeformed first year ice and leads.

We see that approximately 50% of the total area of the sidescan imagery comprises matrix. It is likely that there is no valid way to split this region into other ice types. Certainly no method is immediately obvious, save re-analysing the original imagery to extract progressively smaller homogeneous units, such as linear ridges. At the time of the data collection in May 1987, the study region was clearly not made up of a simple mix of clearly defined floes, leads and ridges but was predominately heavily deformed.

Of the area not defined as matrix, the area of clear multi-year ice (30% of the total) is twice that of clear linear ridges (15% of the total). First year and lead fractions comprise less than 2% and 3% of the total area, respectively.

The statistics presented suggest that the distributions of feature sizes are not Gaussian. Indeed, frequency

distributions for most of the feature size and shape parameters studied (area, Ferret diameter, perimeter length; not shown) are highly positively skewed, both for features contained within the swath width and for edge features. The exception is form factor, which is a measure of the linearity, or alternatively, the 'roundness' of a feature and which was normally distributed. (Form factors close to 0 indicate long, thin features, whereas those closer to 1 evidence progressively more circular features). It is important to bear in mind that the samples of features analysed are all limited at both ends of their size ranges, at the lower end by the limit for rapid analysis and at the upper end by the width of the sidescan swath

6.2 Positional associations between ice types

Familiarity with the appearance of Arctic ice fields suggests to most observers that ice elements do not occur in random sequence but that particular types of element tend to be juxtaposed. A clear case is ridges and leads: larger frozen leads often have pressure ridges beside them which are generated by repeated partial closure and re-opening of the lead during its history. So we might expect leads to be preferentially associated with pressure ridges, although the reverse would not necessarily be the case. Similarly, one might suppose that a different frequency of pressure ridging occurs in first year ice than in multi-year ice.

To test such hypotheses quantitatively, two sequences of ice categories were considered, along lines parallel to the zenith and offset from it by 100m to each side. (This can be done along any other suitable line, between -350m and +350m.) The choice of lines avoided difficulties associated with the centre line and the occasional lack of continuity of features across it, as well as the lower contrast seen there. Two transects of the sidescan swath were studied to enable a qualitative assessment of the stability of the resulting statistics. 100m offsets were chosen to maximise the quality of the data in the area of swath with the clearest image and to be as close to the



zenith as possible so as to be within the area of the swath corrected using the upward-looking sonar. Whilst each transect represents a separate trial of the population, the size of some features means that the two trials are not independent.

The analysis considers the distribution of ice of 'Type I' in relation to another type, 'Type II'. By definition, matrix is not present in sequential lists of features, so the data were analysed to identify the regions along these lines where there existed gaps between features of greater than 15m. At each of these points, a feature of type matrix (Mx) was added. The threshold of 15m was chosen after consideration of digitising accuracy and examination of a frequency histogram of the gaps between features. This procedure was checked by hand to ensure that matrix was correctly inserted between defined features. The resulting primary data sets were two sequences of features, along track for approximately 119km (for example: r,r,m,r,Mx,m,l,f,l,w,r,m,r,Mx,r,r,m,m,.....).

Note that, by definition two matrix features cannot be adjacent but other similar types may. Because of the physical ambiguity in identifying leads, for the analysis discussed below l and w are combined into one class of leads, L.

The resulting sequences were tested to see if features of a certain type (Type 'I') are more or less likely to be associated with features of another type (Type 'II') than could be accounted for if the sequences of features were random. By treating each individual feature as a bin and selecting a feature Type I, the number of bins adjacent to features of Type I (and not containing another I) were counted. These were denoted as 'special' bins. All other non-I bins were denoted 'normal' bins. For each transect, the number of special bins was less than twice the number of normal bins because of cases where two or more features of Type I lie alongside one another, or where two Type I features are separated by a single feature of another type.

The hypothesis under test was that a feature of Type II would be equally likely to lie in a normal bin (away from a Type I feature) as a special bin (next to a Type I

feature). On the other hand, if Type II elements are significantly more likely to be found in special bins than in normal bins, then we can say that there is a positive positional association between Type II and Type I. The statistical test is a simple 2x2 contingency table from which the χ^2 statistic (with one degree of freedom) is computed, using an equation corrected for continuity (SIEGEL, 1956). The results of our initial analysis are shown in Tables 6a and 6b.

The tables show, for all possible Type I:Type II pairs, the number of features of Type I; the number of special bins for that particular Type I; the number of features of Type II in special bins; the number of normal bins and the number of features of Type II in normal bins; the sign of the association and the calculated χ^2 . Note that when an expected number of associations is zero, no χ^2 statistic is calculated. Relevant significance levels are:

0.05 significance level $\chi^2 \leq 3.84$

0.01 significance level $\chi^2 \leq 6.64$

However, since we would expect that, by chance, 1% of the listed 32 tests would show a significant result at the 0.01 level (0.32 tests), we suggest that a more rigorous test of significance be applied. The 0.00032 significance level ($\chi^2 \leq 12.95$) seems appropriate, since this is 1% of 0.32.

Tables 6a and b show some clear associations that are not surprising. For example l:w and w:l should be strongly positively associated and these data show them to be so, at χ^2 of 84.25 and 81.98, respectively for Transect 1 and similarly high values for Transect 2.

Leads of either type are strongly negatively associated with ridges (r:L - Transect 1, $\chi^2=42.14$; Transect 2, $\chi^2=31.30$), with a less strong negative association the other way (L:r - $\chi^2=7.07$ and 6.08, respectively). This is an important result, as it seems to refute the impression of experienced observers. Leads are distributed through the sea ice field so as to be significantly less likely to be next to ridges than to be away from ridges. This result requires verification and explanation. It suggests perhaps

that opening events are not the same events that build ridges. Alternatively, it may be that in the period just before the data were collected, this area of the sea ice field had experienced only divergence during the events which created the local pattern of leads. Thus, there would have been no cases of partial lead closure that would have built ridges along the edges of leads.

Matrix appears to be associated with ridges (r:Mx - Transect 1, $\chi^2=15.46$; Transect 2, $\chi^2=29.10$) but less strongly the other way (Mx:r - $\chi^2=3.11$ and 6.39, respectively). This is not surprising considering the sea ice environment of the study area and since matrix is defined as a non-linear ridged and hummocked under-side. On the other hand, ridges are not significantly associated with matrix, confirming that the presence of matrix does not necessarily indicate the presence of identifiable linear ridging. Matrix is actually an apparently random array of deformed ice. Frequently within such a matrix it is possible to discriminate a linear ridge feature. Thus, it is reasonable to expect matrices to be situated alongside ridges in a non-random way. Matrix is positively associated with multi-year ice (m:Mx) at or above the 0.01 significance level (matrix is more likely to be situated next to multi-year ice than away from it), which is expected. However, the converse association is not seen. multi-year ice is no more likely to be situated next to matrix than elsewhere in the sea ice field.

Another interesting result is that along Transect 1 leads are significantly not associated with multi-year ice ($\chi^2=13.22$ for m:L). This is not seen as significant along Transect 2 where $\chi^2=2.65$. Assuming that the association is real, it has a clear physical explanation. Multi-year ice floes are stronger than younger, thinner ice. The latter are expected to crack preferentially, under shear or divergence, to form leads. However, the relationship between multi-year ice and leads does not support this conclusion (L:m - $\chi^2=0.62$ (+), Transect 1; $\chi^2=3.99$ (+), Transect 2). Here, there is no apparent preference for multi-year ice not to be associated with leads. Indeed, if anything there is a suggestion of a positive association. Since most of these results are within the limits of random



variation, we conclude that larger spatial data sets are required to study these relationships further and perhaps resolve this ambiguity. In a similar way, while leads are strongly not associated with matrix (Mx:L - $\chi^2=10.53$, Transect 1; $\chi^2=12.96$, Transect 2), there is no such relationship seen for L:Mx. We have no ready explanation for this.

Unsurprisingly, multi-year ice and first year ice appear to be quite strongly not associated (m:f - $\chi^2=11.95$, Transect 1; $\chi^2=10.95$, Transect 2 and f:m - $\chi^2=5.94$ and $\chi^2=4.32$, respectively). Despite the paucity of first year ice in the study area, we accept this result as a confirmation that such a juxtaposition is likely to be unstable, as ridge building will be encouraged at the interface.

Importantly, for this dataset there is no tendency for homogeneous areas of multi-year ice to be positionally related to ridges (r:m - $\chi^2=0.27$, Transect 1; $\chi^2=4.00$, Transect 2 and m:r - $\chi^2=0.05$ and $\chi^2=0.10$, respectively).

6.3 A runs test for sequence data

A run is defined as a succession of identical features which are followed or preceded by features of different types, or no features at all. For example, the sequence:R,R,R,M,M,R,M,....

has a run of three Rs, then a run of two Ms, followed by a run of one R and finally, a run of one M. By counting the number of runs of each feature type and comparing the actual number with the expected number, the hypothesis can be tested that the sequence of like features is randomly distributed along track.

The expected number of runs (MOOD, 1940) for each feature type is given by:

$$E(r_i) = \frac{n_i(n - n_i + 1)}{n} \quad (1)$$

Where: r_i is the number of runs of feature type i
 n_i is the number of features of type i , and
 n is the total number of features.

Here, the distribution of the number of runs is transformed to one with zero mean and unit variance (see MOOD, 1940). If a normal distribution is assumed (which is the asymptotic case), then the 0.01 significance level is at $z=2.33$. Along the same two transects analyses of runs were undertaken. The results are summarised in Table 7.

The results indicate that the distributions of runs are approximately random for all features except ridges and multi-year ice. Both of these show significantly more runs and hence smaller groupings (more regularly spaced features) than would be expected in a random sequence. This does not indicate an association between ridges and multi-year ice. Similarly, it does not indicate that there is a preferred length scale for ridge building and multi-year floe splitting events in the region, prior to data collection. It does show that in this data set, both ridges and multi-year ice fragments tend to come in ones, less often in pairs, triplets or longer groups. For ridges, this suggests that each ridge building event tends to build one ridge, rather than a number of adjacent ridges. If ridges seen by the sidescan sensor tend to be preferentially orientated parallel to the track, rather than normal to it, then a cluster or group of ridges would tend to be seen as one ridge on linescan data (as here or on an upward-looking sonar record), giving a non-random along-track distribution of runs.

Having a number of multi-year fragments adjacent is only possible if they are separated by the thinnest of cracks (not delineated as separate features during classification). Thus, we expect that there would be a tendency towards separation of multi-year ice floes and hence a non-random distribution along track. Unfortunately the numbers of leads and first year ice fragments in the data set are too few for us to draw any conclusions from the results.

7 ANALYSIS OF LEADS

7.1 Distribution of lead orientations

A manual analysis was carried out of every lead which crossed the centre line of the sidescan swath. For this purpose 'Bright' and 'Dark' leads were combined. The average orientation of the lead within the image width was measured, with the resulting angle being expressed as rotation anticlockwise relative to an east-west axis (the submarine was heading eastward). The position of the western edge of the lead when it crossed the centre line was recorded. The width of the lead at right angles to its major axis was measured at uniform (68.5m) intervals along the axis, giving typically ten to twelve independent measurements of width for each lead.

Figure 4 shows the distribution of orientations of the 38 leads occurring in the original 140km sample of classified sidescan. If leads were truly random in orientation and had lengths which were independent of their orientation, then the frequency of encounter with a lead along any given straight line would be proportional to $\sin\theta$, where θ is the angle between the lead axis and the line. Such a random distribution is also plotted in Figure 4. It can be seen that the observed distribution appears to differ considerably from randomness, although a χ^2 goodness-of-fit shows that this difference is not significant ($\chi^2=25.1$ for 16 degrees of freedom). The distribution is strongly peaked in the range 60° - 70° , relative to north, indicating a preferred northeast to southwest orientation for leads in this region. The distribution also has a lower variance

than would a random distribution. Since we do not expect the detectability of leads to be dependent on orientation (unlike ridges), we conclude that there is some evidence of a non-randomness to the lead orientation distribution, indicating a preferred direction for leads within the length scale of 140km.

To investigate this effect further, the way in which lead orientations varied with distance along track was examined. Figure 5 shows the orientation of each lead plotted against the along track distance at which the lead crossed the centre line, in kilometres. Leads wider than 100m are shown with a circle, narrower ones by a dot. Figure 5 indicates both clustering and a trend. The leads are not widely scattered in orientation but are clustered around what appears to be a linear trend, with θ decreasing along the track. The best-fit regression line through the data is also shown on Figure 5. This is evidence that the stress system which gave rise to the leads was slowly changing in direction but had a 'wavelength' greater than the 140km length of track. Figure 5 also indicates a tendency for leads to become less frequent with increasing along track distance, showing that the sea ice field may have been less divergent in the eastern part of the study area.

7.2 Distribution of lead widths

The dataset of 38 independent leads yielded a distribution of mean widths (as measured along a grid of positions as described above) shown in Table 8. The overall mean width was 79.4m and median width 35.3m. The small number of leads in the sample makes it impossible to test this dataset for its fit to a functional form. However, the dataset is of unique quality because all other published lead width distributions (for example, WADHAMS and HORNE, 1980; WADHAMS, 1981) consist of projected along track lead widths derived from upward-looking sonar data, rather than real widths measured at right angles to the lead axis, along a significant length of that axis.

Table 9 compares the exceedence frequency of these data with two other published datasets, from the Beaufort Sea in



April 1976 (USS 'Gurnard', WADHAMS and HORNE, 1980) and M'Clure Strait in February 1960 (USS 'Sargo', MCLAREN, WADHAMS and WEINTRAUB, 1984). Our results are remarkably similar to the 'Sargo' distribution and not dissimilar to the 'Gurnard' results. The chief difference lies in the lower frequency of narrow leads (less than 50m wide) detected by the sidescan sonar. This is possibly an artefact of the classification technique, in that narrow cracks with little or no apparent width were often incorporated into the floe of which they formed part, whereas on an upward-looking sonar record they would be detected and recorded as separate entities.

The similarities among these three datasets strongly suggest that there is some natural function governing the width distribution of leads, applicable throughout the Arctic (at least in winter and spring). However, larger datasets would need to be examined in order to verify this and establish its nature. WADHAMS (1981) found a power law for lead widths (with frequency proportional to width⁻²) but this has not been confirmed in other datasets. A best power law fit to the present data gives an exponent of -1.74 but the sample size is small and thus the significance of this result is not known.

7.3 Lead spacings

If leads are placed randomly upon an ice surface, the distribution of spacings between successive leads along a given line should be a negative exponential. The relationship was proposed for the equivalent case of pressure ridges by HIBLER, WEEKS and MOCK (1972) and confirmed by WADHAMS (1981), although in a later analysis it was found that the log-normal distribution gives a better fit to ridge spacing data (WADHAMS and DAVY, 1986).

The 38 leads in this sample have a spacing distribution which differs greatly from randomness. As Table 10 shows, the distribution is strongly peaked in the range two to three kilometres. Physically, this result suggests that the lead system in this region was created by a single stress event, represented by a slowly varying stress field of high spatial coherence (hence the preferred



orientations) and of fairly uniform magnitude. It seems that there was a preferred distance over which a single lead-opening event is capable of relieving the stress upon the sea ice field.

8 ANALYSIS OF PRESSURE RIDGE KEEL DATA

8.1 Ridge orientations

Information on ridge orientation is important since any directional anisotropy in sea ice roughness parameters would lead to a corresponding anisotropy in the mean strength of the ice cover, its drag coefficient, its ability to generate internal waves and the rate of transmission loss for sound under ice. Using the digital sidescan dataset such data can be derived with confidence for the first time. Since the crest line of each ridge was placed on the overlays of sidescan classification, it was possible to compute the orientations of pressure ridges which cut any given line. Here, two lines were chosen; the centre line of the sidescan swath and a line offset by 100m. The datasets are not independent but each represents a separate unbiased trial of the orientation distribution. 173 ridges were observed along the centre line and 420 along the 100m offset, an indication of the data quality problems at zenith. The distributions of orientations along these transects are shown plotted in 10° bins as Figure 6 together with the frequency distribution of all ridge orientations derived for all 1378 ridges in the entire digital sidescan map (86 images).

Figure 6 shows that centre line orientations are strongly peaked relative to the sine curve which would occur for a random distribution, with a main peak in the 60° - 80° range, similar to the result of the lead analysis. The 100m offset orientations are also peaked at 60° - 80° but with a smaller deviation from randomness. We suspect that the ridges along the centre line are subject to data quality and detectability problems as already described and the smaller number implies that they are a selected group. Thus, the 100m offset distribution is considered to be more representative of the data set as a whole. It appears not

to differ significantly from a random distribution, except for the peak at 60° - 80° . This peak is evidence of a preferred ridge orientation to match the preferred lead orientation.

However, this result is derived using ridges encountered along a single line, sampling relatively few of all the ridges present in the complete sidescan data set. Because the orientations of all identified ridges were output as a product of the classification and digitising procedure, it is possible to consider a larger set of ridge orientations (θ), determined relative to the direction of movement (eastward). Figure 6 also shows the frequency of all ridge 1378 orientations in the record. The frequency distribution appears quite uniform but with a tendency to dip in the centre, near $\pi/2$. If ridges were randomly orientated in space, we would expect to see a uniform distribution on the sidescan image so long as the swath is wide enough to make the image truly two-dimensional, that is relatively few ridges with cross-track lengths greater than 700m. As this was not quite the case, the theoretical random distribution should lie between the ($\sin\theta$) relationship of Figure 4 and uniformity. Folding the distribution in half so that its limits are 0 and $\pi/2$ (Figure 7) indicates a noticeable reduction in sidescan detectability of ridges as the ridge orientations approach $\pi/2$ (ie. normal to the submarine track). This is expected since the shadows produced by such a ridge are just the relief shadows of individual blocks, whereas for a ridge parallel to the track, the entire ridge casts an acoustic shadow on the undeformed ice behind it. Finally, we find no relationship between ridge size and orientation.

8.2 Ridge spacing

The frequency distribution of ridge spacing is shown in Figure 8, for a 100m offset sample. Spacings were defined as the distances between crossings of the relevant line by the leading (western) edge of successive ridges. Figure 8 indicates an apparently reasonable fit to a negative exponential distribution, except for ridge spacing less than 150m. A log-normal distribution provides a better fit, as observed for Arctic sea ice ridges (WADHAMS and

DAVY, 1986). The best fit to a log-normal distribution is that the cumulative probability versus ridge spacing should fit a straight line when plotted on logarithmic probability paper. Cumulative distributions are plotted in Figure 9 together with the equivalent centre line data. Here the 100m offset results show a good fit to a log-normal distribution, while the centre line data fit less well.

To verify these results, the positions of leading edges of ridges along the two 100m offset lines (Transects 1 and 2) were computed. In each case, the along track distance was split into 100m bins and the number of ridges that started in each bin were counted. No account was taken of ridge orientation, so that ridges crossing the transects that were nearly parallel to the submarine track would be much longer than others (and would be more likely to cross bin boundaries than those at right angles). Bearing this in mind, if the (leading edges of) ridges identified along track were randomly spaced, with a negative exponential distribution of spacing, then the frequency distribution of number per bin would be expected to fit a Poisson distribution. Figure 10 shows the comparison between the actual distribution of ridge starts per bin and the corresponding Poisson distribution for Transect 1 data (the almost identical distribution for Transect 2 are not shown). By eye this confirms that ridges are randomly spaced along the track and thus that there was no obvious length scale of ridge building events in the study region or upstream of it, prior to data collection.

9 CONCLUSIONS

Sidescan sonar imagery provides the first opportunity to carry out spatial analysis of the structural elements which comprise the main volume of a sea ice field that may be viewed from the underside. A manual division of the sidescan images into identifiable structural elements was tested against upward-looking sonar profiles. The classification procedure was found to be reliable for positive identifications of ridges and multi-year ice but not for first year ice. It was not possible to identify all the ridges present using sidescan sonar.



An analysis of 140 km of sidescan sonar swath separated into ice type categories showed that there were a number of significantly non-random juxtapositions of different ice elements, implying a degree of association between them. An unexpected result was that leads are significantly less likely to be situated next to ridges than randomly along track. Lead orientations were non-random, being concentrated within a narrow band of angles in a generally NE-SW orientation. This preferred orientation changes slowly along the length of the sample, implying a causative stress mechanism with a characteristic length scale exceeding 140km. Lead widths did not fit a simple distribution but did agree well with earlier measurements made in the Arctic in winter. Spacings between successive leads were not random but had significant clustering in the range 2 to 3 km.

Analysis of the pressure ridge orientations showed they did not differ greatly from randomness, but possibly have a similar orientation to the leads. The spacings of pressure ridges offer a good fit to a log-normal distribution.

In all of these analyses, a distinctive characteristic of the ice cover was the extent of apparently random fields of broken-up ice blocks on the underside, so random that individual linear ridges could not be distinguished among them. This is in contrast to the greater rarity of such rubble fields as reported from the analysis of SAR for the ice upper surface.

ACKNOWLEDGEMENTS

This work was carried out for the U.S. Office of Naval Research, NASA and the U.S Office of the Naval Oceanographer, under Office of Naval Research Contract No. N00014-89-C-0014 to Science Applications International Corporation, Polar Oceans Associates Division, Cambridge, UK. We are grateful for the support and suggestions of these funding agencies. The authors acknowledge the help of SAIC staff for sidescan interpretation (Alison Scoon), data analysis (Mark Fearon) and support (David Evans).

REFERENCES

BERKSON, J.M., C.S. CLAY and T.K. KAN (1973) Mapping the underside of Arctic sea ice by backscattered sound. Journal Acoustic Society America, 53(3), 771-781.

COMISO, J. C., P. WADHAMS, W.B. KRABILL, R.N. SWIFT, J.P. CRAWFORD and W.B. TUCKER III (1990) Top/bottom multisensor remote sensing of Arctic sea ice. Submitted to: Journal Geophysical Research.

GUOLIANG, J. and P. WADHAMS (1989) Travel time changes in a tomography array caused by a sea ice cover. Progress in Oceanography, 23, 249-275.

HIBLER, W.D. III, W.F. WEEKS and S.J. MOCK (1972) Statistical aspects of sea ice ridge distributions. Journal Geophysical Research, 77, 5954-5970.

KAN, T.K., C.S. CLAY and J.M. BERKSON (1974) Sonar mapping of the underside of sea ice. Journal Geophysical Research, 79(3), 483-488.

MCLAREN, A.S., P. WADHAMS and R. WEINTRAUB (1984) The sea ice topography of M'Clure Strait in winter and summer of 1960 from submarine profiles. Arctic, 37(2), 110-120.

MOOD, A.M. (1940) The Distribution Theory Of Runs. Annals of Mathethmatical Statistics, 11, p367-392.

ROTHROCK, D.A. and A.S. THORNDIKE (1980) Geometric properties of the under side of sea ice. Journal Geophysical Research, 85, 3955-3963.

SIEGEL, S. (1956) Nonparametric Statistics For The Behavioral Sciences. 312pp.

TUCKER, M.J. and A.R. STUBBS (1961) A narrow-beam echo-ranger for fishery and geological investigations. British Journal Applied Physics, 12, 103-110.



WADHAMS, P. (1978) Sidescan sonar imagery of sea ice in the Arctic Ocean. Canadian Journal Remote Sensing, 4(2), 161-173.

WADHAMS, P. (1981) Sea-ice topography of the Arctic Ocean in the region 70°W to 25°E. Philosophical Transactions Royal Society London, A302(1464), 45-85.

WADHAMS, P. (1983). Arctic sea ice morphology and its measurement. Journal Society of Underwater Technology, 9(2), 1-12.

WADHAMS, P. (1988) The underside of Arctic sea ice imaged by sidescan sonar. Nature, London, 333, 161-164.

WADHAMS, P and T. DAVY (1986) On the spacing and draft distributions for pressure ridge keels. Journal Geophysical Research, 91(C9), 10697-10708.

WADHAMS, P. and R.J. HORNE (1980) An analysis of ice profiles obtained by submarine sonar in the Beaufort Sea. Journal Glaciology, 25(93), 401-424.

WADHAMS, P., J.C. COMISO, J. CRAWFORD, G. JACKSON, W. KRABILL, R. KUTZ, C.B. SEAR, R. SWIFT, W.B. TUCKER and N.R. DAVIS (1990) Concurrent remote sensing of Arctic sea ice from submarine and aircraft. International Journal Remote Sensing, in press.

Table Captions

Table 1. Comparison of ice type classifications from sidescan sonar and upward-looking sonar data with likely ice draught ranges.

Table 2. Success and failure rates of classification of ice types on sidescan sonar images by validating using upward-looking sonar data, for 140km of sidescan imagery.

Table 3. Success and failure rates of classification of ice types on sidescan sonar images by validating using upward-looking sonar data. Tabulation of new ice features added after correction of erroneous identifications.

Table 4. Original and revised total numbers of features, by class, identified in the central portion of the sidescan sonar record.

Table 5. Ice type statistics.

Table 6. The association of features in sequence along track. Chi-square Test results. \pm indicates the sign of the association. Emboldened χ^2 values are significant at the 0.00032 significance level and underlined values are significant at a less stringent 0.01 significance level ($\chi^2 \leq 12.95$)

a) Transect 1, b) Transect 2

Table 7. Results of an along track Runs Test for features of like sea ice type. Note that, by definition, two or more areas of matrix can be adjacent. Nether can two or more leads of type L (l + w). Significance at the 0.01 significance level is indicated by emboldening.

Table 8. Distribution of mean lead widths in the 140km along track sample of 700m width sidescan sonar data.



Table 9. Lead width exceedence frequencies from this sidescan sonar derived data set, compared with two previous data sets, derived from upward-looking sonar. Mean distances between encounters with a lead of width at least W metres are tabulated.

Table 10. Distribution of lead spacing in the 140km sidescan sonar data set.

Ice Type	sidescan Classification	upward-looking sonar Classification	Draught Range (m)
i. Ridge (r)	Linear, strong backscatter / dark shadow. Clear crest line	Defined by Rayleigh criterion (eg. WADHAMS and DAVY, 1986)	$r > 5m$
ii. First year (f)	Smooth underside with narrow cracks	Smooth bottom (bottom slope $< 5\%$)	$1 < f < 2.5$
iii. Multi-year (floes) (m)	Less smooth or rugged with bulges	High mean draught, a bumpy relief with bulges	$2.5 < m < 4m$ Bulges $< 1m$
iv. 'Bright' lead L1 (l)	Linear, smooth, weak return	Thin level ice. Smooth bottom (slope $< 5\%$)	$l < 1m$
v. 'Dark' lead L2 (w)	Linear, smooth, strong return, maybe banded	Thin level ice or open water (slope $< 5\%$)	$w < 1m$
vi. Unclassified (u)	Poor return	-	-
vii. Matrix (Mx)	Non-linear ridges and rubble field, hummocky	Rough ice (bottom surface slope not always less than 5%)	$Mx > 2.5m$

Table 1. Comparison of ice type classifications from sidescan sonar and upward-looking sonar data with likely ice draught ranges.



Ice Type	Correct IDs		Erroneous IDs		Total Number	%
	Number	%	Number	%		
Mx	196	72.1	76	27.9	272	35.5
m	233	86.6	36	13.4	269	35.1
f	12	34.3	23	65.7	35	4.6
r	116	96.7	4	3.3	120	15.7
l	19	73.1	7	26.9	26	3.4
w	19	52.8	17	47.2	36	4.7
u	1	11.1	8	88.9	9	1.2
Total	596	77.7	171	22.3	767	100.0

Table 2. Success and failure rates of classification of ice types on sidescan sonar images by validating using upward-looking sonar data, for 140km of sidescan imagery.



Added Class	Original Category							Total
	Mx	m	f	r	l	w	u	
Mx	53	7	2	1	0	0	3	66
m	40	26	17	0	1	0	2	86
f	5	12	1	0	1	0	0	19
r	70	19	2	0	0	12	6	109
l	2	0	3	2	1	3	1	12
w	4	0	1	0	6	0	0	11
u	0	0	0	0	0	0	0	0
Total	174	64	26	3	9	15	12	303

Table 3. Success and failure rates of classification of ice types on sidescan sonar images by validating using upward-looking sonar data. Tabulation of new ice features added after correction of erroneous identifications.



Ice Type	Original ID		Corrected ID	
	Number	%	Number	%
Mx	272	35.5	262	29.2
m	269	35.1	319	35.5
f	35	4.6	31	3.4
r	120	15.6	225	25.1
l	26	3.4	31	3.4
w	36	4.6	30	3.3
u	9	1.2	1	0.1
Total	767	100	899	100

Table 4. Original and revised total numbers of features, by class, identified in the central portion of the sidescan sonar record.

Ice Type	Number		Total Area (10^6 m^2)	Areal Fraction	Areal Statistics (10^3 m^2)*		
	Within Swath	Total			Mean	Median	St.Dev
l	12	37	1.4	1.9	13.0	8.6	10.4
w	53	71	0.8	1.1	8.5	4.7	11.0
f	41	67	1.4	1.8	9.1	7.0	10.2
m	589	811	22.7	29.7	18.1	9.8	24.3
r	1285	1378	11.2	14.7	7.7	5.9	6.4
Hx	-	-	37.8	49.7	-	-	-
u	4	33	1.1	1.1	4.8	3.7	4.0
Total	1984	2397	76.4	100.0	-	-	-

* For features entirely within the swath width (ie. not edge features)

Table 5. Ice type statistics.



A:B	N _A	N _{spec}	N _B in spec	N _{norm}	N _B in norm	±	χ ²
r:m	420	511	215	239	95	+	0.27
r:f	420	511	10	239	10	-	2.31
r:l	420	511	21	239	45	-	42.14
r:u	420	511	0	239	1		-
r:Mx	420	511	264	239	86	+	15.46
m:r	310	477	235	383	185	+	0.05
m:f	310	477	3	383	17	-	11.95
m:l	310	477	22	383	44	-	13.22
m:u	310	477	1	383	0		-
m:Mx	310	477	215	383	135	+	8.09
f:r	20	37	12	1113	408	-	0.12
f:m	20	37	3	1113	307	-	5.94
f:l	20	37	7	1113	59	+	9.89
f:u	20	37	0	1113	1	-	
f:Mx	20	37	15	1113	335	+	1.38
l:r	66	90	22	1014	398	-	7.07
l:m	66	90	29	1014	281	+	0.62
l:f	66	90	5	1014	15	+	5.60
l:u	66	90	1	1014	0		-
l:Mx	66	90	33	1014	317	+	0.88
u:r	1	2	0	1167	420		-
u:m	1	2	1	1167	309		0.00
u:f	1	2	0	1167	20		-
u:l	1	2	1	1167	65	+	1.41
u:Mx	1	2	0	1167	350		-
Mx:r	350	518	278	302	142	+	3.11
Mx:m	350	518	200	302	110	+	0.30
Mx:f	350	518	11	302	9	-	0.28
Mx:l	350	518	29	302	37	-	10.53
Mx:u	350	518	0	302	1		-
l:w	23	41	13	1106	30	+	84.25
w:l	43	78	13	1049	10	+	81.98

Table 6. The Association of features in sequence along track. Chi-square Test results. \pm indicates the sign of the association. Emboldened χ^2 values are significant at the 0.00032 significance level and underlined values are significant at a less stringent 0.01 significance level ($\chi^2 \leq 12.95$).



A:B	N _A	N _{spec}	N _B in spec	N _{norm}	N _B in norm	±	χ ²
r:m	343	418	150	209	93	+	4.00
r:f	343	418	11	209	8	-	0.33
r:l	343	418	18	209	38	-	31.30
r:u	343	418	2	209	0		0.06
r:Mx	343	418	237	209	70	+	29.10
m:r	243	368	171	359	172	+	0.10
m:f	243	368	2	359	17	-	10.95
m:l	243	368	22	359	34	-	2.65
m:u	243	368	0	359	2		0.53
m:Mx	243	368	173	359	134	-	6.60
f:r	19	34	15	917	328	-	0.66
f:m	19	34	3	917	240	-	4.32
f:l	19	34	2	917	54	+	0.14
f:u	19	34	0	917	2	-	2.67
f:Mx	19	34	14	917	293	+	0.89
L:r	56	90	19	835	324	-	6.08
L:m	56	90	29	835	214	+	3.99
L:f	56	79	2	835	17	+	0.01
L:u	56	79	0	835	2		0.68
L:Mx	56	79	29	835	278	+	0.24
u:r	2	4	3	964	240		1.29
u:m	2	4	0	964	243		0.34
u:f	2	4	0	964	19		2.32
u:l	2	4	0	964	56	+	0.33
u:Mx	2	4	1	964	306		0.06
Mx:r	307	435	241	228	102	+	6.39
Mx:m	307	435	158	228	85	+	0.03
Mx:f	307	435	11	228	8	-	0.22
Mx:l	307	435	24	228	32	-	12.96
Mx:u	307	435	1	228	1		0.08
L:w	17	31	12	922	27	+	88.93
w:l	39	72	12	859	5	+	87.11



Table 6b

Type	Number of Runs	n_i	$E(r)$	σ^2	σ	z
r	353	420	269	62	7.9	10.6
m	299	310	228	44	0.6	10.8
f	19	20	20	0.3	0.5	2
l	22	23	23	0.4	0.6	1.7
w	43	43	41	1.4	1.2	1.7
u	1	1	1	0	0	0

Table 7. Results of an along track Runs Test for features of like sea ice type. Note that, by definition, two or more areas of matrix can be adjacent. Neither can two or more leads of type L ($l + w$). Significance at the 0.01 significance level is indicated by emboldening.

Table 7b

Type	Number of Runs	n_i	$E(r)$	σ^2	σ	z
r	291	343	222	51	7.1	9.7
m	230	243	182	34	5.8	8.2
f	18	19	19	0.4	0.6	-1.1
l	16	17	17	0.3	0.5	-1.4
w	38	39	37	1.4	1.2	0.4
u	2	2	2	0.0	0.0	0.0

Lead Width (m)	Number of Leads
Mean 79.4m Median 35.3m	
1 - 20	12
21 - 40	8
41 - 60	6
61 - 80	2
81 - 100	0
1 - 100	28
101 - 200	6
201 - 300	2
301 - 400	1
401 - 500	0
501 - 600	1

Table 8. Distribution of mean lead widths in the 140km along track sample of 700m width sidescan sonar data.

Minimum Lead Width (W)	Mean distance (km)		
	These data North of Greenland (May 1987)	'Sargo' M'Clure Strait (Feb. 1960)	'Gurnard' Beaufort Sea (Apr. 1976)
0	3.0	1.3	0.2
50	7.2	7.4	10.3
100	11.4	12.2	24.1
150	19.1	18.9	38.4
200	28.6	25.0	67.6
500	114	100	237

Table 9. Lead width exceedence frequencies from this sidescan sonar derived data set, compared with two previous data sets, derived from upward-looking sonar. Mean distances between encounters with a lead of width at least W metres are tabulated.

Lead Spacing (km)	Number
0 - 1	8
1 - 2	6
2 - 3	14
3 - 4	3
4 - 5	1
5 - 6	1
6 - 7	0
7 - 8	0
8 - 9	0
9 - 10	2
10 - 11	0
11 - 12	1
12 - 13	0
13 - 14	0
14 - 15	0
15 - 16	1

Table 10. Distribution of lead spacing in the 140km
sidescan sonar data set.

Figure Captions.

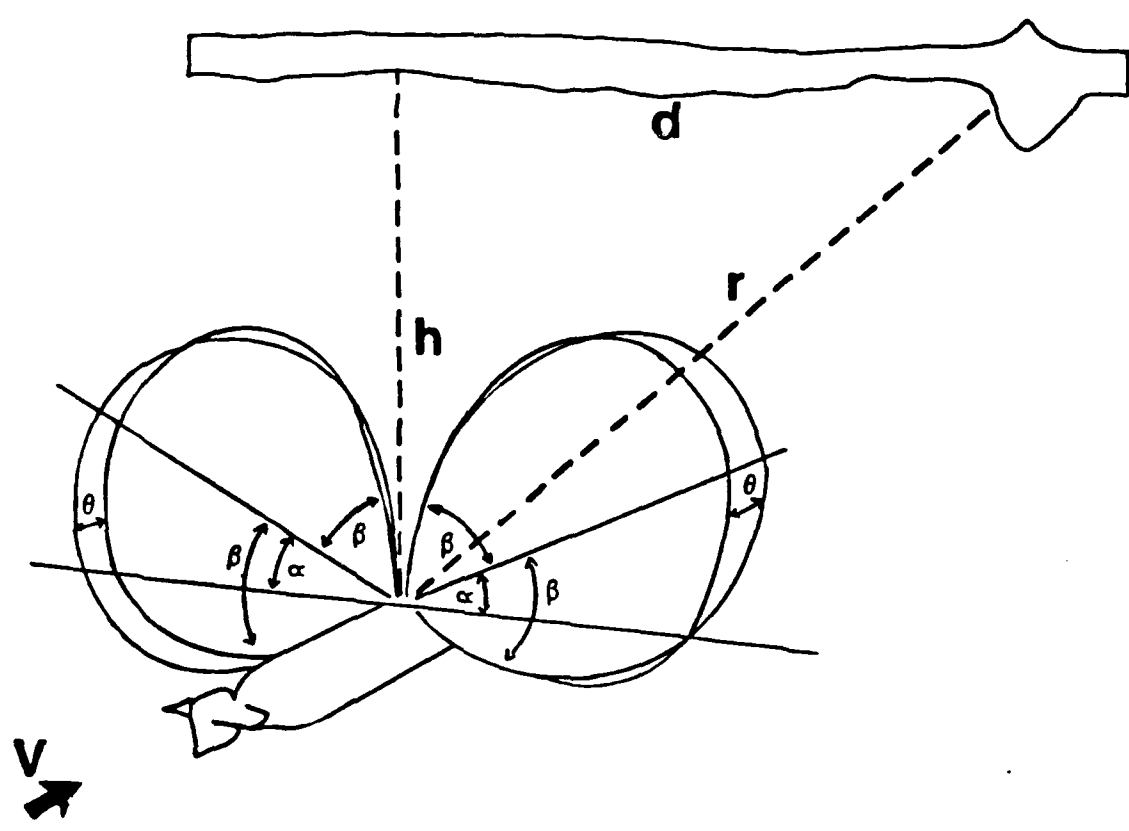
- Figure 1. Geometry of sidescan sonar under-ice profiling.
- Figure 2. Photograph of a portion of the original sidescan sonar chart roll.
- Figure 3. Portion of classified sidescan showing features f: first year ice, m: multi-year ice, r: ridge, l: lead L1, w: lead L2.
- Figure 4. Lead orientation frequency distribution with $\sin\theta$ distribution also shown.
- Figure 5. Lead orientations by distance with regression line. Leads wider than 100m shown as circles.
- Figure 6. Ridge orientations for centre line and 100m offset ridges.
- Figure 7. Ridge orientations for all ridges.

Figure 8. Ridge orientations distribution folded in half. All ridges.

Figure 9. Frequency histogram of ridge spacing along a transect 100m offset from the centre line of the sidescan swath for spacings less than 1000m. Also shown is the best fit to a negative exponential distribution.

Figure 10. Cumulative probability plot of ridge spacings.

Figure 11. Frequency histogram of ridge starts in 100m bins along track. Also shown is the expected Poisson distribution.

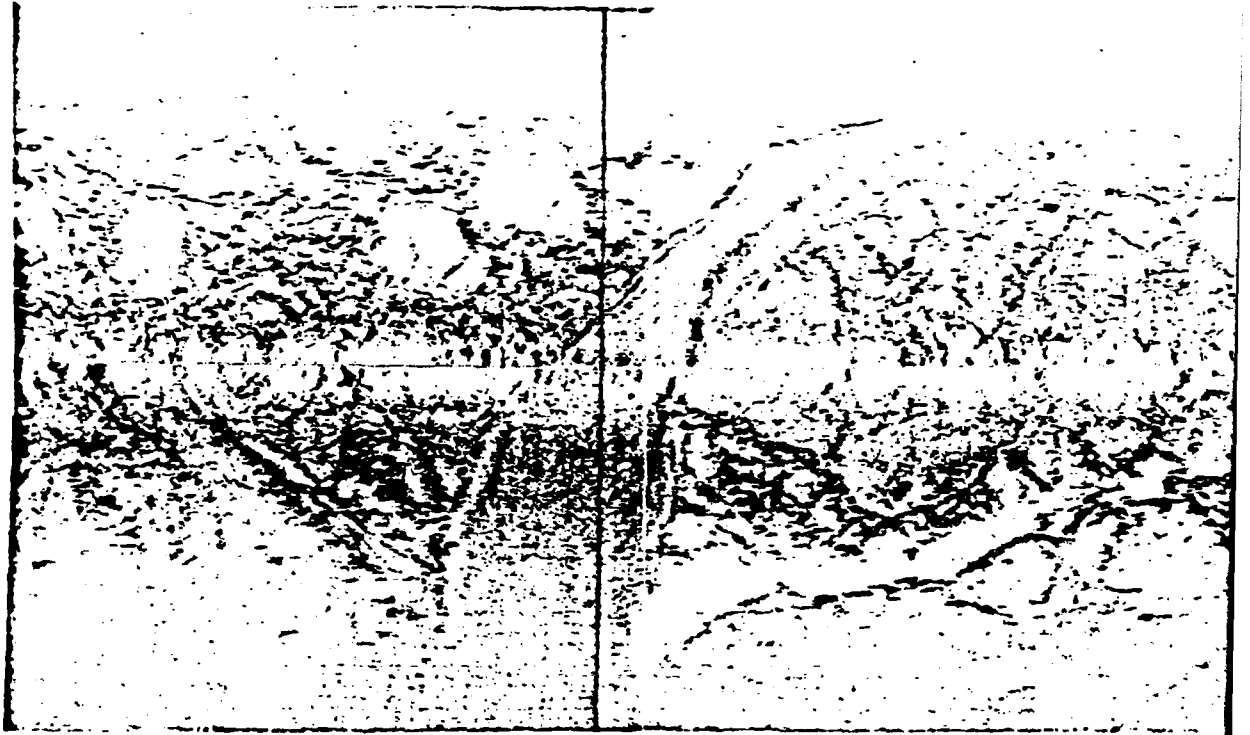


Key

Vertical beamwidth	= 2β
Azimuthal beamwidth	= θ
Depression angle	= α
Depth from surface to transducer	= h
Range	= r
Lateral distance	= d
Boat speed	= V

Figure 1 Geometry of sidescan sonar under-ice profiling

figure 2



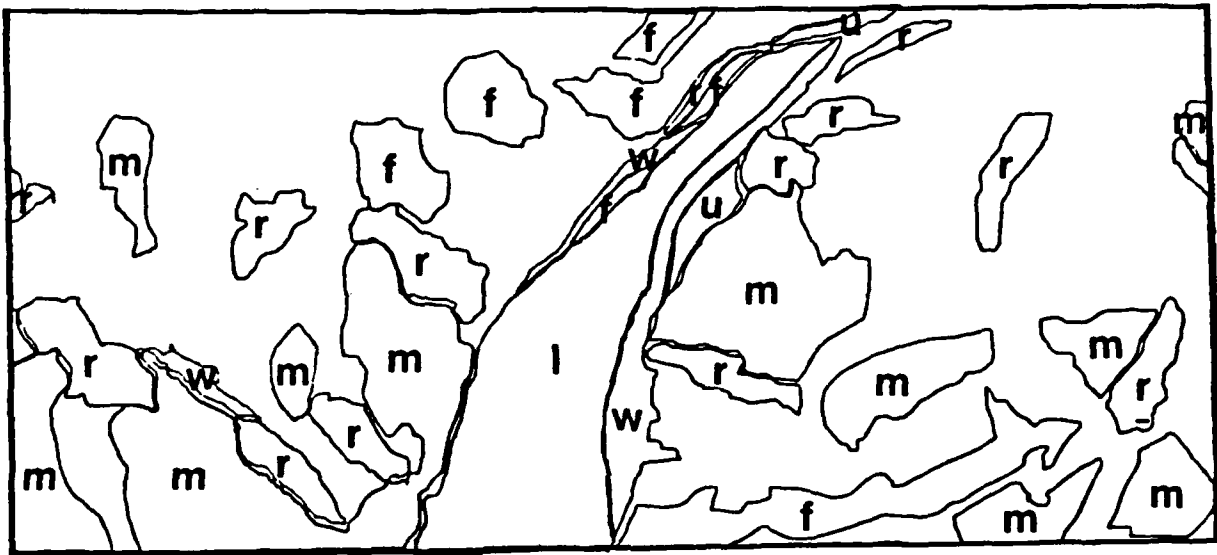


Figure 4

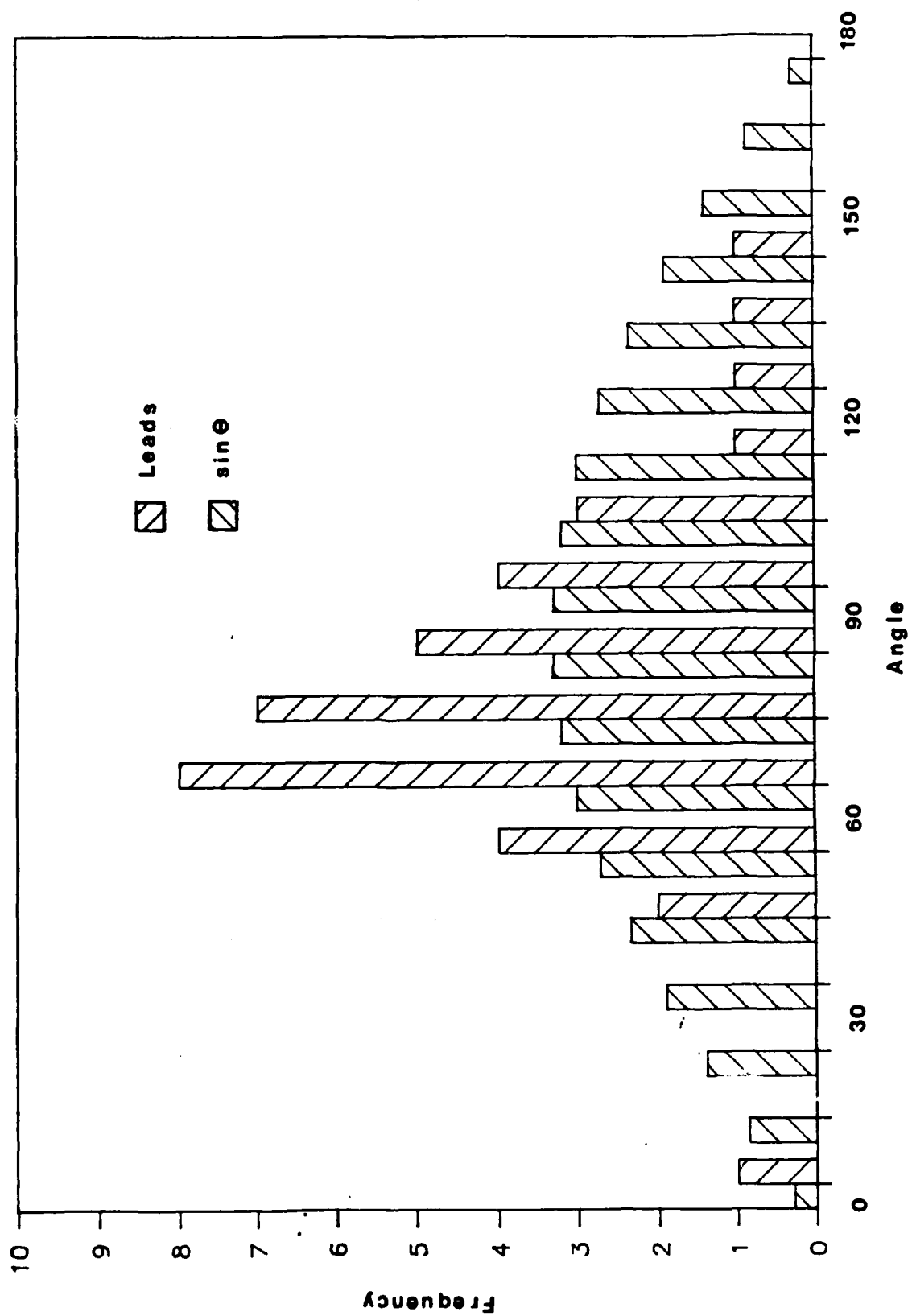


Figure 5

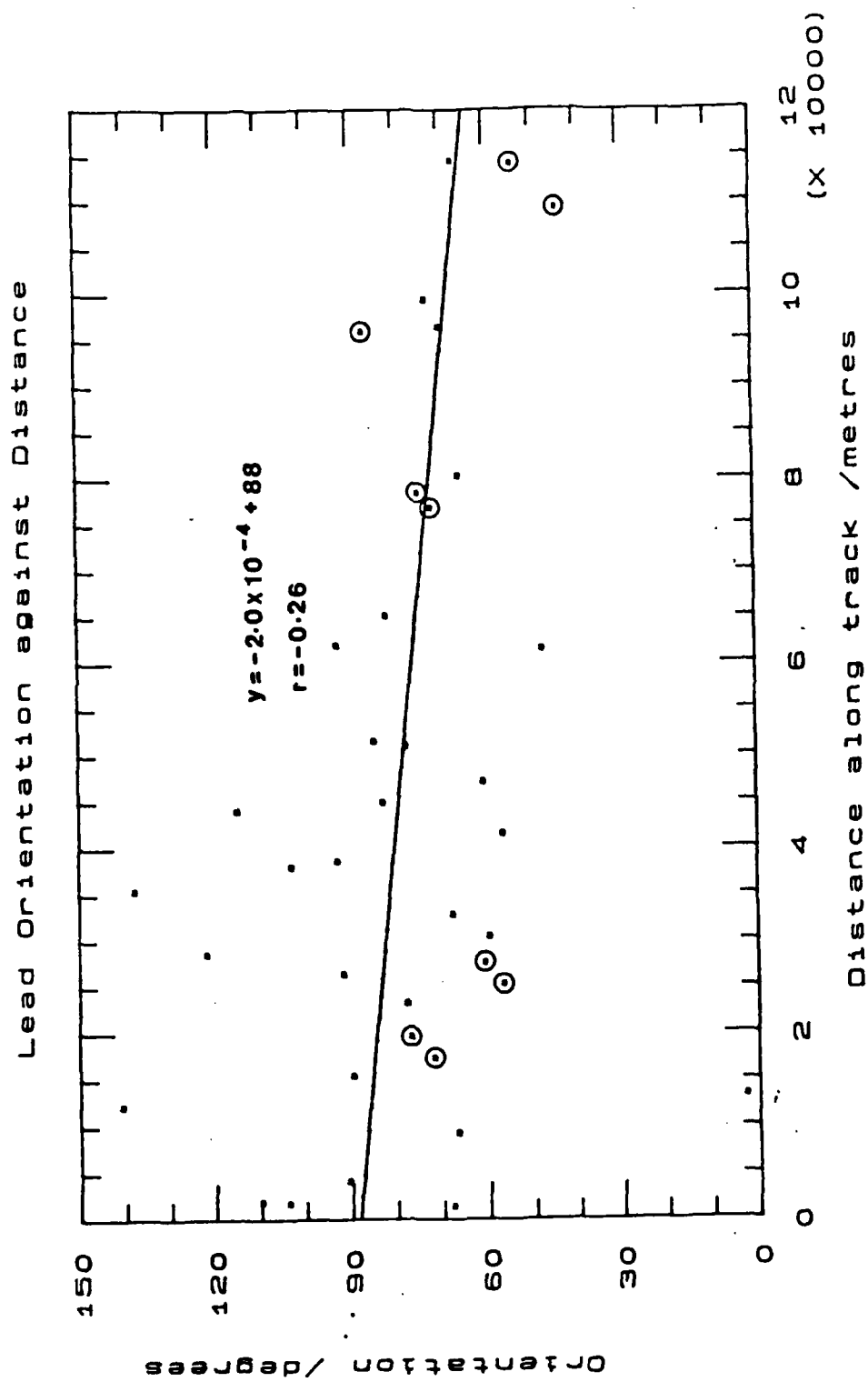


figure 6

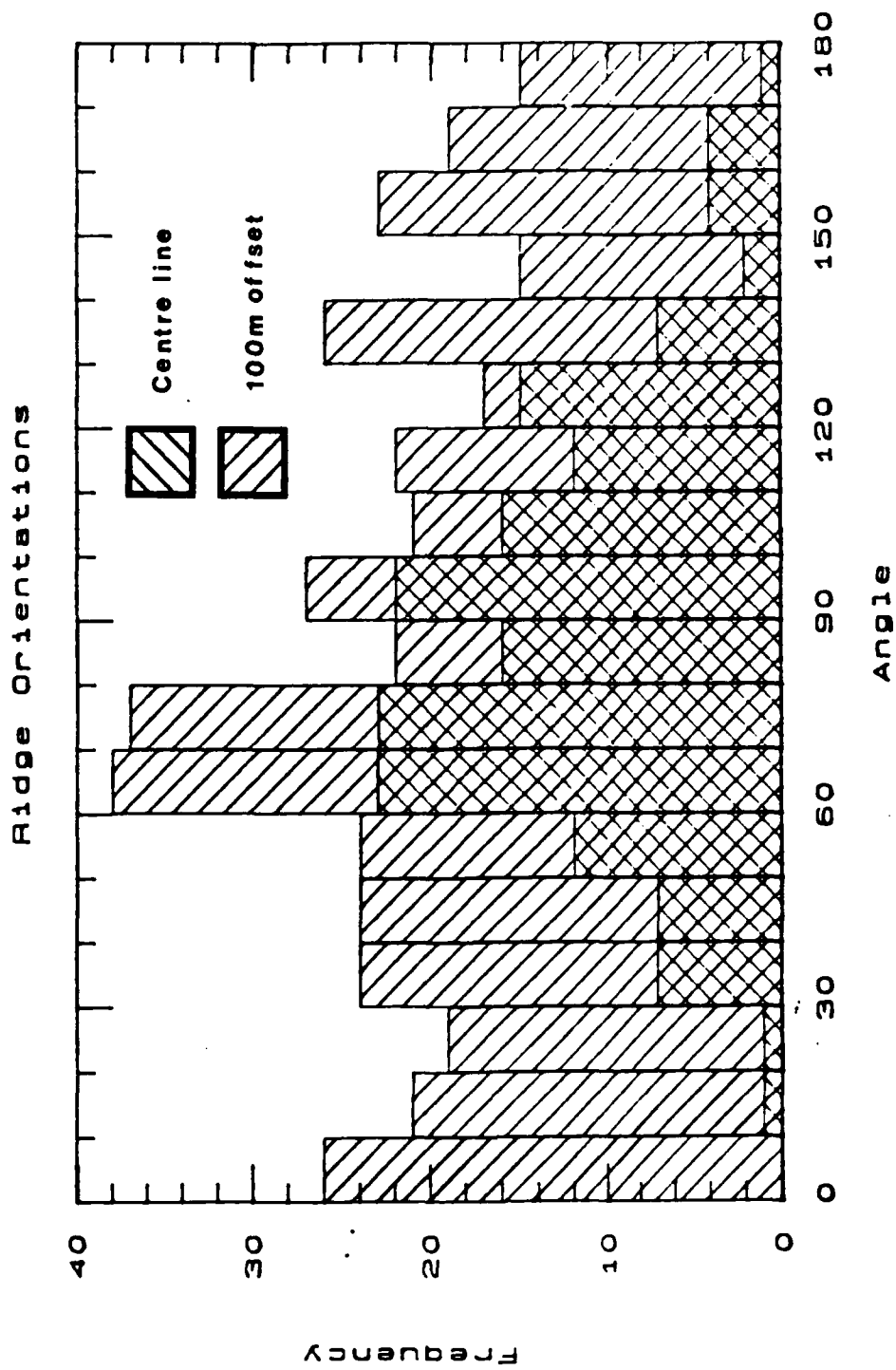


figure 7

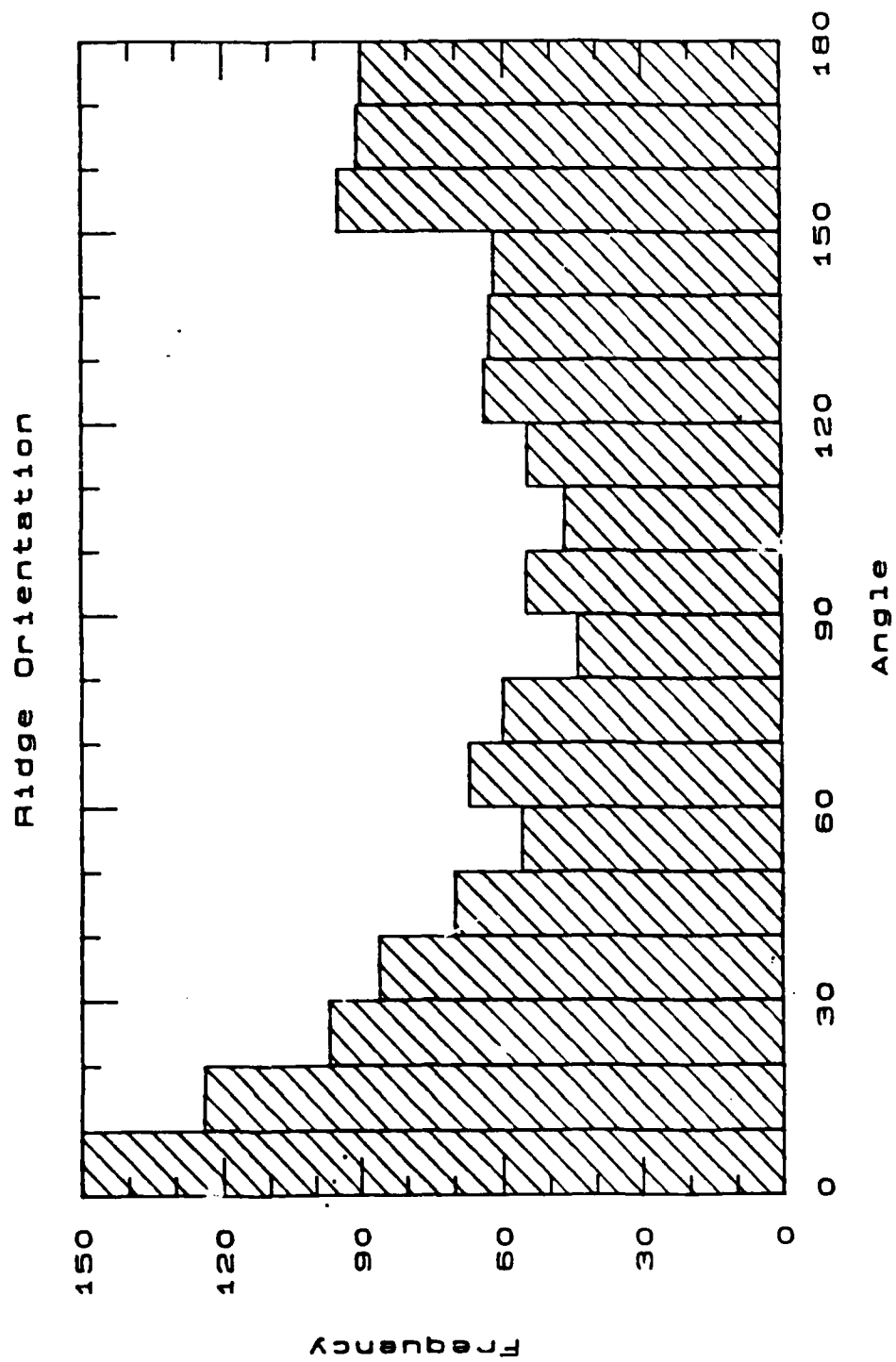


fig 8

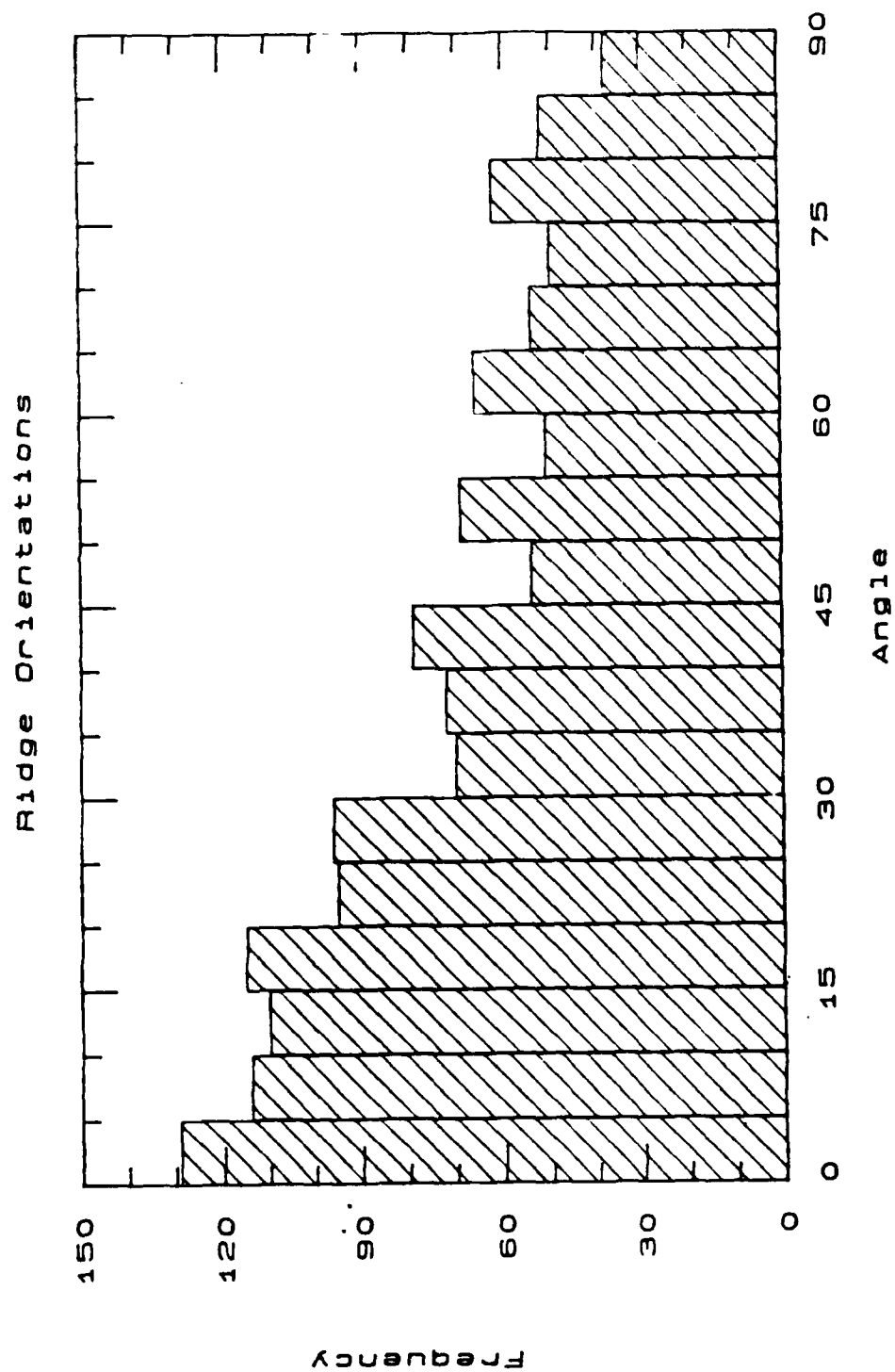


Figure 9

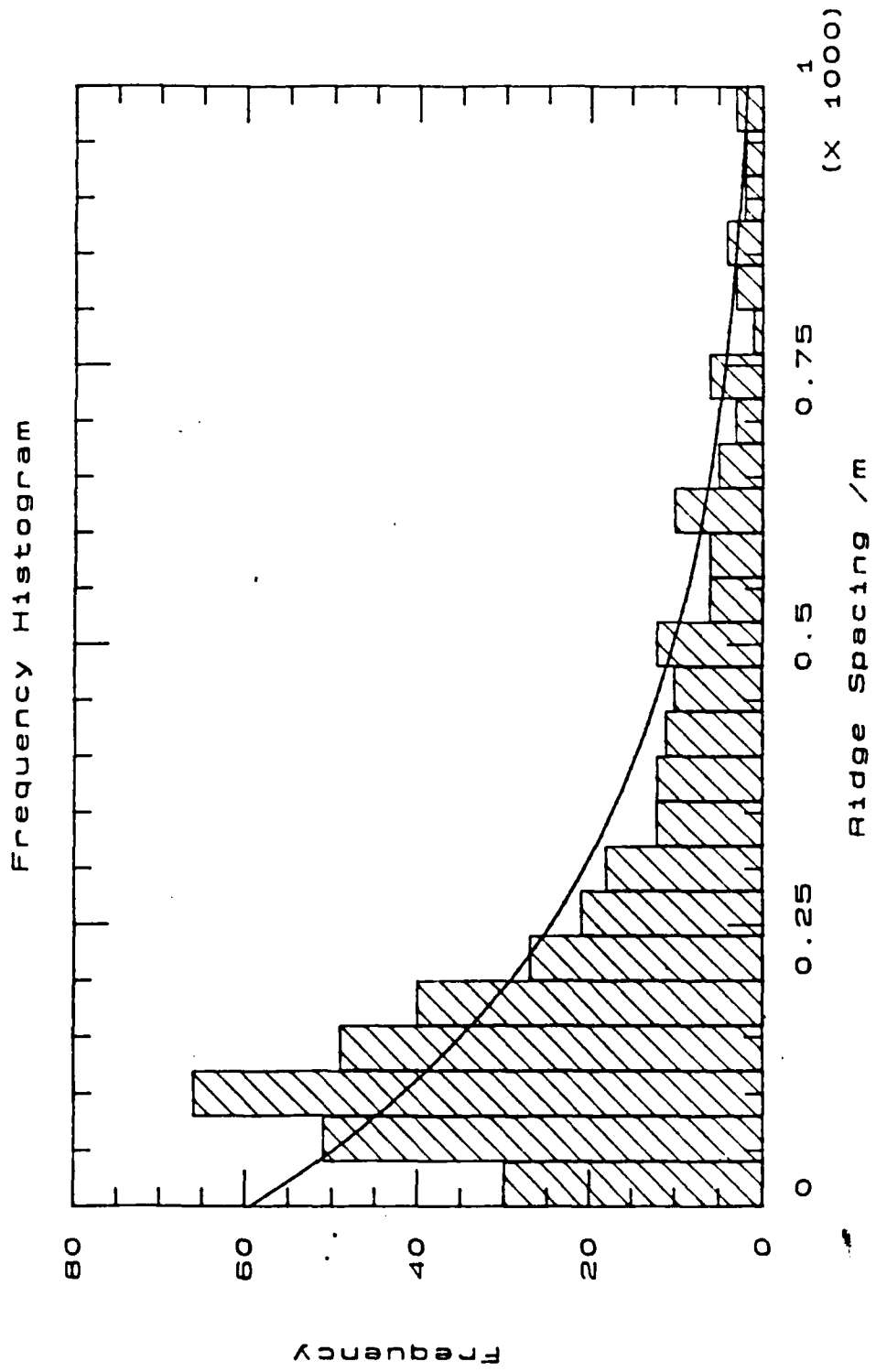


figure 10

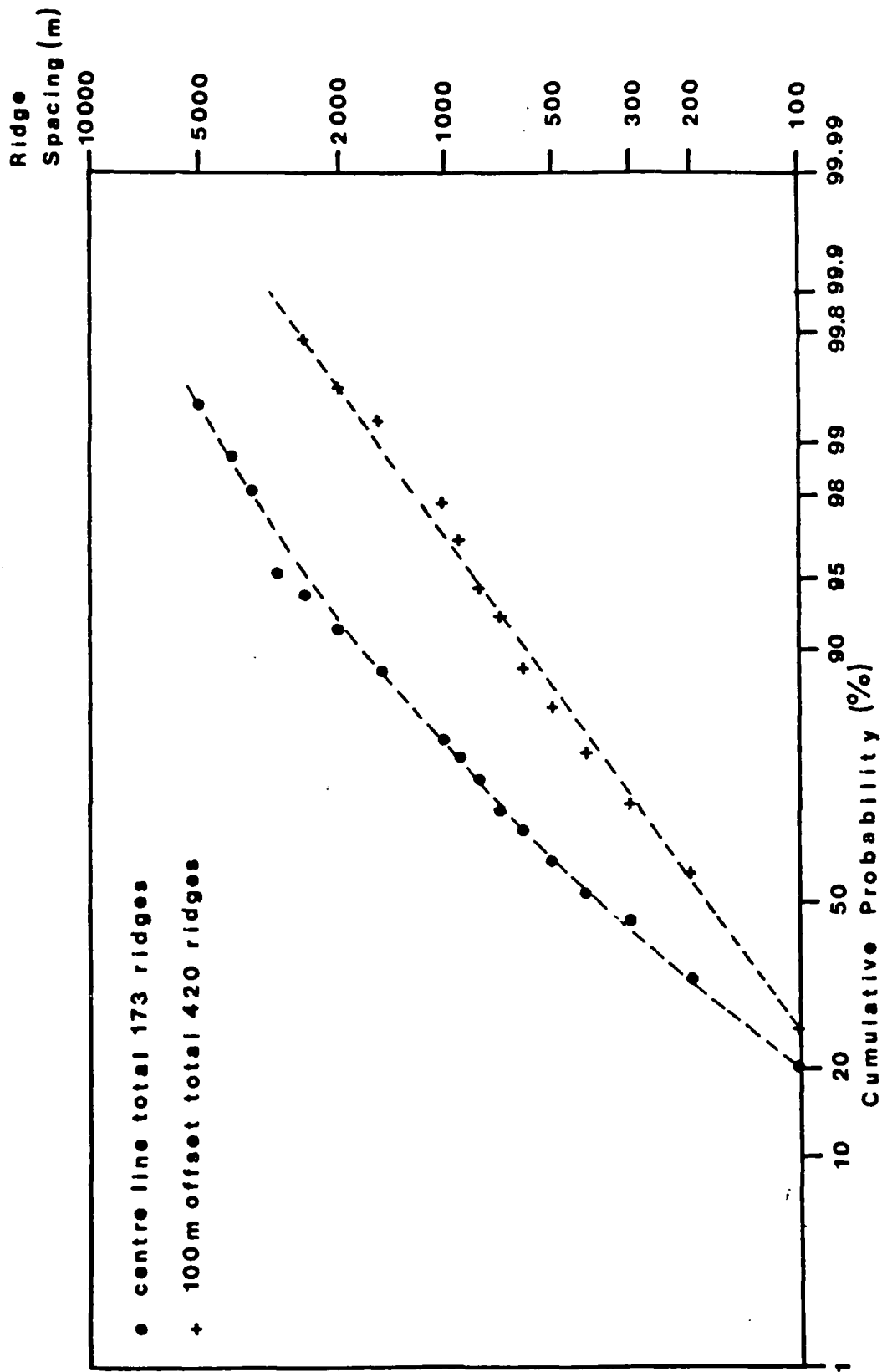
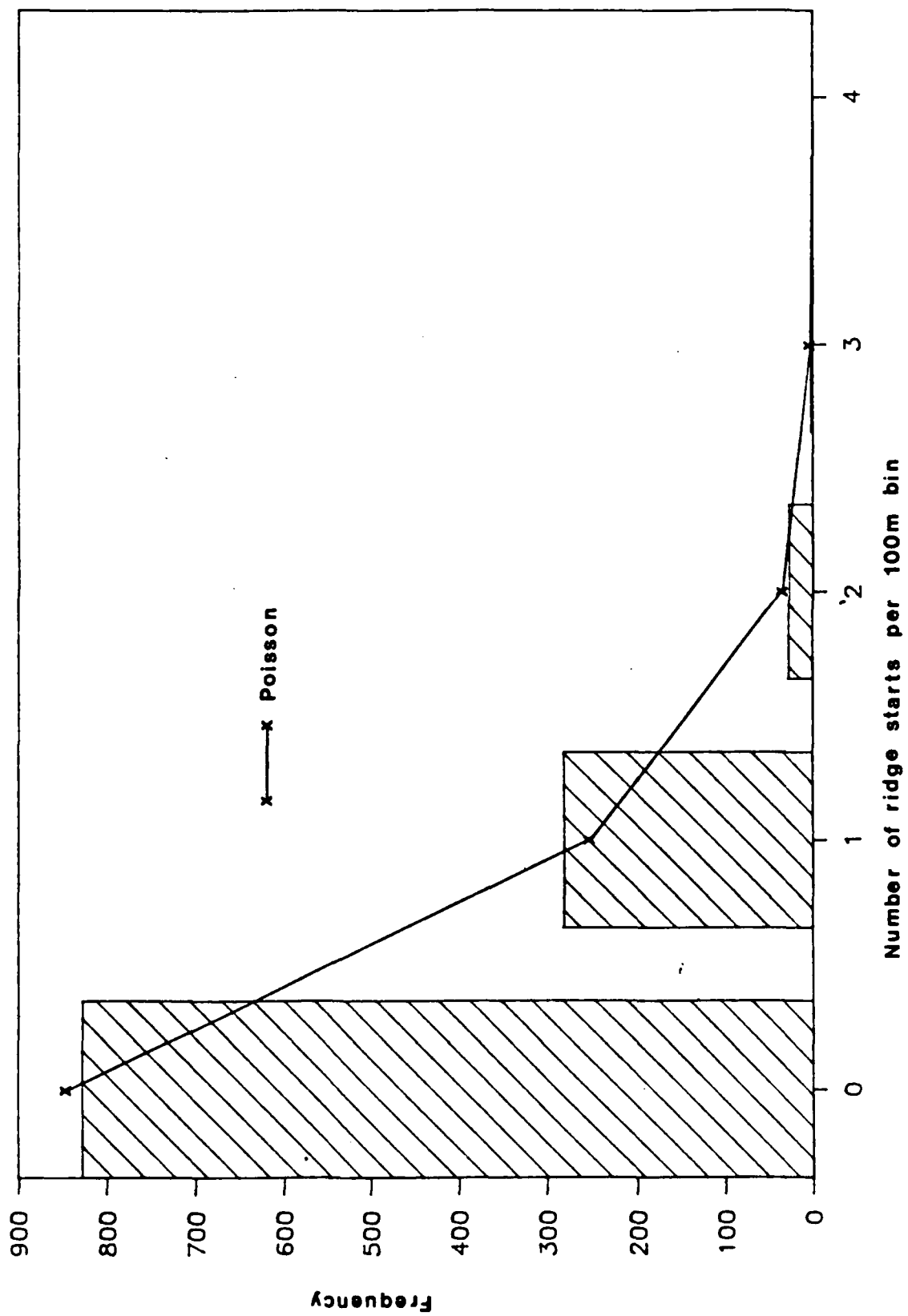


figure 11



UPPER AND LOWER SURFACES OF ARCTIC SEA ICE COMPARED BY THE
USE OF SIDESCAN SONAR AND SYNTHETIC APERTURE RADAR

7

Peter Wadhams

Scott Polar Research Institute
University of Cambridge, Cambridge CB2 1ER

Chris B Sear

Science Applications International Corporation
Block A2, Westbrook Centre, Milton Road, Cambridge CB4 1YQ

1. INTRODUCTION

In this paper we compare data obtained concurrently from a sidescan sonar mounted on a submarine and from an X-band synthetic aperture radar (SAR) operated from an aircraft flying a parallel track and imaging the same region. The aims are to compare the morphology of the upper and lower surfaces as revealed by the two types of sensor, and to determine to what extent the ice surface can be classified into types which are recognisable and comparable between the two sets of imagery.

The data were obtained from the Arctic Basin north of Greenland during a cruise carried out in May 1987 by a British submarine, which was overflown by a Cessna aircraft carrying the Intera Technologies STAR-2 X-band SAR system. A P-3A aircraft of NASA also took part in the experiment carrying a variety of other sensors including passive microwave, laser profilometer, infrared line scanner and cameras. The experiment itself and the datasets obtained by the various sensors are described by Wadhams et al. (1991) and Comiso et al. (1991), while the nature of the sidescan imagery is described by Wadhams (1988) and some results from the upward sonar system fitted to the submarine by Wadhams (1990). The classification of ice types using sidescan sonar validated by upward sonar is described by Sear and Wadhams (1991), which also includes a statistical analysis of two-dimensional ice features as revealed by the sidescan sonar.

2. DATA AND PROCESSING

2.1. Sidescan sonar

Sidescan sonar profiles were obtained using an EDO Western model 602 towfish mounted on the upper casing of the submarine, feeding an EDO 706 sidescan mapping system. The sonar operated at 100 kHz and produced an output in roll form on electrically sensitive paper. The towfish contains two transducers which have a narrow fore-and-aft beamwidth and wide transverse beamwidth, such that the main lobes overlap at the zenith and give relatively uniform signal strength at all angles of incidence on the ice. It was found that an echo

of sufficient strength to delineate bottomside features was obtained over a swath width of 673m, centred on the track line and so the system was normally operated with a swath width of 1km. The system converted the raw sidescan signal, which comprises signal strength against time (and thus range), into a geometrically correct map of the ice underside. This was achieved by using Pythagoras' equation to convert range into lateral distance from the centreline and the use of manually input boat speed to correct the along-track scaling, via a variable paper chart speed. The submarine's depth also had to be input for the lateral distance conversion. Further details of sidescan operation and image generation are given in Sear and Wadhams (1991).

The geometrically corrected image is still not a perfect map of the ice underside. There are three main sources of error:

- a) Error in the manual entry of boat speed, boat depth and average sound velocity into the recording system. Sound velocity errors are minor, but boat speed errors produce a stretching or squashing of the image, while boat depth errors lead to a loss of data near zenith or to a gap along the centreline of the image.
- b) If a pressure ridge has significant draft relative to boat depth, the peak of the ridge is displayed at a smaller lateral distance than is correct. Finite topographic variations will therefore lead to a continuous distortion over the image, since only one depth is entered for the solution to Pythagoras.
- c) If the submarine has a list, there will be a mismatch between the reconstructed maps from port and starboard transducers. This leads, for instance, to a discontinuity in the line of a pressure ridge which crosses the zenith at a slant angle.

The sidescan data were analysed by preparing transparent overlays of the sidescan images, using a swath width of 673m and covering a total length of 140km. The area of each overlay was divided into seven classes which represent different ice types. The classes, and criteria for their identification, are given in Table 1. Further details can be found in Sear and Wadhams (1991), which also describes the results of a validation technique making use of the upward-looking sonar. The initial classification was done using the sidescan alone, but upward sonar provides data which enable us to test the quality of the original classification for features which lay along the centreline of the image (some 25% of all features). Many sources of error and bias were found. These were corrected for zenith-crossing features but not for the others. Therefore some bias remains in the classifications, although the validation process has enabled us to determine in which directions the remaining bias probably lies.

2.2. Synthetic aperture radar

The SAR data were recorded in the form of a digital image on magnetic tape. Details of the STAR-2 system are given in

Akam (1988). The system operates at X-band, and gives an image composed of pixels of side approximately 16m. The pixel brightness is proportional to the radiation scattered from that element of ground surface.

The first necessity in data processing was to collocate the sidescan image to the SAR image. Approximate collocation was achieved by comparison of navigational information from the boat and aircraft, but the final collocation (and compensation on the SAR image for the stretching and squashing errors on the sidescan image described above) had to be done by finding points which could be identified unambiguously on both images. A series of 50 such points were found on the 140km of imagery analysed, based on the similarity of the shapes of features such as leads and prominent ridges in both datasets. The fact that collocation could be achieved in this way is itself evidence that considerable similarity in appearance between top and bottom was evident. Scaling factors for the 49 SAR sections lying between tie points were derived from the corresponding distances measured off the sidescan, and the sidescan images were rotated and translated so as to match and overlay the SAR images. The best possible collocation was thereby achieved. It is worth noting that because of the difference in speed of the aircraft and submarine, the SAR data can be viewed as a snapshot of the region, whereas the submarine might take several hours to traverse it. The SAR imagery was collected within a few hours of the passage of the submarine. However, some translation, rotation and deformation of the ice field would have occurred between the collection of the data sets. This makes absolute location of one on the other impossible.

The SAR image corresponding to the sidescan swath was contrast-stretched to aid classification of ice types, and then image-written and enlarged using a GEMS image analysis system. Finally, it was printed onto hard copy. The hard copy image was then classified manually in the same way as the sidescan image (again producing a classified transparent overlay) but using internal criteria for identification of classes based on brightness and texture (as given in Table 2). Table 2 also shows our *a priori* initial expectations of what these particular seven classifications might be associated with, or represent, in terms of real ice types. This *a priori* interpretation was based on our experience of the physical appearance of Arctic pack ice and an initial qualitative comparison between sidescan and SAR. As shown below, our expectations were not always fulfilled.

3. ANALYSIS

3.1. Statistical properties of sidescan classifications

The statistical analysis of the sidescan overlays was carried out after corrections had been applied to take account of validation by upward sonar. The results are described thoroughly in Sear and Wadhams (1991) and are only summarised

here in order to place the results of the comparison in perspective.

The analysis of areal percentages showed that 49.7% of the area of the ice cover was composed of matrix (Table 1), an irregular, random array of deformed ice with no apparent lineation of ridging. This is clearly related to the high level of deformation which occurs to ice in this region (north of Greenland) because of the nearness of a downstream fixed land boundary. 29.7% of the area was composed of multi-year ice, 14.7% of ridging, and all other categories made minor contributions (1.9% dark leads, 1.1% bright leads, 1.8% first-year ice and 1.1% unknown). The very low percentage of undeformed first-year ice is especially noteworthy. This makes it difficult to derive conclusions about the nature of this kind of ice in relation to SAR imagery.

An analysis of the sequences of ice types occurring along two lines (offset from the submarine track by 100m each side) showed a number of predictable associations. For example, dark and bright leads tended to be juxtaposed. However, some surprising associations are indicated. Leads, for instance, are distributed through the icefield so as to be significantly less likely to be next to ridges than to be away from ridges. This counters a commonly held belief that ridges tend to occur beside the edges of leads. Leads are also associated in a significantly negative way with multi-year ice. This is probably because first-year ice fails preferentially under divergent or shear stress, so that leads tend to be embedded between first-year floes rather than multi-year floes. Multi-year ice and first-year ice also have a significant tendency not to be juxtaposed, evidence that such boundaries are unstable and tend to result in ridge formation.

An analysis of the orientations of bright and dark leads showed that in this region they were not random, but had a significant tendency to be oriented in the sector 60°-70° east from north. A study of the along-track variation in this orientation showed that there was a slowly-varying trend in the preferred orientation, with the angle from north decreasing with increasing distance eastwards. This is an indicator of the large length scale over which the ice deforming forces vary.

Most leads were less than 100m wide. The mean width of leads occurring in this region was 79.4m and median width 35.3m. The distribution of lead widths resembled that observed from some earlier datasets from M'Clure Strait and the Beaufort Sea. The distribution of lead spacings showed a dominant peak at 2 to 3km, indicating a strong regularity in the way in which the ice stress causes leads to open.

Analysis of pressure ridges along two transects along track showed that their orientations were also peaked in the range 60°-80° east of north. A total of 1378 orientations were recorded using the whole width of the sidescan record. Their frequency distribution appears quite uniform but with a tendency to dip in the centre, near $\pi/2$ (Figure 1). It is

likely that a detectability factor is at work here, since ridges orientated normal to the submarine track are less easy to detect on sidescan than ridges orientated parallel to the track. Ridge spacing was found to fit a log-normal distribution, as has been observed for previous datasets (Wadhams and Davy, 1986). However, except for closely spaced ridges (less than 150m), the data also fit a negative exponential distribution, indicating random spacing along track. This was confirmed by an analysis numbers of ridge starts in 100m bins, which indicated that ridges were Poisson (and thus randomly) distributed along track.

3.2. Statistical properties of SAR classifications

The SAR transparencies were statistically analysed in the same way as sidescan sonar. Some results of the analyses are given below.

In considering feature areas and areal distributions, we found that Type B, possibly consisting of refrozen leads, had a distribution which was strongly peaked at the low end (Figure 2), while the distribution of bright linear areas (Type F - possibly ridge sails) was not significantly different to that of a two parameter log-normal (Figure 3). Type E (possibly multi-year floes) also fitted a log-normal distribution (Figure 4), as did Type C (Figure 5 -possibly first-year ice floes). Thus it appears that the log-normal has some general validity for describing the distributions of floe area and of bright linear features (possibly ridge sails), as well as the spacing distribution between pressure ridges which it has already been found to describe well (Wadhams and Davy, 1986). The absolute feature numbers in the case of the present dataset are too small to confirm the validity of the log-normal over all other possible distributions.

Table 3 shows the percentage areas of the SAR types and compares them with those of the sea ice types derived from sidescan imaging over the same area. A comparison is made in Section 3.3. Overall, the SAR imagery indicated that Type G covered 49.7% of the study area, Type F 9.5% and Type E 29.5%. Types A to D accounted for 11.3% in total.

In considering ridge orientations we found that the Type F (possible ridge sail) orientation distribution dipped close to 90°, i.e. normal to the aircraft track (Figure 6), in a similar, though much more noticeable, way to that indicated by the validated sidescan, for ridge keels. The data swath is wide enough that, for the case of random ridge sail orientations, we would expect a uniform distribution of observed angles. This result suggests that ridge sails observed on SAR have a strong tendency to lie parallel to, or rather within an angle of between 0 and 50° from the line of flight. This is most likely to be a function of the way that SAR images sails and thus indicates either that not all sails present are being detected by the SAR, or indeed that Type F are not necessarily equivalent to ridge sails, as would be seen *in situ*. This lends a cautionary note to further comparative analyses. Assuming that the actual distribution of ridge sails

is at least as uniform as indicated by that of ridge keels and that the SAR images ridge sails as bright linear features (which one would expect), then a large proportion of ridge sails are missed by the SAR. This has implications in several areas, for example for studies of sea ice motion and of drag coefficients over ice.

SAR Type F features were extracted along a transect, a total of 176 features. The spacing between individual Type F features (from start to start) was investigated. The mean spacing was 668m, the median was 351m. Figure 7 shows the distribution of spacings. It illustrates the close fit of the observed distribution to a log-normal distribution (curved line). Indeed the observed distribution was found to be insignificantly different from a log-normal. The spacing data were also compared with a negative exponential (not shown) but the fit was not as good because of the fall off in the frequency of spacings below 100m. For longer spacings the observed distribution closely matches a negative exponential and thus indicates that Type F features were distributed randomly along track.

3.3. Comparison of sidescan and SAR

3.3.1. Areal statistics

As Table 3 indicates the same proportion of the study area is covered by Type G as by Matrix. Also, the areas of Multi-year ice and E are the same. This remarkable correspondence between imagery classified independently is very encouraging. It leads us to confirm that X-band very successfully distinguishes multi-year ice and rubble fields. Similarly and as expected, the SAR distinguishes dark leads (open water). As expected, using X-band SAR, it is less easy to tell apart refrozen leads and first-year ice. Finally, as suggested by our analysis of orientation, the X-band SAR appears not to image ridges in the same way as does the sonar. The area of possible ridge sails on the surface is significantly smaller than that of keels.

3.3.2. One-to-one comparison

The final product of the track collocation and ice type classification procedures described in Section 2 was a pair of sets of transparent overlays, to the same scale and covering the same terrain, representing the classification of the ice surface (based on an interpretation of SAR) and ice types based on the underice surface (derived from a validated sidescan map). If the collocation were perfect and if the upper ice surface as classified from SAR perfectly matched the lower ice surface as classified from sonar, then we would expect the two sets of transparencies to show a 1:1 correspondence between areas covered by a particular sidescan ice type (from Table 1) and a particular SAR ice type (from Table 2). Table 2 indicates the type of correspondence which we might have expected to see, based on reasonable hypotheses concerning the nature of sea ice and the way in which it

scatters radiation.

Clearly such perfect correspondence cannot be attained. Three factors prevent it:

(a) The less than perfect matching of the images on a scale of metres or tens of metres (even if we assume that the tie points produce perfect correspondence over scales of 3 to 4km, the average spacing between the points used).

(b) The fact that there is a genuine difference between the geometry of the upper and lower ice surfaces (this is already known from the comparison of upward sonar profiles with laser profiles, for example, Wadhams, 1981).

(c) The fact that the sidescan and the SAR image the ice in different ways. Sidescan responds almost entirely to the surface gradient of the ice. Thus, it is best at displaying roughness and texture. On the other hand, SAR responds both to surface roughness and to the conductivity profile in the upper layers of the ice cover. Thus, it so shows distinct differences between ice of different thicknesses and ages but similar roughness.

We proceeded to test for the quality of match between the two sensor outputs. As reference ice type we decided to use pressure ridges as identified on sidescan. This is because, as described in Section 3.1, we found, in our validation testing of the sidescan against upward-looking sonar, that almost all features identified as pressure ridges on sidescan really were pressure ridges, despite the fact that the upward-looking sonar also revealed ridges in the icefield which had not been identified in the sidescan overlay procedure. Thus we can be confident that each area of icefield marked as 'pressure ridge' (r) on the sidescan overlay really is an area of ice bottom surface which is composed of pressure ridging. We could then match these areas against SAR to see whether there was a statistically valid preferred ice type in the SAR which occurs in the same locations as the ridges on sidescan. The question which we seek to answer is: does a particular SAR category correspond significantly in location with the sidescan category which we know is ridging?

The technique used was as follows. The substrate was the SAR transparency series. Working between tie points, the sidescan overlays were fitted over the SAR transparencies as closely as possible. Final, small adjustments were permitted only if some very clear feature such as a lead was present, which can be expected to give perfect correspondence between top and bottom (except for the effect of relative motion during the 2 to 4 hours between the collection of the two datasets). For every ridge on sidescan, the estimated fractions in tenths of the area of the ridge underlain by different SAR ice types was recorded. A total of 1364 ridges were examined on 74 frames of sidescan (corresponding to 119km of track) which matched SAR underlay.

This procedure gave results in which every ridge was given the same weight regardless of size. We compared these results with the overall relative areas occupied by different ice types on the whole SAR dataset, to see whether, for a

given category, our rate of 'hits' exceeds chance expectation. This assumes that success rate in hitting is independent of the size of ridge, which is a conservative assumption since we might expect large prominent ridges to match better than small ridges.

Data were analysed for groups of ten frames (corresponding to about 15km of track), to test for repeatability and were then combined. The overall results are shown in Table 4. The SAR categories are as given in Table 2 and the figures represent the total number of unit ridge areas underlain by each category of SAR ice type. Table 4 also shows the overall percentage area of the transparency occupied by each SAR classification. Systematic differences between these two sets of numbers indicate an association (positive or negative) between a SAR ice type and the location of ridging on sidescan. The significance level of each association is listed, first using the assumption that each association can be tested independently as if the others were not under test. Second, a more conservative assumption was used: that since seven statistical tests were carried out in aggregate, the significance level of an individual test should be reduced by a factor of seven.

Significance tests were carried out as described below. We refer to the case of ice type F to illustrate the method. Classification F showed the strongest positive association. Table 4 indicates that 9.52% of the area of the whole ice field (as seen by SAR) is occupied by ice of type F. Using the null hypothesis (H_0) that there is no association between sidescan and SAR images we expect 9.52% of the area of ridged ice on the sidescan image to be underlain by type F ice when the sidescan transparency is laid over the SAR. In fact, 17.07% of the sidescan ridged ice is underlain by type F ice (when analysed as 'tenths of unit ridges') using a sample of size 1364. The appropriate significance test is a one-tailed test on a normal variate. If H_0 is true, the sample mean (\bar{X}) should be 129.9 (1364×0.0952). The observed mean is 232.8. The sample standard deviation (s) should be \sqrt{Npq} where $N=1364$, $p=0.0952$, $q=(1-p)$. This gives $s=10.84$. The actual mean in standard units (z) is then $(m - \bar{X})/s (=9.49)$. This implies that the observed mean is 9.49 standard deviations away from the mean expected from H_0 , which is significant at better than the 0.1% level. Since we are doing the same test on seven ice types, we should be conservative and reduce the significance level by a factor of seven. The result for F is still significant at better than the 0.1% level.

From the results shown in Table 4, we draw the following conclusions:

1. The spatial coincidence between sidescan ridges and SAR ice classifier F is highly significant.
2. There is a positive association between sidescan ridges and SAR ice type C, significant at the 1% level.

3. There is a negative association between sidescan ridges and SAR ice types A and E, which is also significant at the 1% level.
4. There is a negative association between sidescan ridges and SAR ice type G, which is significant at the 5% level.
5. There are no significant relationships between the occurrence of sidescan ridges and SAR ice types B and D.

Furthermore, the positive association between ridges and Type F, noted above, which is only twice the level expected by chance may indicate that while, in many cases the same features were identified, they were not orientated in similar directions on the top and bottom surfaces of the ice. This is illustrated clearly in Figure 8. Figure 8 shows a small matched section of digitised sidescan (Figure 8a) and SAR features (Figure 8b), approximately XXXXm long and 673m wide, covering the same region as shown in the original imagery (Figure 9) (Perhaps this should be Figure 1). Here, the major lead features are clearly well located but individual ridges and areas of multiyear ice observed using the sonar are hard to match to similar features, seen on the SAR. Many SAR Type F features are not seen on the Sidescan (for example to the left of the lead marked L1). Even where ridges and Type F features are observed in the same region (for example Area 2 to the far left of L1), individual features can not be unambiguously matched. Here the ridges appear to trend parallel to the track, whilst the Type F features seen are angled away from the track and Type E features (multiyear ice) make up the rest of the area of confused ridging. To the right of the lead marked L2, an example is seen of a region in which three clear ridges were identified by the sidescan (one horseshoe shaped, one parallel to the track and one at approximately 45° to the track) but no clear Type F features were observed on the SAR image.

4. DISCUSSION AND CONCLUSIONS

What are we to make of the associations discovered in the analysis of Section 3.3? First, it is gratifying that a strong positive association is found between the occurrence of ridging on the ice underside and the perception of a bright linear feature on the topside which was identified, *a priori*, as a prominent ridge (SAR Type F). Nevertheless, the observed occurrence is only about double the level expected by chance, so the coincidence of imagery is by no means perfect. It is impossible to judge to what extent this imperfection is due to: small-scale mismatching in the final image overlaying, or to possible ridge sail crests (SAR) and ridge keel crests (sidescan) being angled differently, or finally, to a real failure of ridges to always identify themselves on the topside and the bottomside in ways recognisable to these sensors.

The second positive association, between sidescan ridges and SAR ice Type C, is yet more puzzling. Type C ice is light

grey, floe-shaped, with some texture and with faint lines running through it. Where possible the lines were extracted and classified separately as Type D. Our a priori interpretation is that Type C is first-year ice and that the lines are either first-year ridges or else correspond to the cracks which are observed to criss-cross first-year floes on the underside as seen by sidescan (Wadhams, 1988). Such a crack would be a strong target for SAR and because it penetrates the ice vertically, the aperture synthesis process may give such a feature an apparent width in a SAR image which is greater than its real width. Nevertheless, it appears that Type C ice corresponds significantly to ridged area on sidescan. This implies either that the faint lines, even when not separated, are indeed first-year ridges, which are wider underneath than on the upper surface, or else that the entire area of Type C corresponds not to first-year floes but to ridged ice of some characteristic kind.

The negative associations, with apparent open water and multi-year floes, are comprehensible and insignificant associations seen between Type F and some categories may be a function of the small sample sizes.

Some qualitative observations made during the analysis may be helpful towards answering the question of whether the significant, but not overwhelming, associations observed here are due to mismatch or to real differences in ice morphology (see Figure 8). First, an excellent match between prominent features on each type of image would often occur in some location, and then a match of similar quality would recur 3 to 4km farther along the track, but the intervening region might show no match at all. Realistically, this could not have been because of local mismatch in collocation but rather appears to be because the terrain consisted of a nondescript heavily deformed rubble, which was difficult to categorise both on SAR and sidescan. This dataset was obtained in the heavily ridged area north of Greenland, and much of the imagery was of this type, with few or no undeformed floes visible. Probably this helped to reduce the ability of the analysts to obtain matching in categorisation, and suggests that a similar analysis should be done of coincident imagery in a less strongly ridged region of the Arctic.

A second observation was that in frames where an excellent matching of transparencies could be achieved because of the presence of a characteristically shaped lead, the coincidence of ridges was no better than in the dataset as a whole. This implies that there is a real difference between ridge identifications from each sensor.

Finally, it was observed in some cases that a sidescan ridge of prominent and distinct shape was underlain by a SAR feature of similar distinct shape and identical location (beyond the possibilities of chance coincidence) and yet the SAR classification was B,C or D rather than F.

We conclude that although there is certainly a significant correlation between SAR and sidescan as far as

ridge identification is concerned, the correspondence is not 1:1. Under-ice features which we know to be ridges can correspond to above-ice SAR signatures which are variable enough to lead an observer to place them in a number of different categories. This must lead to continuing caution in attempts to quantitatively interpret SAR imagery in terms of ice type. Much more work, including further validation studies, is needed. For example, it appears that the true nature of the upper surface and particularly of ridges, can not be seen using a single X-band SAR image. Thus, we strongly recommend that a region should be imaged by two SAR flights at right angles, better to pick out all possible ridge sails, whilst coincident under-ice sidescan and upward-looking data are collected which give the most reliable large scale ice type data possible.

5. ACKNOWLEDGEMENTS

We are grateful to Flag Officer Submarines, Northwood, for granting us permission to use the submarine in the original experiment and to Admiralty Research Establishment, Portland, for funding the SAR flights. Funding for submarine sensors and data analysis was provided by a contract from Office of Naval Research to Science Applications International Corporation (no. N00014-89-C-0014) and by a grant from Natural Environment Research Council to Scott Polar Research Institute. Finally, we thank Alison Scoon and Mark Fearon for their support in data analysis.

6. REFERENCES

- Akam, B. (1988). An integrated radar imaging system for the STAR-2 aircraft. IEEE 1988 National Radar Conference.
- Comiso, J.C., P. Wadhams, W.B. Krabill, R.N. Swift, J.P. Crawford and W.B. Tucker III (1991). Top/bottom multisensor remote sensing of Arctic sea ice. J. Geophys. Res., in press.
- Sear, C.B. and P. Wadhams (1991). Statistical properties of Arctic sea ice morphology derived from sidescan sonar images. Prog. Oceanogr., submitted.
- Wadhams, P. (1978). Sidescan sonar imagery of sea ice in the Arctic Ocean. Canadian J. Remote Sensing, 4, 161-173.
- Wadhams, P. (1981). Sea-ice topography of the Arctic Ocean in the region 70°W to 25°E. Phil. Trans. Roy. Soc., Lond., A302, 45-85.
- Wadhams, P. (1988). The underside of Arctic sea ice imaged by sidescan sonar. Nature, Lond., 333, 161-164.
- Wadhams, P. (1990). Evidence for thinning of the Arctic ice cover north of Greenland. Nature, Lond., 345, 795-797.
- Wadhams, P. and T. Davy (1986). On the spacing and draft

distributions for pressure ridge keels. J. Geophys. Res, 91,
10697-10708.

Wadhams, P. and S. Martin (1990). *****

Wadhams, P., J.C. Comiso, J. Crawford, G. Jackson, W. Krabill,
R. Kutz, C.B. Sear, R. Swift, W.B. Tucker and N.R. Davis
(1991). Concurrent remote sensing of Arctic sea ice from
submarine and aircraft. Intl. J. Remote Sensing, in press.

Multi-year ice (m)	Coherent area of icefield with rugged appearance and distinctive "bulges" on otherwise smooth local topography. Causes of these bulges are discussed by Wadhams (1988) and Wadhams and Martin (1990).
First-year ice (f)	Smooth underside, often criss-crossed by patterns of narrow cracks.
Ridges (r)	Linear set of broken ice blocks. Where several ridges cross or run in parallel, each ridge was separately identified and its crest line traced.
Bright leads (l)	Narrow linear areas of uniform ice of low draft (shown by upward sonar), giving a bright sonar return. Our assumption is that this is thin smooth ice giving specular reflection, so these are refrozen leads. In some cases, however, upward sonar signal strength suggests open water.
Dark leads (w)	Similar areas but giving a dark (i.e. strong) sonar return, denoting high backscatter and suggesting wind-ruffled open lead.
Matrix (Mx)	Areas composed of deformed ice blocks, but with no identifiable linearity which would enable individual ridges to be extracted. Such areas are common in this region, and were first seen by Wadhams (1978).
Unknown (U)	Unidentifiable regions, usually near outer range limit of sonar.

Table 1. Ice classes used in sidescan sonar analysis and criteria for their identification.

- A Very dark return (black); features tending to have some linearity.
- B Very dark grey return, with slightly mottled appearance but differing only slightly from A and often seen along the edges of A, or replacing A in narrow linear features.
- C Light grey regions with some texture and faint lines running through them. Often apparently floe-shaped.
- D Faint lineations within C.
- E Non-linear (floe-shaped) features with a mottled mid-to-dark grey return which gives a textured or bumpy appearance.
- F Narrow linear lines of very bright (white) return.
- G Matrix, a mottled region of mid-grey and white returns suggesting a rough terrain but with no distinct shapes.

A priori expectations of corresponding ice type:-

- A Open water or very thin ice within a lead.
- B Refrozen lead with pattern of cracks or rafting in the young ice.
- C First year ice floes.
- D Ridge sails in first year ice.
- E Multi-year ice floes.
- F Prominent ridge sails of unknown age.
- G Possibly randomly deformed multi-year ice.

Table 2. Ice classifications used in SAR analysis and criteria for their identification.

Sidescan		SAR	
Type	% Area	Type	% Area
Lead w	1.1	A	1.0
Lead l	1.9	B	4.3
Firstyear	1.8	C	5.6
-		D*	0.4
Multiyear	29.7	E	29.5
Ridge	14.7	F	9.5
Matrix	49.7	G	49.7
Uncl'fd	1.1	-	-
Total	100.0	Total	100.0

* Lineations within C

Table 3. Comparison of SAR classification with sidescan classification along 119km of best collocation.

	Ridges	Ridges Underlain By SAR Types						
	Present	A	B	C	D	E	F	G
	1364	1.7	46.5	102.1	10.7	338.7	232.8	631.5
Percent		0.1	3.4	7.5	0.8	24.8	17.1	46.3
Total %		1.0	4.3	5.6	0.4	29.5	9.5	49.7
Significance level:								
Independent		<0.2%	not	<0.2%	<1%	<0.2%	<0.1%	<1%
Aggregated		<1%	not	<1%	not	<1%	<0.1%	<5%

Table 4. Results of matching SAR transparencies to areas occupied by ridging on corresponding sidescan transparencies.

Figure 1

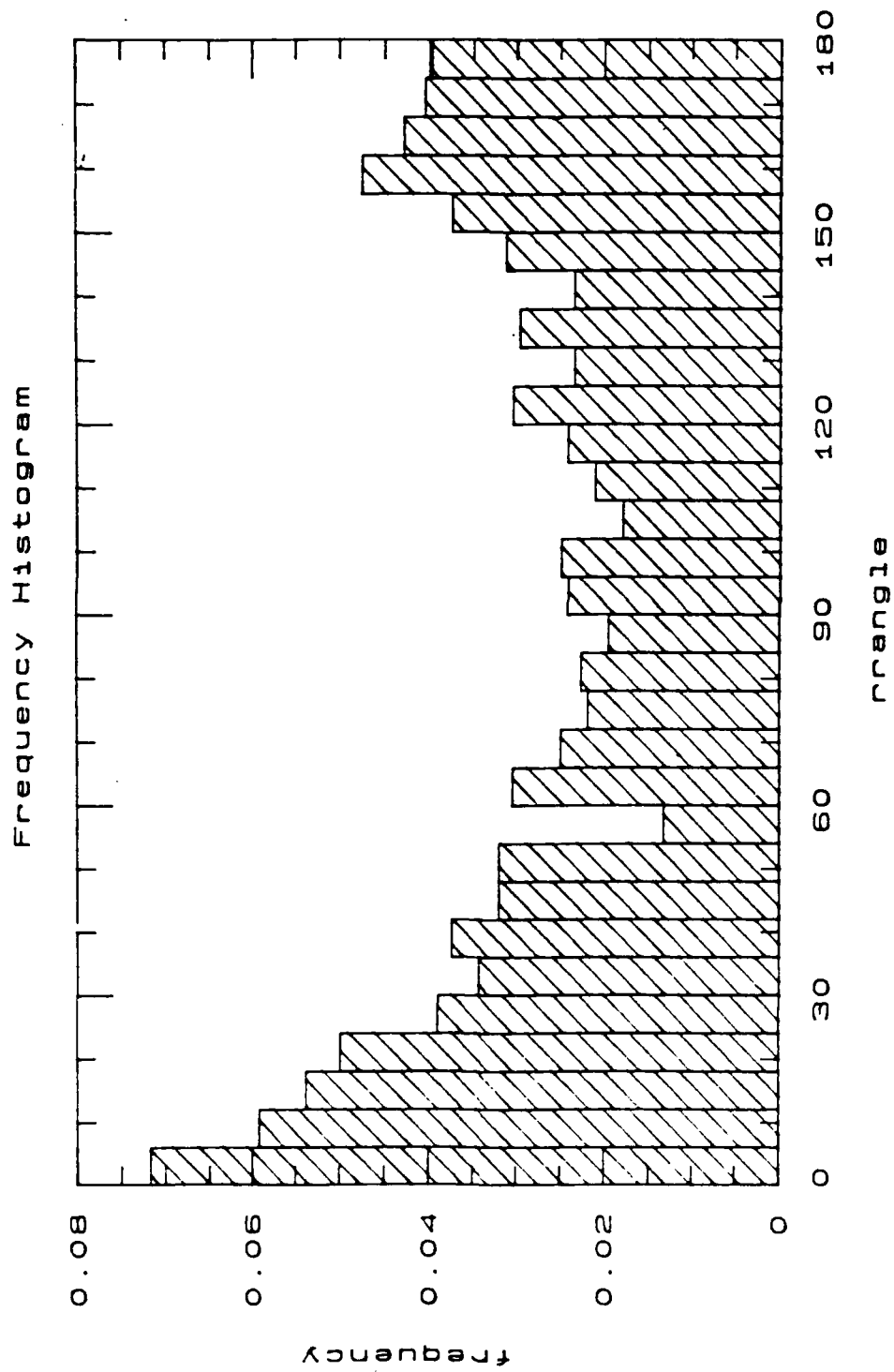
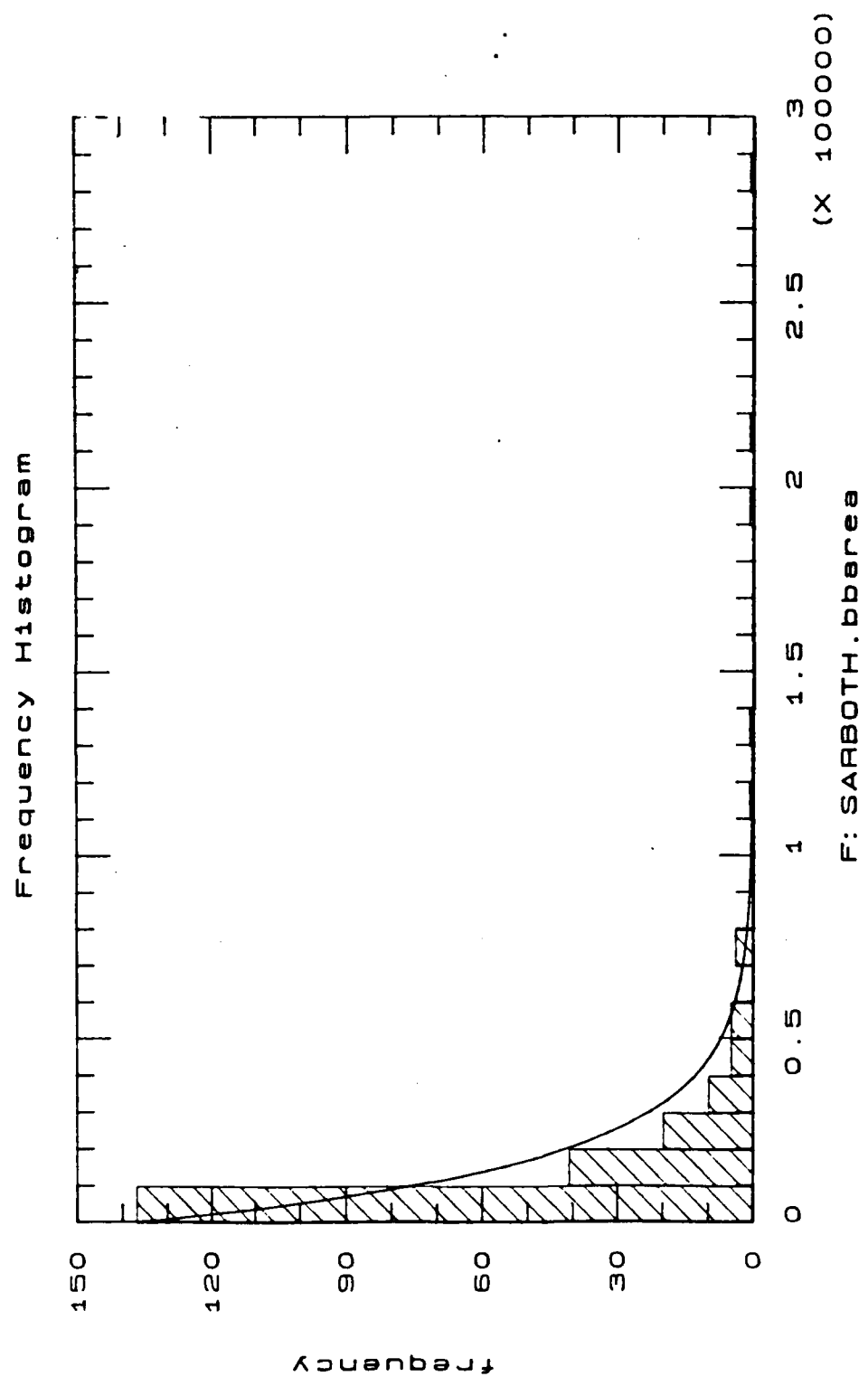
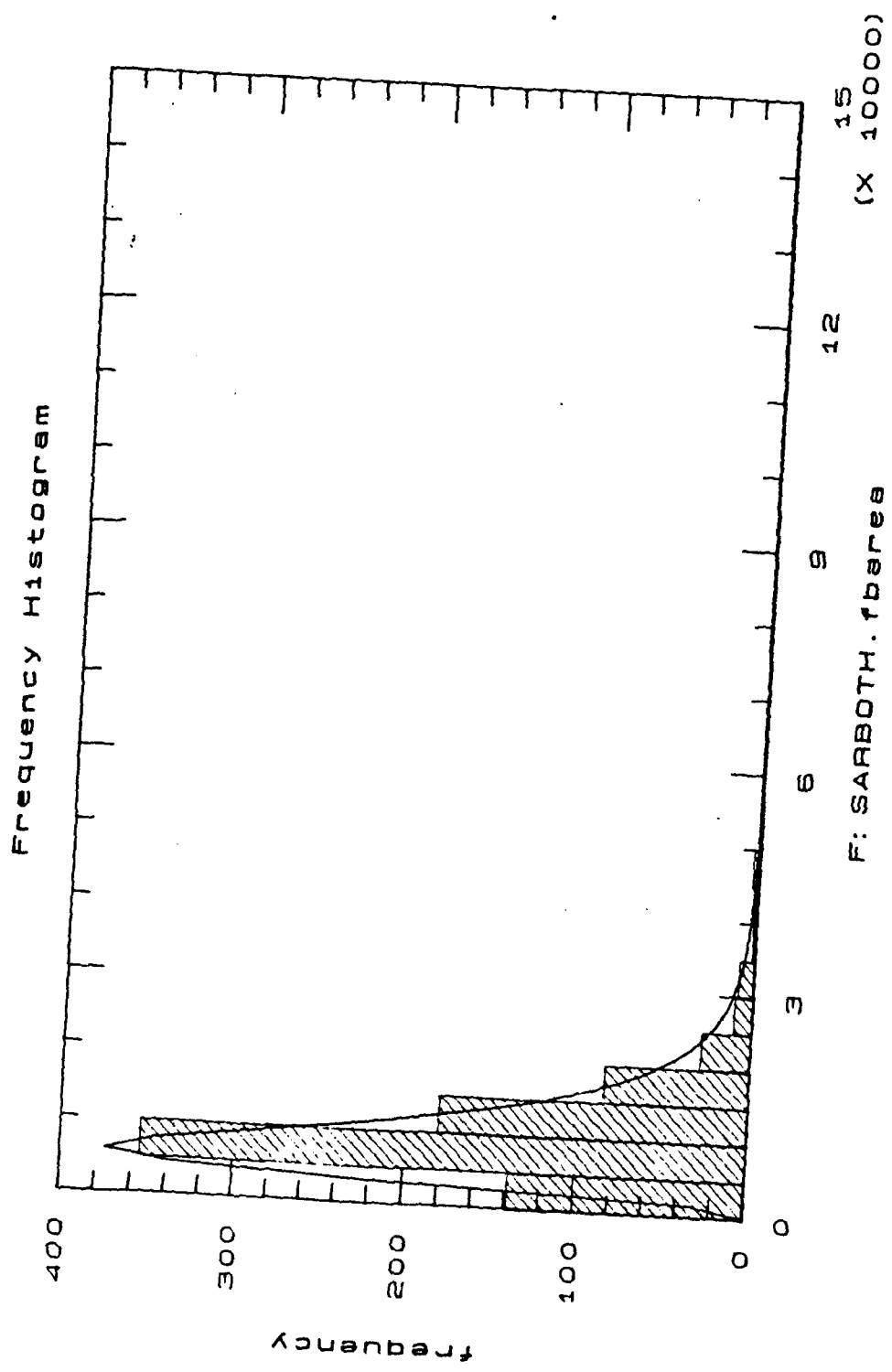


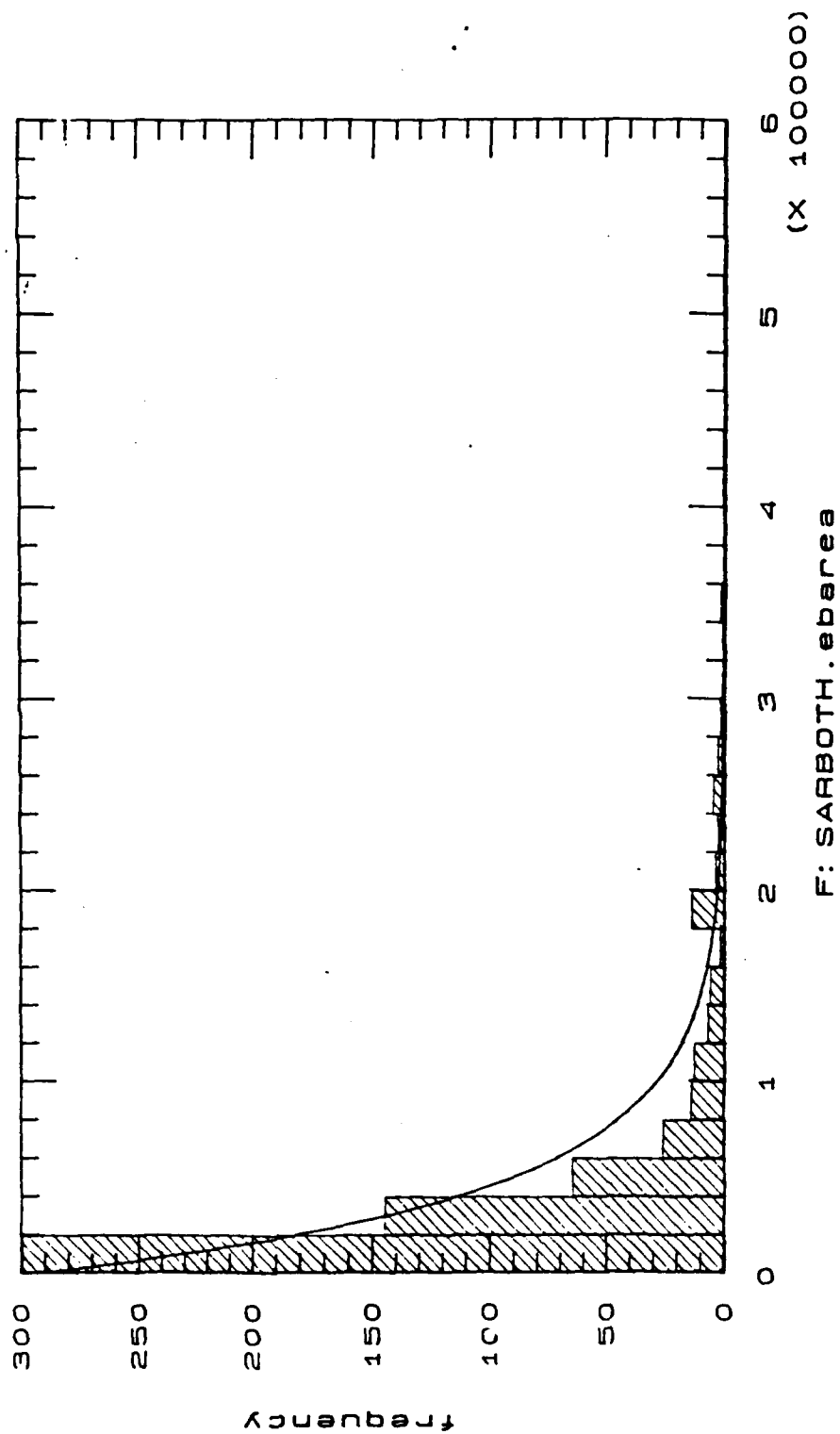
Figure 2



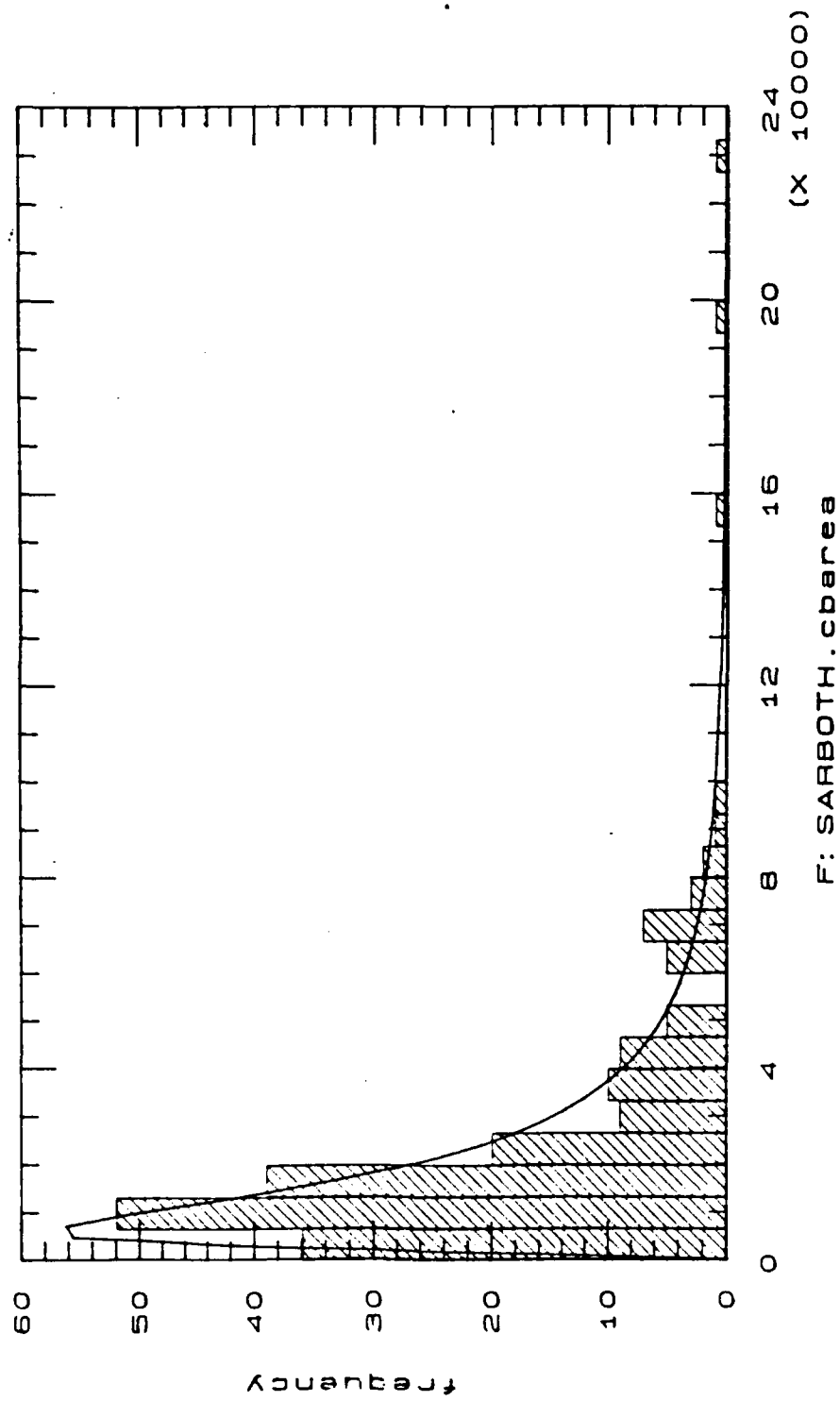
2.

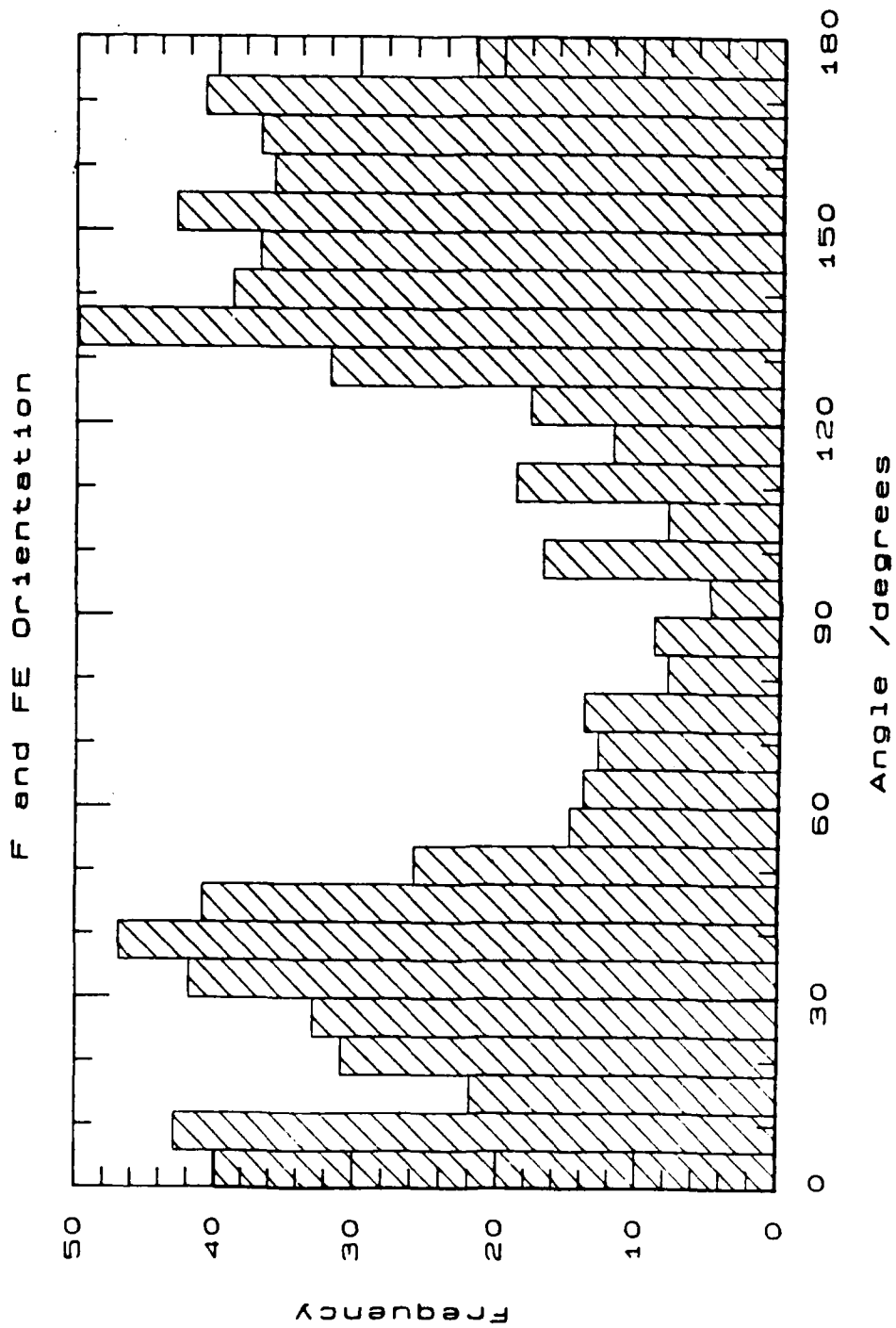


Frequency Histogram



Frequency Histogram





frequency Histogram

